FOUR-BODY SEMILEPTONIC DECAYS OF *D* MESONS

BY

RAYMOND LLOYD CULBERTSON

B.S., Towson State University, 1987
M.S., University of Illinois, 1988

THESIS

Submitted in partial fulfillment of the requirements
for the degree of Doctor of Philosophy in Physics
in the Graduate College of the
University of Illinois at Urbana-Champaign, 1993

Urbana, Illinois

FOUR-BODY SEMILEPTONIC DECAYS OF D MESONS

BY

RAYMOND LLOYD CULBERTSON

B.S., Towson State University, 1987
M.S., University of Illinois, 1988

THESIS

Submitted in partial fulfillment of the requirements
for the degree of Doctor of Philosophy in Physics
in the Graduate College of the
University of Illinois at Urbana-Champaign, 1993

Urbana, Illinois

UNIVERSITY OF ILLINOIS AT URBANA-CHAMPAIGN

THE GRADUATE COLLEGE

MAY 1993

WE HEREBY RECOMMEND THAT THE THESIS BY

RAYMOND LLOYD CULBERTSON

ENTITLED FOUR-BODY SEMILEPTONIC DECAYS OF D MESONS

BE ACCEPTED IN PARTIAL FULFILLMENT OF THE REQUIREMENTS FOR

THE DEGREE OF DOCTOR OF PHILOSOPHY

[redacted]

Director of Thesis Research

[redacted]

Head of Department

Committee on Final Examination†

[redacted]

Chairperson

† Required for doctor's degree but not for master's.

O-517

FOUR-BODY SEMILEPTONIC DECAYS OF D MESONS

Raymond Lloyd Culbertson, Ph.D.
Department of Physics
University of Illinois at Urbana-Champaign, 1993
James E. Wiss, Advisor

Results on measurements of the four-body semileptonic decays $D^+ \to \overline{K}^{*0}\mu^+\nu$, $D^0 \to K^{*-}\mu^+\nu$, and $D_s^+ \to \phi\mu^+\nu$ are presented. New limits on related decays are presented: $\Gamma(D^+ \to K^-\pi^+\mu^+\nu(\text{nonresonant}))/\Gamma(D^+ \to (K^-\pi^+)\mu^+\nu) = .083 \pm .029$, and $\Gamma(D^+ \to (K^-\pi^+)\pi^0\mu^+\nu)/\Gamma(D^+ \to (K^-\pi^+)\mu^+\nu) < .042$. The relative branching ratio is presented: $\Gamma(D^+ \to \overline{K}^{*0}\mu^+\nu)/\Gamma(D^+ \to K^-\pi^+\pi^+) = .56 \pm .04 \pm .06$. The form factors in the decay $D^+ \to \overline{K}^{*0}\mu^+\nu$ are measured to be $R_v = 1.74 \pm .27 \pm .28$, and $R_2 = .78 \pm .18 \pm .10$ which imply $\Gamma_l/\Gamma_t = 1.20 \pm .13 \pm .13$. The ratios of the D^0 and D^+ widths is measured: $\Gamma(D^0 \to K^{*-}\mu^+\nu)/\Gamma(D^+ \to \overline{K}^{*0}\mu^+\nu) = 1.37 \pm .34 \,^{+.15}_{-.35}$. The D_s^+ semileptonic width is measured: $\Gamma(D_s^+ \to \phi\mu^+\nu)/\Gamma(D_s^+ \to \phi\pi^+) = .58 \pm .11 \pm .08$ which implies an absolute branching ratio: $\Gamma(D_s^+ \to \phi\pi^+)/\Gamma(D_s^+ \to \text{all }) = (3.1 \pm .6(\text{stat}) \pm .5 \text{ (sys)} \pm .4 \text{ (theoretical)})\%$.

Acknowledgments

The E687 collaboration is a large group of physicists and technicians from around the world; everyone contributes their part to make the experiment work. Many individuals deserve to be singled out. The E687 spokesman, Joel Butler, deserves credit for organizing the collaboration and taking on many thankless but necessary tasks. Jeff Wilson's contributions to tracking, tracing and packing are the foundation of every analysis. Karen Lingel provided the complete Monte Carlo package. I want to thank these people and Paul Sheldon, Rob Gardner and Glen Jaross for many helpful ideas.

Special thanks go to my advisor, Jim Wiss. His expertise concerning E687 and high-energy physics in general makes him an excellent teacher. His enthusiasm and hard work inspired these results and many more.

Jerry Wray and Dave Lesny are responsible for creating and maintaining a computing environment which few other institutions can equal. I especially appreciate Dave's Vax networking software which provided a huge increase in our effective computing power.

Finally, I want to thank my parents and family for their love and support through the years. I want to thank Paul, Bill, Randy, Jim, Eva, Rose, and especially Renée for distracting me from my work.

This research is funded in part by the U.S. Department of Energy under Grant #DE-FGO2-91ER40677.

Table of Contents

List of Abbreviations

ADC Analog to Digital Converter.

BGM Beam Gamma Monitor – an electromagnetic shower detector designed to collect uninteracted beam photons.

CL Confidence Level – the percentile rank of a χ^2

CL1 The confidence level that a charm daughter does not point back to the primary vertex.

CL2 The confidence level that no tracks, not in the primary or secondary are in the secondary vertex.

DCL The confidence level of a secondary or charm vertex.

ℓ/σ The separation between the primary vertex and a charm secondary vertex divided by its error.

5 – chamber A particle trajectory that is measured in all PWC planes and passes through M2.

Golden modes The copious all charged D decays $K\pi$, $K2\pi$, and $K3\pi$.

H × V The horizontal and vertical scintillator trigger array.

Link The requirement that a particle trajectory is found in the SSD's and the PWC's and the two segments are associated.

M1, M2 The first and second analysis magnets.

MCS Multiple Coulomb Scattering

MWPC – Multiwire Proportional Chambers, also PWC or chambers.

OE, IE Outer electromagnetic detector and inner electromagnetic detector.

OM, IM Outer muon detector and inner muon detector.

Primary vertex The photon-nucleon interaction point.

RESH Recoil Electron Shower Hodoscope.

SSD Silicon Microstrip Detector

Stub A particle trajectory that is measured in the first 3 PWC planes only, P0-P2.

Track parameters A set of numbers used to define a particle trajectory either $(x, x' = p_x/p_z, y, y' = p_y/p_z)$ or (x, x', y, y', p).

Chapter 1

Introduction

This thesis reports on analysis of the data collected by E687 during the years 1987 through 1991 at the Wideband Photon Lab at the Fermi National Accelerator Laboratory. E687 uses a photon beam with a mean energy of approximately 200GeV and a Beryllium target to produce charm mesons and baryons. The products of the interactions are are detected by a large aperture magnetic spectrometer. We have collected approximately 80,000 fully reconstructed charm decays.

There are three ways that charmed particles have been produced in large numbers. The first is in e^+e^- rings where the center of mass energy is near the threshold for producing two charm particles. The other two are fixed target methods with either hadron beams or photon beams. The advantage of production through e^+e^- collisions is that there are few background mechanisms but the overall rate is low. The advantage of hadroproduction is a large production rate but the hadron-hadron collisions tend to produce large numbers of particles in every event. This, together with significant cross sections for non-charm production, leads to large backgrounds. Photoproduction has the advantage of a large production rate but the photon-hadron interactions tend to have fewer particles in each event, giving better signal to noise than hadroproduction.

E687 data are consistent [1] with the photon-gluon fusion [2] production mechanism shown in Figure 1.1. In this mechanism, the photon interacts with a gluon from a target nucleon that has fluctuated into a charm, anti-charm quark pair. The quarks are forced out of the nucleon and are dressed to produce the charm mesons or baryons. Charm particles live approximately 1ps then decay weakly to (predominately) strange and other particles. We then detect these decay products. The finite lifetime of charm particles is the principle property that we exploit to isolate signals from copious non-charm backgrounds.

In this thesis we give an overview of the E687 spectrometer and the data reconstruction and processing methods. We present a method for calculating the true errors on track parameters that were estimated from least squares fits that ignore mutiple Coulomb scattering and tests of these calculations. We present a candidate driven vertexing algorithm and demonstrate its effectiveness.

We investigate the muonic four-body semileptonic decays of the ground state charm mesons: $D^+ \to \overline{K}^{*0}\mu^+\nu$, $D^0 \to K^{*-}\mu^+\nu$, and $D_s^+ \to \phi\mu^+\nu$. The $\overline{K}^{*0}$ is detected in its $K^-\pi^+$ decay mode, the K^{*-} is detected in its $K_s\pi^-$ decay mode, and the ϕ is detected in its K^+K^- decay mode. Because we do not detect the neutrino in these decays, they are not fully reconstructed and therefore are susceptible to insidious backgrounds. We will present extensive studies of potential backgrounds.

In the D^+ analysis we will measure the branching ratio of this decay mode relative to $K^-\pi^+\pi^+$ and the form factors governing the decay. These measurements can be compared to theoretical predictions to provide information on the internal structure of the charm mesons. In the D^0 analysis we will measure the branching ratio between the D^0 and D^+ semileptonic decays. This is a test of isospin symmetry. In the D_s^+ analysis we will report a measurement of the branching ratio relative to $\phi\pi^+$. This branching ratio has implications for all D_s^+ absolute branching ratios because, with a theoretical input, it can be used to determine the absolute branching ratio for $D_s^+ \to \phi\pi^+$.

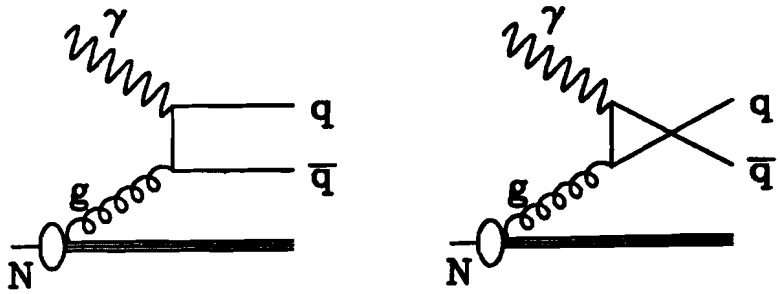

Figure 1.1. The photon-gluon fusion mechanism for the photoproduction of charm.

Chapter 2

The Phenomenology of Four-body Semileptonic Decays

2.1 Overview

In this chapter we review some of the phenomenology relevant to the three semileptonic decays discussed in this thesis: $D^+ \to \overline{K}^{*0}\mu^+\nu$, $D^0 \to K^{*-}\mu^+\nu$ and $D_s^+ \to \phi\mu^+\nu$. Invariance arguments can be used limit the description of the decay intensity which governs the decay angular distribution and rate to a set of four form factors. Isospin symmetry can be used to equate the form factors for $D^0 \to K^{*-}\mu^+\nu$ to those for $D^+ \to \overline{K}^{*0}\mu^+\nu$ decay. This relationship is tested in Chapter 8. Dynamical calculations predict these form factors, and relate the form factors for $D_s^+ \to \phi\mu^+\nu$ to those for $D^+ \to \overline{K}^{*0}\mu^+\nu$. Chapter 7 compares our measurements of the $D^+ \to \overline{K}^{*0}\mu^+\nu$ form factors to several phenomenological predictions. Chapter 9 uses the expected relationship between D_s^+ and D^+ semileptonic form factors to help discriminate against possible $\phi\mu^+\nu$ backgrounds and to infer new measurements of the $D_s^+ \to \phi\pi^+$ absolute branching ratios.

Since the semileptonic decays of charmed mesons should proceed via a simple spectator diagram (see Figure 2.1) they should be among the most theoretically understandable charm particle decays. Because the decay amplitude can be factorized into a hadronic and a well understood leptonic part, the validity of theories on the hadronic part can be studied experimentally. As a result, the investigation of these three decay modes and related semileptonic decays in both the beauty and charm sector has become a major focus of theoretical and experimental heavy quark physics at both fixed target facilities [3,4,5] and at e^+e^- collider facilities [6].

This thesis concentrates on specific semileptonic decays of the form $D \to V\mu\nu$ where the D (either the D^0 , D^+ or D_s^+) is a ground state 0^- meson and the V is a 1^- vector meson (either the $\overline{K}^{*0}$, K^{*-} or ϕ) which decays into two pseudoscalars. The amplitude for semileptonic factorization into hadronic and leptonic parts can

be written as follows: $\mathcal{A} = \frac{G_F}{\sqrt{2}} V_{cs} L^\mu H_\mu$ where G_F and V_{cs} are the Fermi constant and CKM coupling, L^μ is the pointlike leptonic current given by:

$$L^\mu = \overline{u}(\nu)\gamma^\mu(1-\gamma_5)v(\mu) \tag{2.1}$$

and H_μ is a hadronic current of the form: $H_\mu(q^2) = < V(\vec{\epsilon})|J_\mu^{(\mathrm{had})}|D >$.

This hadronic current depends on the polarization state of the vector meson, V, as well as the the momentum transfer ($t = q^2$) between the D and V meson. Because the initial and final state are composite rather than pointlike particles, their hadronic current depends on a set of q^2 dependent form factors which describe the coupling of their wave functions to the virtual W^+. Because this current describes the coupling of cs system to virtual W^+, one traditionally [7,8] assumes that these form factors have a simple pole dependence $(M^2+q^2)^{-1}$ where the pole mass M is assumed to be the mass of the lowest D_s^{*+} states which have the same spin and parity as the current described by each form factor.

One builds the hadronic current using all possible Lorentz invariant forms that can be constructed from the D and V four momenta and the V polarization ($\vec{\epsilon}$). One can show [9,10] that four independent q^2 dependent form factors are required. One of these form factors only produces amplitude terms which are proportional to m_μ^2/q^2 which are totally negligible for the case of electronic semileptonic decay and produce only slight corrections for the case of muonic semileptonic decay.

The $\vec{\epsilon}$ (vector meson spin) dependence in the hadronic current produces a non-isotropic vector meson decay angular distribution. The $V-A$ lepton helicity rule which describes the coupling of the $\mu^+\nu$ system to the virtual W^+ vertex produces a non-isotropic $\mu^+\nu$ angular distribution. By fitting the q^2 dependence of the vector meson decay and the angular distributions, one can in principle measure each of the four form factors and compare them to theoretical calculations. Such calculations are ultimately based on models of the wave functions which describe how the mesons couple to their quark constituents. This comparison is made in

Chapter 7 for the three major form factors whose effects survive in the $m_\ell \to 0$ limit.

Before summarizing the formal phenomenology of the semileptonic decay distributions, we give a simplified, heuristic picture of the angular decay distribution which is schematically illustrated in Figure 2.2. For definitiveness, consider the case of the D^+ decaying to $\overline{K}^{*0}\mu^+\nu$ in the $m_\ell \to 0$ limit. In this simple picture, the virtual W^+ which connects both the $\mu^+\nu$ and $\overline{K}^{*0} \to K^-\pi^+$ decays can exist in any of the three possible helicity states $m = -1$, 0 , or $+1$ with a probability proportional to a width Γ_m. The helicity states $m = \pm 1$ correspond to transverse W^+'s where the W spin lies along or against its momentum vector (like the spin of a photon); the helicity state $m = 0$ corresponds to the longitudinal W^+.

Angular momentum conservation applied to the $D^+ \to K^-\pi^+W^+$ vertex tells us that this decay amplitude is proportional to the Wigner D-matrix $d^1_{0m}\ (cos\ \theta_v)$ where θ_v is the angle of the pion with respect to the virtual D direction in the $\overline{K}^{*0}$ rest frame. The fact that the kaon and pion are spinless implies that W^+ has zero angular momentum along the $\overline{K}^{*0}$ decay axis while simultaneously having an angular momentum of m along its momentum axis. The fact that the ν must be left-handed while the μ^+ is overwhelmingly right-handed implies that the $W^+ \to \mu^+\nu$ decay amplitude is proportional to $d^1_{1m}\ (cos\ \theta_\mu)$ where θ_μ is the angle of the neutrino with respect to the D direction in the W rest frame. We then expect:

$$\frac{d^2\Gamma}{d\cos\theta_v\ d\cos\theta_\mu} \propto \sum_{m=-1}^{m=1} \Gamma_m \mid d^1_{1m}\ (cos\ \theta_\mu) \mid^2 \mid d^1_{0m}\ (cos\ \theta_v) \mid^2$$

$$\propto \sin^2\theta_v\ \{(1+\cos\theta_\mu)^2\ \Gamma_+ + (1-\cos\theta_\mu)^2\ \Gamma_-\} + 4\cos^2\theta_v \sin^2\theta_\mu\ \Gamma_0 \qquad (2.2)$$

where we have averaged over the azimuthal angle between the $\mu^+\nu$ and $K^-\pi^+$ decay planes and ignored any possible q^2 dependance on the Γ_m's. If all three Γ_m's were equal (not the case in reality!) there would be no net alignment effects

and isotropic decay distributions would result. The degree of $cos\theta_v$ anisotropy is directly related to the ratio of the longitudinal $\Gamma_\ell = \Gamma_0$ and transverse ($\Gamma_t = \Gamma_+ + \Gamma_-$) widths:

$$\frac{d\Gamma}{d\cos\ \theta_v} \propto 1 - \left(2\ \frac{\Gamma_\ell}{\Gamma_t} - 1\right)\ cos^2\ \theta_v \tag{2.3}$$

The next section describes how the longitudinal and transverse W^+ widths and their q^2 dependence depend on the relevant form factors.

2.2 The Semileptonic Decay Intensity

In this section we present the formal decay intensity for the the decay $D \to V\mu\nu$. Although this intensity applies to any decay of the form $D \to V\mu\nu$, we will present it in terms of the the specific decay $D^+ \to \overline{K}^{*0}\mu^+\nu$. The decay width has the form [7,9,10]:

$$\begin{aligned}\frac{d^4\Gamma}{dM^2_{K\pi}\ dt\ dcos\theta_v\ dcos\theta_\mu} =& G_F^2|V_{cs}|^2\frac{3}{2(4\pi)^5}\frac{M_{K^*}}{M_D^2 M_{K\pi}} \\ & \frac{M_{K^*}\Gamma}{(M^2_{K\pi} - M^2_{K^*})^2 + M^2_{K^*}\Gamma^2} Kt\left(1 - \frac{m_\mu^2}{t}\right)^2 \\ & \left[\text{diagonal terms} + \text{cross terms} + \frac{m_\mu^2}{t}(\text{mass terms})\right]\end{aligned} \tag{2.4}$$

$$\begin{aligned}\text{diagonal terms} =& \sin^2\theta_v\ \{(1+\cos\theta_\mu)^2\ |H_+(t)|^2\ +\ (1-\cos\theta_\mu)^2\ |H_-(t)|^2\} \\ & + 4\cos^2\theta_v \sin^2\theta_\mu\ |H_0(t)|^2\end{aligned} \tag{2.5}$$

$$\begin{aligned}\text{cross terms} =& -2\sin^2\theta_v \sin^2\theta_\mu \cos 2\chi\ \mathcal{R}e(H_+^* H_-) \\ & - 4\sin\theta_v\cos\theta_v\sin\theta_\mu(1+\cos\theta_\mu)\cos\chi\ \mathcal{R}e(H_+^* H_0) \\ & + 4\sin\theta_v\cos\theta_v\sin\theta_\mu(1-\cos\theta_\mu)\cos\chi\ \mathcal{R}e(H_-^* H_0)\end{aligned} \tag{2.6}$$

$$
\begin{aligned}
\text{mass terms} = & 2\sin^2\theta_v \sin^2\theta_\mu(|H_+|^2 + |H_-|^2) \\
& +8\cos^2\theta_v(1+\cos^2\theta_\mu)|H_0|^2 \\
& +4\sin^2\theta_v \sin^2\theta_\mu \cos 2\chi \ \mathcal{R}e(H_+H_-^*) \\
& +2\sin 2\theta_v \sin 2\theta_\mu \cos\chi \ \mathcal{R}e(H_+H_0^* + H_-H_0^*) \\
& +16\cos^2\theta_v \cos\theta_\mu \ \mathcal{R}e(H_tH_0^*) \\
& +4\sin 2\theta_v \sin\theta_\mu \cos\chi \ \mathcal{R}e(H_+H_t^* + H_-H_t^*)
\end{aligned}
\tag{2.7}
$$

G_F is the Fermi coupling constant, V_{cs} is the relevant CKM matrix element, M_{K^*} is the K^* mass, $M_{K\pi}$ is the $K\pi$ invariant mass, m_μ is the muon mass, and K is the $K\pi$ momentum in the D rest frame. The kinematic variables (in addition to $M_{K\pi}$) are $\cos\theta_v$, the angle between the π and the D direction in the $\overline{K}^{*0}$ rest frame, $\cos\theta_\mu$, the angle between the ν and the D direction in the $\mu\nu$ rest frame, t, the square of the $\mu\nu$ mass, and χ the angle between the $K\pi$ and $\mu\nu$ planes in the D rest frame.

D^- decays have the same definition of variables and no change is required in the matrix element. There is a vast amount of confusion in the literature [7,9,10] concerning this point although it is a reasonably straightforward consequence of the approximate CP symmetry of the weak interaction. Under CP the D^+ is transformed into the D^- and the muon and neutrino helicities reverse, causing factors such as $1 + cos\ \theta_\mu$ to transform into $1 - cos\ \theta_\mu$. Simultaneously the W^+ with helicity ± 1 transforms into a W^- with helicity ∓ 1 causing the H^+ form factor to transform into the H^- form factor. The effect of both transformations is to leave the decay intensity (as expressed by equations 2.4-7) unchanged in going from the particle to antiparticle case.

Note that if we integrate over χ, the cross terms and half of the mass terms produce no contribution to the width. If the muon mass is replaced by the electron mass, which is negligible, the mass terms, which are already small for muons, become negligible for electrons.

We note that the phase space in this expression is written for the three-body decay $\overline{K}^{*0}\mu^+\nu$, and the Breit-Wigner has been included as a *post-hoc* correction. The three-body phase space contributes the factor of K and one factor of $(1 - m_\mu^2/t)$ while the matrix element itself contributes the factor of t and another factor of $(1 - m_\mu^2/t)$.

Because the K^* is spin 1, the Breit Wigner is a parameterized as with a p-wave form where the width is given by:

$$\Gamma = \Gamma_0 \frac{P^{*3}}{P_0^{*3}} \tag{2.8}$$

where P^* is the momentum of the K in the $K\pi$ rest frame, the 0 subscript refers to the value at $M_{K\pi} = M_{K^*}$.

The H_i appearing in the matrix element expression are the projections of the form factors on the W helicity basis.

$$\begin{aligned}
H_\pm(t) &= (M_D + M_{K\pi})A_1(t) \mp 2\frac{M_D K}{M_D + M_{K\pi}} V(t) \\
H_0(t) &= \frac{1}{2M_{K\pi}\sqrt{t}}\left[(M_D^2 - M_{K\pi}^2 - t)(M_D + M_{K\pi})A_1(t) - 4\frac{M_D^2 K^2}{M_D + M_{K\pi}} A_2(t)\right] \\
H_t(t) &= \frac{M_D K}{M_{K\pi}\sqrt{t}}\left[(M_D + M_{K\pi})A_1(t) - \frac{(M_D^2 - M_{K\pi}^2 + t)}{M_D + M_{K\pi}} A_2(t) + \frac{2t}{M_D + M_{K\pi}} A_3(t)\right]
\end{aligned} \tag{2.9}$$

There are three axial form factors, A_i, and one vector form factor, V with an unknown t dependence. The usual assumption [7,8] is that these form factors have a single pole form:

$$A_i(t) = \frac{A_i(0)}{1 - t/M_A^2}, \qquad V(t) = \frac{V(0)}{1 - t/M_V^2} \tag{2.10}$$

Where $M_A = 2.5\text{GeV/c}^2$ and $M_V = 2.1\text{GeV}/^2$ which are the masses of the lowest lying $c\bar{s}$ meson states with the correct quantum numbers.

In Chapter 7 we will fit for the ratios of the form factors at $t = 0$:

$$R_v = \frac{V(0)}{A_1(0)}, \qquad R_2 = \frac{A_2(0)}{A_1(0)}, \qquad R_3 = \frac{A_3(0)}{A_1(0)} \tag{2.11}$$

which are determined by the ***shape*** of the distributions of the kinematic variables. Given these form factor ratios, V_{cs}, and the partial width $\Gamma(D^+ \to \overline{K}^{*0}\mu^+\nu)$, we can calculate the value of $A_1(0)$ which is determined by the ***overall decay rate.***

For this we integrate the matrix element expression over the angles and find:

$$\Gamma = \frac{G_F^2|V_{cs}|^2}{96\pi^4} \int dM_{K\pi}^2 \int dt\ G(t, M_{K\pi})(|H_+|^2 + |H_-|^2 + |H_0|^2) \tag{2.12}$$

where

$$G(t, M_{K\pi}) = \frac{M_{K^*}}{M_D^2 M_{K\pi}} \frac{M_{K^*}\Gamma}{(M_{K\pi}^2 - M_{K^*}^2)^2 + M_{K^*}^2\Gamma^2} Kt \left(1 - \frac{m_\mu^2}{t}\right)^2 \tag{2.13}$$

We can then do the integrals after factoring out $A_1(0)$ and inserting our measurements of the form factor ratios. This leaves an expression for the width in terms of $A_1(0)$ which can then be solved for $A_1(0)$, as we do in Chapter 7.

$$\frac{\Gamma(D^+ \to \overline{K}^{*0}\mu^+\nu)}{\Gamma(D^+ \to K^-\pi^+\pi^+)} \frac{\Gamma(D^+ \to K^-\pi^+\pi^+)}{\Gamma(D^+ \to \text{all})} \frac{\hbar}{\tau_{D^+}} = \Gamma(D^+ \to \overline{K}^{*0}\mu\nu) =$$
$$\frac{G_F^2|V_{cs}|^2 A_1^2(0)}{96\pi^4} \int dM_{K\pi}^2 \int dt\ G(t, M_{K\pi})(|H_+|^2 + |H_-|^2 + |H_0|^2)/A_1^2(0) \tag{2.14}$$

When we make this calculation in Chapter 7, we will use our new measurement [11] of the $D^+ \to \overline{K}^{*0}\mu^+\nu$ to $D^+ \to K^-\pi^+\pi^+$ branching ratio.

The ratio of longitudinal to transverse width (polarization) of the W is defined as:

$$\frac{\Gamma_l}{\Gamma_t} = \frac{\int dM_{K\pi}^2 \int dt\ G(t, M_{K\pi})|H_0|^2}{\int dM_{K\pi}^2 \int dt\ G(t, M_{K\pi})(|H_+|^2 + |H_-|^2)} \tag{2.15}$$

This then determines the curvature of the $\cos\theta_v$ distribution in equation 2.3.

The polarization depends slightly on the lepton mass. Because other experiments analyze the equivalent decay mode $D^+ \to \overline{K}^{*0} e^+ \nu$, we report this result in the limit that the lepton mass is negligible.

2.3 Relating the Semileptonic Decays of the D^+, D^0 and D_s^+

Isospin symmetry applied to the D semileptonic decay predicts that the $D^+ \to \overline{K}^{*0} \mu^+ \nu$ and $D^0 \to K^{*-} \mu^+ \nu$ should have identical form factors. Although, in general, strong isospin is not a valid symmetry for weak decays, in Cabibbo favored semileptonic decays (such as those studied here), the weak current transforms like an isosinglet since it connects the isosinglet c to the isosinglet s quark. Given that this is true one can transform the current $< \overline{K}^{*0} | J_\mu^{(\mathrm{had})} | D^+ >$ into the current for $< K^{*-} | J_\mu^{(\mathrm{had})} | D^0 >$ (apart from possible phase factors) by simply rotating by 180° about I_2. This will transform the D^+ into its isodoublet partner, the D^0 and the $\overline{K}^{*0}$ into its isodoublet partner, the K^{*-}. Because the phase space for $D^+ \to \overline{K}^{*0} \mu^+ \nu$ and $D^0 \to K^{*-} \mu^+ \nu$ are nearly identical (since the D^+ and D^0 differ in mass by only ≈ 3 MeV/c^2), equality of the form factors implies equality of the partial widths $\Gamma(D^0 \to K^{*-} \mu^+ \nu) = \Gamma(D^+ \to \overline{K}^{*0} \mu^+ \nu)$. This prediction is directly tested in Chapter 8.

There are no simple symmetry arguments which we are aware of which can be used to directly relate the decay $D^+ \to \overline{K}^{*0} \mu^+ \nu$ to the decay $D_s^+ \to \phi \mu^+ \nu$. All dynamical calculations, which are based on various models of the meson wave functions, conclude that the form factor ratios should be nearly identical [12] and partial widths should be equal to within 20% [13]. We make use of these results in Chapter 9.

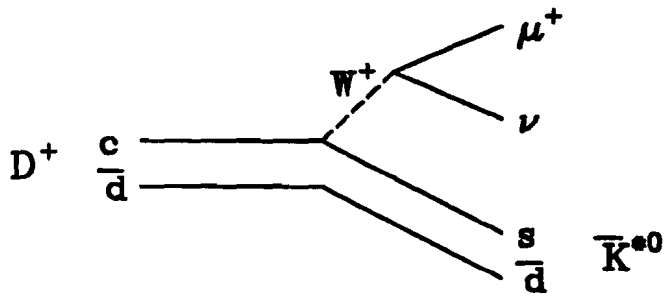

Figure 2.1. The spectator diagram for the four-body semileptonic decay of the D^+.

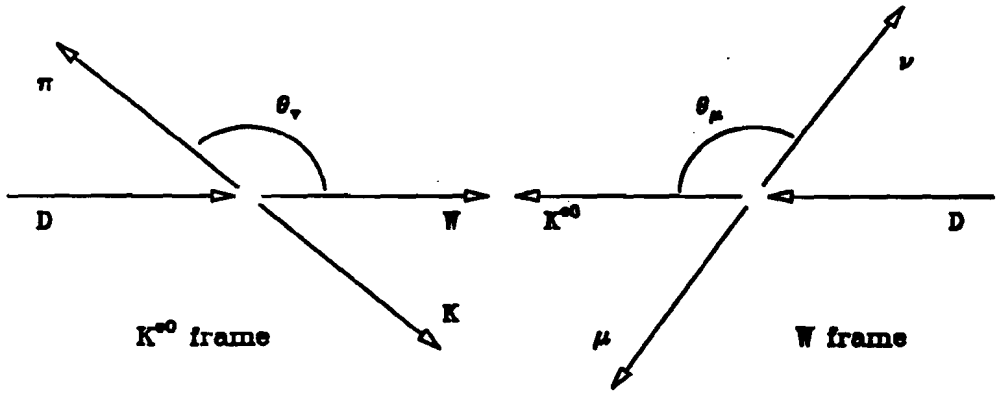

Figure 2.2. Schematic for the definitions of the cosines in the four-body semileptonic decay of the D^+. $\cos\theta_v$ is the angle between the π and the D direction in the $\overline{K}^{*0}$ rest frame and $\cos\theta_\mu$ is the angle between the ν and the D direction in the $\mu\nu$ rest frame.

Chapter 3

Experimental Apparatus and Run History

The E687 apparatus has been described in detail [3,14] and we include a brief description here.

3.1 Beamline

To provide beams for fixed target experiments, the Fermilab Tevatron operates in cycles of about one minute. The Tevatron is filled with a protons which are accelerated to 800GeV and then extracted over a 20s "spill". About $3-4\times10^{12}$ protons are delivered to the E687 beamline during each spill. The beam is directed to a liquid deuterium target where it interacts producing a hadron shower.

A large number of π^0's are produced in the shower which immediately decay to two photons. At this point magnets sweep the charged particles out of the beam leaving only the photons, neutrons and neutral K's. The beam strikes a 50% radiation length lead foil (the convertor) which causes about half of the photons to convert into e^+e^- pairs. The electrons are bent out of the beam and the neutral hadrons and positrons continue into a dump where they are absorbed.

More dipoles combined with collimators select the electrons with a mean energy approximately 350GeV. The energy range is intentionally large, 15% (wideband), to provide a large luminosity. Finally, the electrons are directed to a 27% radiation length lead foil (the radiator) which causes them to bremsstrahlung, producing a photon beam. The recoiling electrons are swept away and the photon beam strikes the experimental Be target.

3.2 Beam Tagging

For some measurements, we must know the energy of the photon. There are three parts to this measurement. The first part is to measure the energy of the incoming electron before it reaches the radiator. This job is accomplished by a set of five planes of silicon microstrips, known as the "beam tagging" detector, in

the electron beam. The planes are arranged so that there are two planes, followed by a dipole magnet, followed by another plane, another dipole and the last two planes. The planes are orientated so that they can measure the electron's bend in the magnets, which provides its energy (E_{inc}).

After the electron radiates photons in the radiator, it passes through another dipole to measure its energy again. The difference in the incoming and outgoing electron energy is how much energy was released in photons as the electron passed through the radiator. Just downstream of the radiator is set of dipoles which sweep the recoil electron into a set of scintillators called the RESH. The struck counter number determines the electron's magnetic deflection which measures the recoiling electron energy (E').

To this point, we have measured the amount of energy that the electron has lost. However, that energy will be divided up between the photon that interacts in the target and other non-interacting photons. The latter are collected in an electromagnetic calorimeter called the BGM which is centered on the beam, near the end of the detector. This energy sum is called E_{BGM}. (In the 1991 run the BGM was removed to accommodate a downstream experiment. This experiment provided a signal from their calorimeter to replace the BGM measurement.)

The energy of the interacting photon is estimated from:

$$E_\gamma = E_{inc} - E' - E_{BGM}. \tag{3.1}$$

3.3 Microstrips

The experimental target is a slab of Beryllium 2.54cm square and approximately 4cm long (12% of an interaction length).

About 5cm downstream of the target sits the microstrip system which measures charged particle trajectories with very high precision. This device is used to exploit the lifetime of charm (typically 1cm decay flight distance for mesons)

to identify charm signals. A layout of the microstrip system is shown in Figure 3.1. The twelve microstrip planes are arranged into four stations of three planes each. In each station, one plane measures in the y direction and the other two are tilted in opposite directions from the y plane by 45°. The first station is about 6cm downstream of the target and last is about 30cm downstream. Each plane is divided into an inner, high-resolution region and an outer, lower-resolution region. The strips of the planes in the first station have pitches of 25μm (inner region) and 50μm (outer) and all other stations have pitches of 50μm (inner) and 100μm (outer).

The charge collected from each strip is amplified and read by an ADC. Charge division between adjacent strips is used to improve the resolution.

Two experimental targets were used during the 1990-91 run. These were made from layers of Be, 2.54cm square and 4mm thick. For about the first 1/2 of the 90 run, 9 layers were used, then 11 layers were used for the rest of the run. The squares are tilted at 45° to align them with the high-resolution region of the microstrip planes.

3.4 MWPC's and Magnets

A layout of the MWPC system along with the rest of the spectrometer is shown in Figure 3.2 and summarized in Table 3.1. After charged particles pass through the microstrips, they are bent vertically (in y) in a dipole magnet, M1, with a kick ($= .3 \int B\ dl$) of .4GeV/c. After the magnet are three multiwire proportional chambers (P0-P2). P0 has 2mm wire spacings, P1 and P2 have 3mm wire spacings.

Each of the chambers has four views, one measures in x, one in y and two others (u and v) are tilted in opposite directions from the y view by 11°. Each view is a set of readout wires separated from the other views by a cathode plane, also made of wires. Charged particles passing through these chambers ionize Ar-Ethane gas while a high voltage between the readout and cathode planes

amplifies and collects the ions. The signals are further amplified and are recorded by TDC's.

Downstream of these chambers, there is another vertically bending magnet, M2, with a kick of -.836GeV/c. The kicks of the two magnets are opposite to improve acceptance. Finally, following M2 are two more MWPC stations of the same design (P3 and P4). P3 has 2mm wire spacings and P4 has 3.3mm wire spacings.

3.5 Particle Identification

3.5.1 Cherenkov

E687 has three threshold Cherenkov counters to help identify particle types. C1, with a π threshold of 8.4GeV is located between the first and second MWPC stations. This counter is segmented into an inner region with two 45° plane mirrors directing the Cherenkov light to phototubes mounted on the side. The outer region is made of focusing mirrors which direct the light backwards to phototubes mounted near the upstream end of the counter. C2, with a π threshold of 4.5GeV is located between the second and third MWPC stations. This counter has two large 45° plane mirrors directing light to the phototubes mounted on the side. C3, with a π threshold of 17.4GeV is located between the third and fourth MWPC stations. This counter has only focusing mirrors. C1 contains a helium-nitrogen mixture, C2 contains nitrous oxide and C3 contains pure helium. A layout of the Cherenkov system along with the rest of the spectrometer is shown in Figure 3.2 and summarized in Table 3.1.

3.5.2 Muon Identification

E687 has an outer muon detector which is shielded behind M2. It has two layers of scintillators (OMH, OMV) and separate x and y views of 5.08cm diameter proportional tubes (OMX OMY).

There is also an inner muon detector which is shielded by the inner electromagnetic detector, the hadron calorimeter, cement blocks and steel. After this material there are 2 layers of scintillators (IMH1, IMV1) and x and y 5.08cm diameter proportional tube arrays (IM1X, IM1Y). After this there is more shielding followed by another set of x and y proportional tube arrays (IM2X, IM2Y) and another layer of scintillators (IM2H). A layout of the muon system along with the rest of the spectrometer is shown in Figure 3.2 and summarized in Table 3.1.

During the 1990 run, some periods had no muon identification due to an error in timing of the readout. During the 1991 run a large slice in both x and y was removed from the inner system to accommodate a downstream experiment. This caused additional noise and inefficiencies for muon identification.

3.5.3 Calorimeters

E687 has inner and outer electromagnetic detectors. The outer detector (OE) lies just upstream of M2 and frames the aperture of M2. It is made from layers of lead and scintillator. The inner detector (IE) is also lead and scintillator but the scintillator is formed into bundles of fibers. This construction allows for a inexpensive, longitudinally thin calorimeter which minimizes the confusion from hadronic showers.

The hadron calorimeter only covers the inner part of the spectrometer and lies immediately behind the inner electromagnetic calorimeter. This is a gas hadrometer which uses steel as the absorber and Ar-Ethane proportional tubes as the ionization medium. The measured resolution $\sigma_E/E \approx 1.33/\sqrt{(E)}$.

3.6 Trigger

In high-energy photoproduction on Be, the rate for hadronic interactions is about 1/500 of the rate for pair production. The purpose of the trigger is to select only these hadronic interactions by accepting only events with wide angle tracks and non-negligible energy deposited in the hadron calorimeter.

The main hadronic trigger is evaluated in two stages. A first level trigger consisting only of scintillators requires the presence of a multiparticle event outside of the region where beam related e^+e^- pairs are produced.

Once a first level trigger ("master gate" or MG) occurs, the evaluation of the second level trigger and readout of the event begins. The second level takes longer to evaluate than the first level and makes more stringent requirements on the event. If the event does not pass the second level trigger, the readout of the event is stopped, the data aquisition is reset and becomes available for the next MG.

3.6.1 First Level Trigger

The first level is derived from several scintillators. First there are the TR counters. TR1 lies between the target and the microstrips and ensures there are charged particles coming from the target. TR2 lies downstream of the microstrips and requires that the particles that fired TR1 also go through the microstrips.

We ran with several combinations of veto requirements. The large TM counters, laying upstream of the target, are intended to veto events with a muon coming from interactions in the primary target. There are also two small counters, A0 and A1, in the photon beam to reject events with hadrons in the beam. The TR counters and the vetoes are combined into a signal called T.

To require wide angle tracks in the event we use a scintillator hodoscope called H$\times$V. This array of a layer of horizontal paddles crossed with a layer of vertical paddles lies immediately downstream of M2, just after the last PWC station. A vertical gap (of about 4cm) allows pairs from beam photons to pass. A logic module computes if the pattern of hits is consistent with at least one particle (H$\times$V$_1$) or more than one (H$\times$V$_2$). Another single layer of scintillator mounted on the upstream end of of the outer electromagnetic calorimeter is called OH. The full requirement of the MG is then

$$\mathrm{T.(H \times V_2 \ + \ H \times V_1.OH)}$$

although some data was restricted to the H × V_2 component.

3.6.2 Second Level Trigger

When the second level trigger is evaluated, the modules reading out the PWC system have produced a pulse proportional to the number of hits in each plane. The outputs from all planes are combined and a minimum requirement is made in a logic module. Most of the data the required evidence for at least three tracks outside of the pair region. Some data was taken with looser multiplicity requirements.

The most important element in the second level trigger is the HC energy requirement which provides additional rejection against e^+e^- pair events. The charge output of the HC is summed to provide an estimate of the hadronic energy and a minimum deposition is required. The requirement corresponded to roughly 35GeV in the 1988 run and 40-50GeV in the 1990 and 1991 runs.

When a MG fires, it holds off further MG's for approximately 100ns while the second level trigger is decided. If the second level trigger is satisfied, further MG's are are again held off until the detector is read out. The combination of these gives a typical deadtime of about 25%.

3.6.3 Muon Runs

A very wide beam of muons from interactions in the primary deuterium target is always passing through the detector. If the normal photon beam is blocked, only the muon beam survives. Under these conditions we can make a trigger out of the TM counter and H×V_1 to get events with a single muon passing through the detector. These runs are used to calibrate the calorimeters, the Cherenkovs and the inner muon system.

3.7 Coordinate Systems

There are two main coordinate systems employed in analysis. Both have the positive z axis oriented along the beam direction, positive x pointing to the

west, and positive y vertically upward. The first system, called the M2 system, has the origin at the bend center of M2. The second system, called granite block coordinates, has its origin at the upstream edge of the granite block that supports the microstrips; the offset between the two is $\approx$ 1240cm. M2 coordinates are used for analysis of MWPC data and lepton identification while the granite block coordinates are used for analysis of SSD based information such as vertexing.

3.8 Run History

E687 took data during three separate periods which are called the '88, '90, and '91 runs, referring to the year they took place. The '88 run took $\approx$ 60 million hadronic triggers while the '90 and '91 runs each took about 250 million hadronic triggers.

During part of the 1990 run, there were timing problems in the muon proportional tube readout which caused the muon identification to be inefficient. There were also periods where the muon system was moved out of the detector to accommodate tests of the downstream experiment. These periods of no muon identification comprised about 40% of the 1990 luminosity and are removed for analyses involving muons.

Table 3.1. Spectrometer Layout

Device	z (center)	x extent	y extent
TARGET	-3.00	2.54	2.54
SSD1	4.56	2.48	3.50
SSD2	10.57	4.96	4.96
SSD3	16.59	4.96	4.96
SSD4	28.51	4.96	4.96
M1 US MIRROR	77.44	168.00	192.00
M1	220.95	175.26	273.05
(continued)			

Table 3.1. Spectrometer Layout (continued)

M1 DS MIRROR	370.17	168.00	192.00
PWC 0	403.14	38.10	63.50
C1	519.75	50.80	76.20
PWC 1	644.58	76.20	114.30
C2	757.00	76.20	114.30
PWC 2	879.18	76.20	114.30
OE	962.99	135.00	150.00
M2 US MIRROR	1091.43	168.00	192.00
M2	1238.11	175.26	273.05
M2 DS MIRROR	1383.52	168.00	192.00
OMX	1399.24	152.40	254.00
OMY	1416.94	152.40	254.00
PWC 3	1444.13	38.10	63.50
OMH	1474.56	152.40	243.84
OMV	1505.06	152.40	254.00
C3	1884.42	95.25	114.30
PWC 4	2285.88	76.20	114.30
HxV	2328.19	137.15	182.90
IE	2399.67	68.58	114.30
HC	2569.78	101.60	152.40
BGM	2430.32	12.70	11.43
(continued)			

Table 3.1. Spectrometer Layout (continued)

CHC	2778.00	22.86	22.86
IM SHIELD 1	2895.66	115.57	165.10
IM1X	2973.48	101.60	152.40
IM1Y	62993.21	101.60	152.40
IM1V	3012.52	106.68	152.40
IM1H	3036.07	101.60	152.40
IM SHIELD 2	3079.66	115.57	165.10
IM2X	3138.95	101.60	152.40
IM2Y	3158.09	101.60	152.40
IM2H	3178.25	101.60	152.40

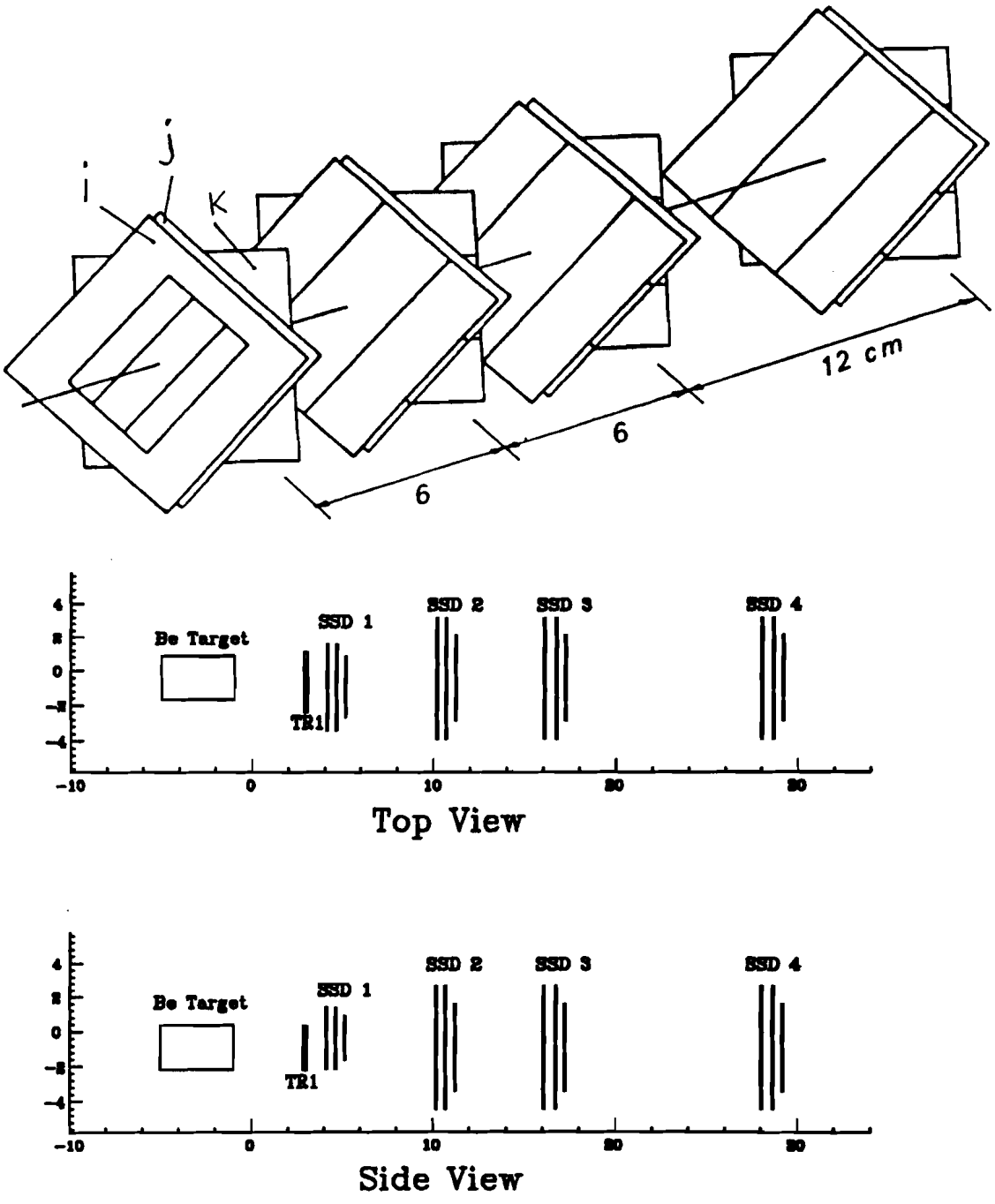

Figure 3.1. The layout of the SSD (Silicon Strip Detector) in E687.

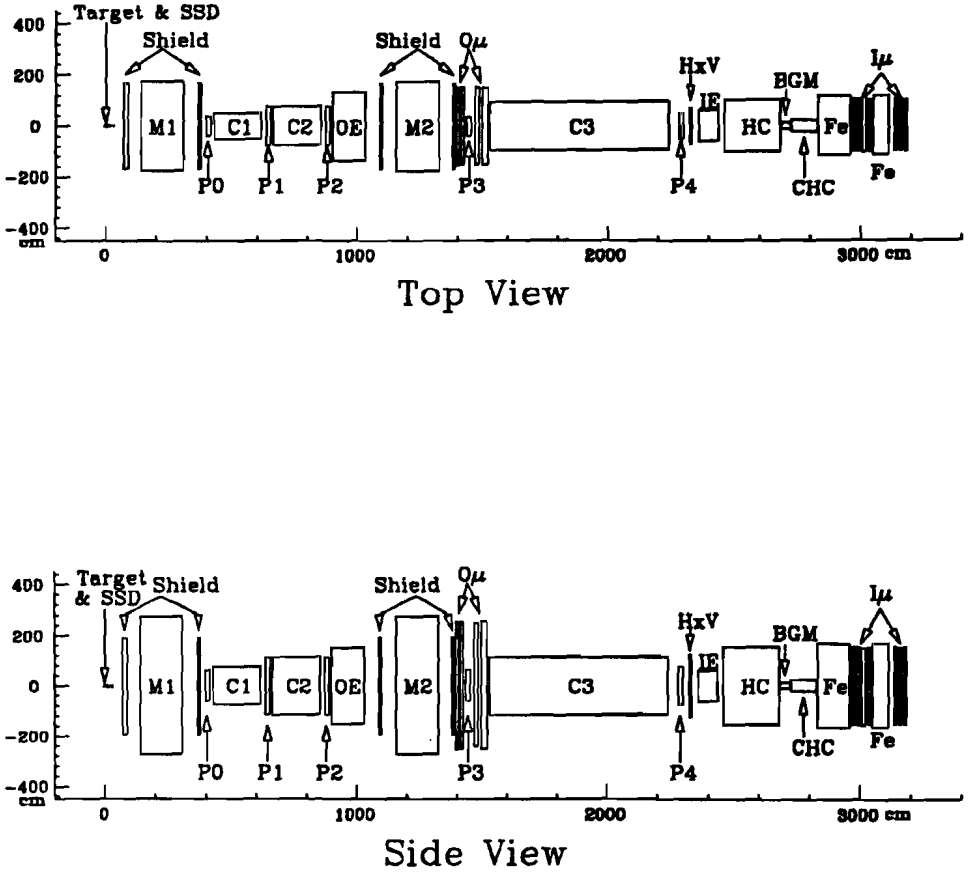

Figure 3.2. The layout of the E687 spectrometer. The magnets are M1 and M2, the Cherenkov detectors are C1-3, the MWPC's are P0-4.

Chapter 4

Reconstruction and Skims

The reconstruction process recduces the raw detector information, such as PWC hits, to produce higher level information such as the trajectory of particles and their momentum.

4.1 Reconstruction

The first step in the reconstruction is to identify microstrip tracks from the microstrip hits. These microstrip tracks are then combined into vertices. Tracks are found in the chambers, linked to the microstrip tracks, and momentum analyzed. Finally, particle identification including Cherenkov, muon and calorimeter analysis is added to the reconstructed tracks. Events most likely to contain charm are skimmed off onto separate tapes for distribution to the collaboration.

4.1.1 Microstrips

The twelve planes of the microstrips are arranged into three views. First, projections of particles trajectories are found in each separate view where they must leave at least three hits in the four planes in the view. The projections are then fit in three dimensional space and must pass a loose χ^2 cut. Since microstrip tracks are found independently from the PWC system, no momentum information is available and a least-squares fit is performed which ignores MCS (multiple Coulomb scattering) effects. The effects of not including MCS in the fit are discussed in depth in Chapter 5. In the case of two adjacent hits, the hit position is interpolated by weighting between the strip positions based on the relative pulse height recorded in the adjacent strips. Hits are allowed to be shared between tracks.

The resulting resolution of the transverse position of the track at the center

of the target is calculated to be (see Chapter 5):

$$\sigma_x = 11\mu\mathrm{m}\sqrt{1+\left(\frac{17.5GeV}{p}\right)^2}$$

$$\sigma_y = 7.7\mu\mathrm{m}\sqrt{1+\left(\frac{25GeV}{p}\right)^2} \tag{4.1}$$

Additional routines find wide angle tracks that leave hits in only two of the four microstrip stations.

4.1.2 VERTIC

Once the microstrip tracks are found, they are combined into vertices by a routine called VERTIC. The algorithm forms a trial vertex from all the tracks in the event. If the χ^2 is not acceptable then the track which contributes the most to the χ^2 is removed and the vertex is refit. The process of removing the worst track continues until a good vertex is left. The process is repeated on the tracks that were dropped, and iterated until an acceptable set of vertices, and possibly some unused tracks, remain. The fit only uses the microstrip hits and utilizes no MCS information.

VERTIC provides a primary vertex (the photon interaction vertex) for further reconstruction routines such as neutral vees, and for the momentum analysis of some categories of tracks.

VERTIC has been used to obtain very clean charm signals in decays such as $D^+ \rightarrow K^-\pi^+\pi^+$ by demanding the daughters appear in a single vertex with no other tracks. The secondary vertex is required to lie downstream of another VERTIC identified (primary) vertex and the D momentum vector (the sum of the daughter's momenta) must point to the primary vertex. For a charm vertex to be found as a separate vertex by this routine, it must be well separated from the primary vertex, must be separated from other tracks in the event and no charm

daughter track can point back to the primary vertex. The resulting signals are extraodinarily clean but the technique is inefficient at short lifetimes. In response, I have developed another vertexing technique which is more efficient since it is based only on the assumption that the D momentum vector points to the primary vertex. This vertexing routine, called SDVERT, will be described in detail in Chapter 6.

4.1.3 PWC's

Finding PWC tracks is done in several stages. First, projections of tracks in each view are found. Microstrip tracks are used to help search for projections in non-bend view (x). Projections downstream of M2 are connected to the upstream segment through the constraint that they intersect in the center of M2.

Sets of two projections that pass consistency cuts are combined with other projections. The projections are combined into three dimensional trajectories using a fit to all the chamber hits where no microstrip information is used. Tracks cannot be missing more than 5 hits total or more than 2 in each chamber. Cuts on the χ^2 are loose because no MCS information is used in this least squares fit.

At this stage there are only 3-chamber (P0 through P2, called "stubs") and 5-chamber (P0 through P4) tracks. For 3-chamber tracks we have no momentum information yet since no use has been made of the microstrip information. For the 3-chamber tracks we estimate the track parameters x, $x' = p_x/p_z$, y, and $y' = p_y/p_z$. The slopes and intercepts are specified for the track trajectory in the region between the magnets at P1 with the intercepts referenced to the center of M2.

For 5-chamber tracks we include a fifth track parameter, the bend angle in M2, $\delta'_y = y'_2 - y'_1$ where y'_1 is the y slope of the track before M2 and y'_2 is the slope after the bend in M2.

Additional recovery routines find tracks that only are accepted in P0 and P1 or attempt to extend a stub through M2 by including hits in P3 and P4. These

categories are small compared to the stub and 5-chamber track categories.

4.1.4 Linking

Most particles leave tracks in both the microstrip system and the chamber system. The process of connecting chamber tracks with the appropriate microstrip track is called "linking". A global fit to the hits from a microstrip track and the hits from a chamber track is used to test the hypothesis that the two track segments are consistent with being created by the same particle. A momentum dependent correction to the χ^2 to account for MCS is applied before the cut is made. We do not use this global fit to find the final track parameters because the lack of MCS information results in worse resolution than separate fits to chamber and microstrip segments. Because e^+e^- pairs produced are often found as a single track in the microstrips, we allow two chamber tracks to be linked to a single microstrip track.

4.1.5 Momentum Calculation

The momentum is found by various methods selected to exploit the available information about the track. Once the momentum is found, the track is refit including magnetic corrections. These include the effect of the magnetic field extending into the chambers and the fact that trajectories that enter the magnet at an angle or with a lower momentum will traverse more field, etc.

The basic problem is to propagate a particle of momentum $\vec{p}$ from the point $\vec{r_0} = (x_0, y_0, z_0)$ to the point $\vec{r} = (x, y, z)$. The momentum vector is described as a total momentum p, and slopes $\vec{r}' = d\vec{r}/dz$.

A straightforward application of the Lorentz force equation gives:

$$\frac{\vec{r}'}{\sqrt{1 + x'^2 + y'^2}} = \frac{\vec{r}_0'}{\sqrt{1 + x_0'^2 + y_0'^2}} + \frac{.29997}{p} \int_{z_0}^{z} \vec{r}'(\vec{x}_1) \times \vec{B}(\vec{x}_1)\, dz_1 \qquad (4.2)$$

This can be solved for the momentum from the intial and final slopes. The only problem is to do the integral. If we take on the largest component of the field

(B_x, which gives the kick in y) we find:

$$\frac{y'}{\sqrt{1+x'^2+y'^2}} = \frac{y'_0}{\sqrt{1+x'^2_0+y'^2_0}} + \frac{.29997}{p}\int dz\ B_x \tag{4.3}$$

Which gives, to a good approximation, for particles traversing the entire magnet, $p = K/(y' - y'_0)$. If we continue and solve for the position instead of just the slopes we have:

$$\begin{aligned} x &= x_0 + x'_0(z - z_0) \\ y &= y_0 + y'_0(z - z_0) + \frac{1+y'^2_0}{p}\sqrt{1+y'^2_0+x'^2_0}\int_{z_0}^{z} dz_1 \int_{z_0}^{z_1} B_x(\vec{x}_2)\ dz_2 \end{aligned} \tag{4.4}$$

In the actual implementation, equation 4.4 is expanded in powers of $1/p$ and various moments of the magnetic field which are precomputed.

Using this magnetic trace formalism, 5-chamber tracks are fit using least-squares including the bend angle in M2 and the momentum is found from that angle. The resolution, using the methods in Chapter 5, is:

$$\frac{\sigma_p}{P} = 1.4\% \left(\frac{P}{100\text{GeV}}\right)\sqrt{1+\left(\frac{23\text{GeV}}{P}\right)} \tag{4.5}$$

The second term in the resolution equation 4.5 reflects MCS uncertainty and is discussed in Chapter 5.

Stubs that are linked to microstrip tracks are fit with a global least-squares fit to the microstrip and chamber hits. For tracks that pass only through the high resolution region of the microstrips the resolution is:

$$\frac{\sigma_p}{P} = 3.4\% \left(\frac{P}{100\text{GeV}}\right)\sqrt{1+\left(\frac{17\text{GeV}}{P}\right)} \tag{4.6}$$

At high momentum this is dominated by y' resolution in the chambers but at low momentum it is dominated by y' resolution in the microstrips.

Tracks that are found only in P0 and P1 and are linked are fit the same way but have worse resolution because there is less lever arm for the measurement of y' after M1.

Tracks that do not pass through M2 and are not linked are assumed to eminate from a VERTIC vertex, and the momentum is estimated from the requirement that the particle originated from the vertex. If no VERTIC vertex was found, the track is assummed to eminate from the center of the target.

4.1.6 Cherenkov

After the tracks are found and their momentum analysed, the Cherenkov analysis determines which of the five possible long-lived particles is the most likely hypothesis. For each track, the predicted light yield in each cell of each Cherenkov counter is calculated using the hypothesis that the particle is a pion if $P > P_\pi$ and an electron if $P < P_\pi$ where P_π is the pion threshold of the counter. The cells of each counter are classified as either on or off according to the phototube response as read out by ADC's.

For each track in each counter, the predicted light yield in each cell is combined with knowledge of whether that cell is on or off to provide identification. If any light is predicted in a cell and that cell is on, that track is called on in that counter. If there is significant light predicted but all cells are off, the counter is called off for that track. If two or more tracks have a prediction for a cell and that cell is on, the counter is called confused because we don't know which track produced the light.

The pattern of counters which are on or off is combined with the momentum information to determine which particle hypothesis the Cherenkov response is consistent with. The considered hypotheses are electron, pion, kaon, or proton. Muons are not separated from pions because their thresholds are so close. The Cherenkov response is summarized by a word where bit 0 is on if the response was consistent with an electron, bit 1 for pion consistency, bit 2 for kaon consistency,

and bit 3 for proton consistency. Possible outcomes include definite categories, such as 4, which would be kaon definite, ambiguous categories such as 12, which would be kaon-proton ambiguous, or 0, which means the system found inconsistent responses in the different counters. A result of 15 means the Cherenkov system could provide no information. Table 4.1 shows the Cherenkov identification for the different particles and momentum ranges for 5-chamber tracks and Table 4.2 is the same for stubs. We have the capability of separating kaons from pions in the momentum range 4.5 to 61.8GeV/c if it is a 5-chamber track and from 4.5 to 29.8GeV/c if it is a stub.

Table 4.1. Cherenkov Identifications for 5-Chamber Tracks

p (GeV/c)	e	π	K	p
0.0 - 4.5	1	14	14	14
4.5 - 16.0	1	2	12	12
16.0 - 17.4	1	2	4	8
17.4 - 56.5	3	3	4	8
56.5 - 61.8	3	3	12	12
61.8 - 117.0	7	7	7	8
117.0 -	15	15	15	15

Table 4.2. Cherenkov Identifications for Stubs

p (GeV/c)	e	π	K	p
0.0 - 4.5	1	14	14	14
4.5 - 8.4	1	2	12	12
8.4 - 16.0	3	3	12	12
16.0 - 29.8	3	3	4	8
29.8 - 56.5	7	7	7	8
56.5 -	15	15	15	15

Several Cherenkov cuts are commonly used in our analyses. When high statistics are needed, we cut only on the kaon, requiring ID=12 ($K-p$ ambiguous) if $P < 61.8$GeV/c or ID=7 ($\pi/K/p$ ambiguous) if $P > 61.8$GeV/c. This is called the KP7 cut. If we need somewhat cleaner signals we use K/p ambiguous only. This is about 80% efficient compared to $KP7$. It is almost never advantageous to go all the way to K only (called Kdef) because it is only about 40% as efficient as KP7. Using KP identification often eliminates a reflection where a π is being used as a K such as in the $K2\pi$ background to $KK\pi$. In some cases we also put requirements on π's. Here typical cuts are ID$\neq 4, 8, 12$ (not-heavy), π bit set in the ID word (pi-con), or ID$= 2, 3$ (pi-identified).

4.1.7 Vees

The decays $K_s \rightarrow \pi^+\pi^-$ and $\Lambda_0 \rightarrow p\pi$ are common in our data. Because these are neutrals decaying to two charged daughters, they are referred to as vees. Because of their long decay length, there are several regions where these can be reconstructed. These decays are useful as a source of particles with known identities to study particle identification. They are also used to reconstruct charm decays such as $D^0 \rightarrow K_s\pi^+\pi^-$.

About 10% of the $K_s \rightarrow \pi^+\pi^-$ decays are found with decay vertices upstream of the first microstrip station. We run SDVERT (see Chapter 6) to find a production vertex for the vee which may be either the primary vertex or a secondary, charm vertex. A very clean sample can be found by requiring the decay vertex to be separated from the primary vertex.

About 80% of the K_s decays are found with the decay vertex downstream of the microstrips and upstream of P0. No microstrip information is available. The daughters may be either two stubs, a 5-chamber track and a stub, or two 5-chamber tracks. The vees are fit using a MCS corrected fit with the constraint that the neutral was produced at the primary vertex. This fit constrains the daughters of the neutral to intersect using a routine that can trace a charged particle to anywhere in M1. A powerful cleanup cut for these K_s's is to require

that the fit converged and the confidence level is good. We also typically require that the vee has a significant opening angle in x which eliminates the background from e^+e^- pairs.

Additional routines find vees that decayed in between the first and second microstrip station or downstream of P0.

4.1.8 Muons

Tracks that are found to have traversed P4 are analysed to see if they are consistent with leaving hits in the inner muon system. The track is projected to each muon plane which is searched for hits within 3 times the average multiple scattering radius. A minimum of three hits is required if $P < 30$ GeV/c and 5 hits if $P > 30$ GeV/c. A hit may be in the scintillator planes or in the proportional tubes.

4.2 Processing History

The reconstruction process is very CPU intensive. A farm of several dozen IBM RS600 RISC machines located at Fermilab was able to complete the reconstruction in about one year. Since most of the code was developed on the Vax, we had to port and verify the code on the unix system. The most critical verification was done by operating on an output tape produced on the RS600, re-reconstructing it on the Vax and comparing the high-level results such as momentum of tracks on a track by track basis. We can characterize the discrepancies as being on the 1% level and mostly in non-critical cases where the result is poorly measured or sensitive to roundoff errors.

4.3 Skims

Because the E687 reconstructed data set consists of about 4000 8mm tapes, direct distribution to the collaboration for analysis is prohibitive. We handled this problem by creating smaller data summaries (DST's) for the subset of events which are likely to contain charm.

4.3.1 DST's

When an event is reconstructed, the output contains considerable information that is not generally needed for high-level analysis. (This information is useful for developing reconstruction routines or reprocessing.) To greatly reduce the number of tapes needed for distributing the skims, the events are summarized on data summary tapes (DST's). This also greatly reduces the subsequent processing time.

The reduction in the number of tapes and the time to process them is approximately a factor of 10. Critical information such as track momentum vectors and Cherenkov identifications are kept but information such as PWC hits and ADC's are dropped.

4.3.2 All Charged Skim

For all charged decays such as $K\pi$ or $K2\pi$ we run the candidate driven vertexer (see Chapter 6) and make minimal cuts on mass, Cherenkov identification and ℓ/σ. These cuts vary according to the state. We take all events that pass these cuts. With this skim we can accept all charm events with any useable signal so this skim is 100% efficient for useful, fully reconstructed charm states.

The results of the vertex-finder as well as the mass of the candidate and other relevant information is stored on the tape for very fast subskimming and processing later. This skim is called the EZDEE skim.

4.3.3 Global Vertex Skim

Since charm states have a lifetime which is characterized by decay lengths on the order of 1cm, we expect charm events to have secondary vertices separated from the primary vertex. The global vertex skim requires evidence for secondary vertices.

Specifically, all combinations of pairs of tracks are formed into vertices. Only vertices with a confidence level greater than 1% are kept. If any two vertices

are separated by more than a minimum number of standard deviations in their z positions, the event is excepted. The requirement was 3.0 in the '88 data and 4.5 in the '90-'91 data.

The purpose of this skim is to accept decays which are not fully reconstructed such as $K\pi\mu\nu$ and $K\pi\pi^0$.

Chapter 5

Error Calculations

In this chapter we discuss the calculation, testing, and application of measurement errors. The quantities we are concerned with are the slopes and intercepts of tracks in the microstrips, slopes and intercepts of tracks in the PWC's, and momentum. We will also propagate the errors into quantities calculated from these track parameters.

The measurement error of track parameters can vary widely from track to track, depending on the topology and momentum of the track. Error calculation is critical for extracting the maximum information from an event with the maximum efficiency. For example, if we want to require that two tracks intersect we could require that their distance of closest approach is x microns. If the measurement error varies widely, then this cut will be inefficient for tracks with large measurement errors and, at the same time, it will be very loose for tracks with small measurement error, introducing background. If we can instead require that the distance of closest approach is less than, say, 3σ then the cut will have the same efficiency for all classes of events and will not introduce any unnecessary background. Because the cut becomes uniformly efficient, it is also less sensitive to biases and model dependence.

5.1 Description of Errors

Three sources of measurement error include pattern recognition (and efficiency), resolution, and multiple Coulomb scattering (MCS). Errors from pattern recognition occur when microstrip or chamber hits are assigned to the wrong particle track or some hits are missing. This may occur when hits are lost due to inefficiency or additional hits are present due to noise or unfound particles. These errors are unavoidable but can be minimized by careful choice of algorithms and cuts. They cannot be easily calculated and we rely on the Monte Carlo to simulate their effect. Pattern recognition typically results in small non-Gaussian tails.

We will not discuss this source of errors further except when they appear in tests of error calculations.

The second source of error is resolution. If we find a certain particle leaves a hit in a microstrip plane, we only know that track's position to the width of the strip. While our measured position is taken to be the center of the strip, the true position of the particle will have a square distribution with the width of the strip. If the width of the strip is Δ then the variance of the this distribution is $\Delta^2/12$. As we discuss later, the track parameters are deduced from a fit to the hit coordinates. The deviation in track parameters from true track parameters therefore represents a convolution of the many coordinate deviations, each of which has a "square" measurement error. The central limit theorem says that only the variance is relevant and the fit deviations approach Gaussian distributions.

Approximately 20-30% of the time the particle leaves hits in two adjacent SSD strips. In these cases the intercept is known, in principle, with a factor of two better precision compared to the case of no adjacencies. When adjacent strips fire, the measurement is taken to be the position between the strips. We find from studies of the data that it is not a serious approximation to ignore adjacency effects in calculating resolutions.

The third source of error is MCS (Multiple Coulomb Scattering). This occurs when a charged particle passes through a material and is deflected through many Coulomb collisions with the nuclei of the material. It is strongly dependent on particle momentum.

5.1.1 Basic Covariance Matrix

In this section we describe the calculation of the track parameter covariance matrix for a particle passing through a system of transverse measurement planes with a finite resolution.

This method is applied to the microstrip system where the fit parameters are (x, x', y, y'), the chamber system where the fit parameters are $(x, x', y, y', \delta y')$,

and, in some cases, to both systems. The intercepts x and y are the track positions at the coordinate system position $z = 0$ which is a point near the first microstrip station in the granite block coordinate system. The slopes are defined as $x' = p_x/p_z$, and $y' = p_y/p_z$. $\delta y'$ may be the y bend in M1 or M2, defined as the y slope downstream of the bend minus the y slope upstream of the bend.

Let us call the coordinate of the i'th plane X_i. For simplicity we will express these coordinates in units of "wire numbers" with "wire spacing " Δ_i. The random deviation of coordinate X_i (in a Gaussian model) is:

$$\delta X_i = \frac{1}{\sqrt{12}} \mathcal{G}_i + \frac{1}{\Delta_i} \sum_{m=1}^{i} d_m(P)\ (Z_i - Z_m)\ \mathcal{G}_m\ \sqrt{2}\ cos\ (\Phi - \phi_i) \qquad (5.1)$$

$$\text{Where } d_m(P) = \frac{0.014}{P}\sqrt{t_m} \quad \text{with } P \text{ in GeV/c}$$

The $\mathcal{G}_j$ values are uncorrelated, normalized Gaussian random numbers which (averaging over many tracks) obey:

$$< \mathcal{G}_i\ \mathcal{G}_j\ >= \delta_{i,j} \qquad (5.2)$$

The first term of equation 5.1 represents the coordinate error due to finite granularity. The Central Limit Theorem tells us that Gaussian distribution describes the δX_i deviations of fitted tracks in the limit of a large number of planes. The subsequent terms of equation 5.1 model the effects of MCS on a track of momentum P (in GeV/c) by all matter "slabs" located upstream of the i'th plane ($Z_m < Z_i$). The m'th matter slab has a thickness (in radiation lengths) of t_m. The MCS error is normalized to the "wire spacing" of the i'th plane, Δ_i. The multiple scattering is directed in a random Φ direction with respect to ϕ_i , the read-out direction of the i'th plane. The presence of the $\sqrt{2}$ multiplying the cosine is present in order to convert from the "projected" MCS error factor of 0.014 (in the $d_m(P)$ function) to a "half cone" factor reflecting both projections.

Correlating δX_i with δX_j and averaging over ϕ we obtain the coordinate correlation matrix:

$$C'_{ij} \equiv < \delta X_i \, \delta X_j > = \frac{\delta_{i,j}}{12} + \frac{cos\ \phi_{ij}}{\Delta_i \Delta_j} \sum_m d_m^2(P)\ (Z_i - Z_m)\ (Z_j - Z_m) \quad (5.3)$$

where ϕ_{ij} is the angle between the read out directions of the i'th and j'th plane. Equation 5.3 follows from equation 5.1 and the trig identity:

$$\frac{1}{2\pi} \int_0^{2\pi} d\Phi\ cos(\Phi - \phi_i)\ cos(\Phi - \phi_j) = \frac{cos\ (\phi_i - \phi_j)}{2} \quad (5.4)$$

Equation 5.3 means that the coordinates measured by independent planes are correlated due to MCS from the matter upstream of the most upstream coordinate.

There is a subtlety in deciding over which slabs should be summed in equation 5.3. The sum depends on at which point one wishes to make the best estimate of the track parameters. If the result of the fit is intended to give the best track parameters and errors for the particle at the vertex point, then the sum over materials would include the remaining part of the target and the sum would be continued over all slabs upstream of planes i and j. If the result of the fit is to give the best parameters and errors for the particle just downstream of the target then the sum would be over all slabs downstream of the target but upstream of planes i and j. If the result of the fit is intended to give the track parameters downstream of the microstrip than one essentially sums in reverse and includes all slabs (including microstrip planes) downstream of planes i and j but upstream of the position where the "true" track parameters are to be measured.

We now proceed to describe the linear fit used to find track parameters from the set of measurements. We will use the repeated index summation convention and use Roman indices for plane numbers and Greek indices for track parameters. Let us denote the track parameters as t_α , the transport matrix which

relates plane coordinate and track parameter as $T_{i\alpha}$, and the coordinate covariance matrix as C. We note that C may be either the correct covariance matrix of the hits, C', or it may be the coordinate covariance matrix ignoring MCS, $C^{-1}_{i,j} = 12\ \delta_{ij}$. The effects of these two choices is the central result of this section and will be discussed below. The transport equation and track parameter χ^2 which is minimized in track fitting are given by:

$$X_i = T_{i\alpha}\ t_\alpha\ ,\ \ \chi^2 = C^{-1}_{ij}\ (T_{i\alpha}\ t_\alpha - X_i)\ (T_{j\beta}\ t_\beta - X_j) \tag{5.5}$$

The minimization condition is:

$$\frac{\partial \chi^2}{\partial t_\alpha} = 2\ C^{-1}_{ij}\ (T_{i\beta}\ t_\beta - X_i)\ T_{j\alpha} = 0 \tag{5.6}$$

The solution to equation 5.6 can be written as:

$$t = H^{-1}V \quad \text{where the H and V components are :}$$

$$H_{\alpha\beta} = C^{-1}_{ij}\ T_{j\alpha}\ T_{i\beta}\ \ ,V_\alpha = T_{j\alpha}\ C^{-1}_{ij}\ X_i \tag{5.7}$$

It is useful to write two forms of the track parameter solutions in component form using two sets of dummy indices:

$$t_\alpha = H^{-1}_{\alpha\beta}\ V_\beta = H^{-1}_{\alpha\beta}\ T_{j\beta}\ C^{-1}_{ij}\ X_i$$

$$t_\delta = H^{-1}_{\delta\gamma}\ T_{l\gamma}\ C^{-1}_{kl}\ X_k \tag{5.8}$$

Equation 5.8 leads easily to a component form for the track parameter covariance matrix E:

$$E_{\alpha\delta} \equiv <\ \delta t_\alpha\ \delta t_\delta\ > = H^{-1}_{\alpha\beta}\ T_{j\beta}\ C^{-1}_{ij}\ <\ \delta X_i\ \delta X_k\ >\ C^{-1}_{kl}\ T_{l\gamma}\ H^{-1}_{\gamma\delta}$$

$$= H^{-1}_{\alpha\beta}\ T_{j\beta}\ C^{-1}_{ij}\ C'_{ik}\ C^{-1}_{kl}\ T_{l\gamma}\ H^{-1}_{\beta\gamma} \tag{5.9}$$

Note in equation 5.9 that we have made a distinction between the *fit* covariance matrix C and the *true* covariance matrix C'. In practice the *fit* matrix is the co-

ordinate covariance matrix *neglecting* MCS ($C_{i,j}^{-1} = 12\ \delta_{ij}$). The true coordinate covariance matrix (C') *includes* MCS and is given by equation 5.3.

Equation 5.9 can be written in matrix form (using transpose symmetry of the H matrix) as:

$$E = H^{-1}\ \tilde{H}\ H^{-1} \quad \text{where} \quad \tilde{H}_{\beta\gamma} = T_{j\beta}\ C_{ij}^{-1}\ C'_{ik}\ C_{kl}^{-1}\ T_{l\gamma} \tag{5.10}$$

Using the symmetry of the C matrices (and re-dummying some indices), the $\tilde{H}$ matrix can be written in a form analogous to equation 5.7:

$$\tilde{H}_{\alpha\beta} = \tilde{C}_{ij}^{-1}\ T_{j\alpha}\ T_{i\beta} \quad \text{where} \quad \tilde{C}^{-1} = C^{-1}\ C'\ C^{-1} \tag{5.11}$$

Equation 5.10 and equation 5.11 give the result for the parameter covariance matrix (E) for the case where the assumed fit coordinate covariance matrix C differs from the true coordinate covariance matrix C' presumably because the fit leaves out a source of coordinate error such as MCS.

To explicitly review these central results, we have calculated the *true* error matrix for a set of track parameters which were found using a fit that *ignores* MCS. In this (first) case $C_{i,j}^{-1} = 12\ \delta_{ij}$ and the tracks parameters (t) and their error matrix (E) is:

$$t = H^{-1}V, \qquad H = T^tC^{-1}T, \qquad V = T^tC^{-1}X$$

$$E = H^{-1}T^tC^{-1}C'C^{-1}TH^{-1} \tag{5.12}$$

This is the scheme implimented in E687.

These errors will be somewhat larger than the optimal case where the fit matrix *includes* MCS ($C = C'$). Note this case requires inverting C' for each

track so it cannot be implemented on a large scale.

$$t = H^{-1}V, \qquad H = T^t C'^{-1} T, \qquad V = T^t C'^{-1} X$$

$$E = H^{-1} T^t C'^{-1} T H^{-1} \tag{5.13}$$

The final case is what happens if we simply ignore MCS everywhere. The fit will have the same results as the first case but now the errors will be underestimated. We do not use this scheme but may people do. in this case $C_{i,j}^{-1} = 12\ \delta_{ij}$ and the track parameters and their error matrix is:

$$t = H^{-1}V, \qquad H = T^t C^{-1} T, \qquad V = T^t C^{-1} X$$

$$E = H^{-1} T^t C^{-1} T H^{-1} \tag{5.14}$$

Here C is a constant so these error matrices are constants.

Finally we include a note on implementation. We see that equation 5.12 is of the form $E = K^t C' K$ where K is a constant matrix. From equation 5.1, C' has the form $C'_{ij} = \delta_{ij}/12 + a_{ij}/p^2$, a constant part and a momentum dependent part. Therefore when we calculate E, we actually use the form:

$$E_{ij}(P) = \sigma^2_{ij,\infty} \left(1 + \left(\frac{P_*^2}{P^2}\right)\right) \tag{5.15}$$

where P_* is called the effective momentum and is the momentum where MCS effects are the same scale as granularity effects.

5.1.2 Momentum Error

For 5 chamber tracks (PWC tracks that are measured both upstream and downstream of M2) the momentum is determined through the bend in M2. The track parameters, $(x, x', y, y', \delta y')$, have been fit to the 20 planes of the PWC

system. The calculation of section 5.1.1 applied to the PWC system gives the error on $\delta y'$ which is propagated to an error on p:

$$\sigma_P = 1.351 \times 10^{-4}(\mathrm{GeV/c})^{-1} P^2 \sqrt{1 + \left(\frac{23.00\mathrm{GeV/c}}{p}\right)^2} \qquad (5.16)$$

For 3 chamber tracks there is only the segment between M1 and M2 which is fit to a straight line. If the track is associated with a SSD track then the SSD track is fit separately from chamber segment and the difference between y' in the SSD's and y' in the PWC's is used to find the momentum. The errors from each segment are propagated to find:

$$\sigma_P = 3.391 \times 10^{-4}(\mathrm{GeV/c})^{-1} P^2 \sqrt{1 + \left(\frac{16.96\mathrm{GeV/c}}{P}\right)^2} \qquad (5.17)$$

if the SSD segment is in the high resolution region and:

$$\sigma_P = 3.932 \times 10^{-4}(\mathrm{GeV/c})^{-1} P^2 \sqrt{1 + \left(\frac{14.67\mathrm{GeV/c}}{P}\right)^2} \qquad (5.18)$$

if the SSD segment is in the low resolution region.

5.1.3 Extrapolated Errors and Target MCS

The basis of vertexing is the transverse errors on a microstrip track when extrapolated to the region of the vertex.

First we note that the error in x and y are almost completely uncorrelated due to the symmetry of the microstrip geometry.

Table 5.1. Extrapolation Resolutions

	σ_∞	P^*
x ext	10.749 μm	15.03 GeV
y ext	7.741 μm	21.69 GeV

These values are for the measurements from the high-resolution regions of the SSD's and are extrapolated to the center of the target. The low resolution regions have twice the asymptotic resolutions and half the effective momenta. The effective momenta do not include MCS in the target or TR1 which is taken into account by an additional term.

We modify the asymptotic resolutions to calculate the extrapolation errors to Z_V's other than the target center. The forms used are:

$$\sigma_x^{(\infty)} = \sqrt{30.068 + 0.41589\ (Z_V - 10.335\text{cm})^2}\ \mu\text{m}$$

$$\sigma_y^{(\infty)} = \sqrt{15.021 + 0.20682\ (Z_V - 10.733\text{cm})^2}\ \mu\text{m} \tag{5.19}$$

where Z_V is the vertex location in granite block coordinates ($Z_V \approx -3$cm). MCS in the Be target is incorporated by adding an additional term in quadrature in both x and y:

$$\sigma_{Be} = \frac{1}{\sqrt{3}} \frac{.014\text{GeV/c}\ (Z_m - Z_V)}{P} \sqrt{\frac{Z_m - Z_V}{38.08\text{cm}}} \tag{5.20}$$

where Z_m is the downstream end of the target material in granite block coordinates. This term is found assuming the target is a continuous scatterer and the MCS is integrated through the target. Finally we add an independent MCS term in quadrature for TR1:

$$\sigma_{TR1} = 0.068\text{cm}\ \frac{.014\text{GeV/c}\ (3\text{cm} - Z_V)}{P} \tag{5.21}$$

The TR1 and target MCS contributions are comparable.

5.1.4 Unlinked Tracks

Since unlinked microstrip tracks have no chamber track associated with them, we do not know the correct momentum to use when calculating the errors on these

tracks. However, these tracks are useful because they help to pin down primary vertices. In order to find a default momentum for these tracks we used a Monte Carlo and compared the extrapolation resolution and to the prediction for various momenta. We found that a nominal momentum of 7GeV/c seems to produce a reasonably accurate errors.

The fact that this momentum produces a reasonable prediction does not imply that the average momentum of unlinked tracks is 7GeV/c. We feel that the resolution is probably unexpectedly good for these tracks because they are low momentum and large MCS might result in dropped hits after a large scatter.

5.1.5 f_{hi} and Missing Hits Approximations

When we calculate the track parameter's errors we, in principle, need to account for missing hits in equation 5.1. We also need to account for the fact that some hits are in the high resolution region while some are in the low resolution region.

To incorporate these effects completely correctly we would have to recalculate equation 5.12 with a new C and T for each track or store the results of the calculation for all combinations of missing hits and high/low resolution hits. The first method would be too CPU intensive while the second would require millions of prestored matrices.

Since most tracks have all or nearly all their hits present, we find that the calculation for this case serves as a good approximation for all tracks. For the hit resolution problem we make an approximation:

$$\sigma^2 = f_{hi}\sigma_{hi}^2 + (1 - f_{hi})\sigma_{lo}^2 \tag{5.22}$$

Where the errors marked "hi" and "lo" are the predicted error for the case of all high resolution and all low resolution hits respectively. This makes the approximation that it doesn't matter *where* the high resolution hits were, just *how many* there were.

With these final approximations, we are prepared to calculate covariance matrices for any track from two prestored momentum dependent matrices.

5.2 Tests and Applications of Errors

5.2.1 Mass Error

The uncertainty on a mass measurement can vary significantly with topology and momentum. We use the mass formula:

$$M^2 = (\sum E_i)^2 - (\sum p_{x,i})^2 - (\sum p_{y,i})^2 - (\sum p_{z,i})^2 \tag{5.23}$$

make the approximations:

$$\begin{aligned} E_i &\approx p_i(1 - M_i^2/2p_i^2) \\ p_{z,i} &\approx p_i(1 - (x'^2 + y'^2)/2) \end{aligned} \tag{5.24}$$

and propagate the errors from each set of daughter track parameters ($t_\alpha = x, x', y, y', p$):

$$\sigma^2(M^2) = \sum_i \partial M^2/\partial t_{\alpha,i}\ E_{\alpha\beta,i}\ \partial M^2/\partial t_{\beta,i} \tag{5.25}$$

Figure 5.1 shows a normalized mass plot for the golden modes.

5.2.2 Vertex Intercepts

The best test to compare our calculations of the anticipated SSD resolutions to the data involves measuring the distance from a given SSD track to the primary vertex, from which the candidate track has been removed. The anticipated x and y impact error should reflect both the uncertainty in the track as well as the uncertainty in the vertex. The deviation equation for the x intercept (x_i) for a given track to a given vertex is:

$$\delta(x - X_v) = \delta x_o + \delta x'\ Z_v + x'\ \delta Z_v - \delta X_v = \delta x + x'\ \delta Z_v - \delta X_v \tag{5.26}$$

Note that we have grouped the two variations $\delta x_o + \delta x'\ Z_v$ into a single variation δx_i which describes how accurately a given SSD track can be extrapolated back

to a fixed vertex plane (Z_v). Autocorrelating $\delta(x_i - X_v)$ and setting all correlations between track and vertex quantities to zero (since the track will be always removed from the vertex prior to vertex fitting) we get:

$$\sigma^2_{x-X_v} = \sigma^2_x + \sigma^2_{X_v} + x'^2\ \sigma^2_{Z_v} - 2\ x'\ <\delta X_v\ \delta\ Z_v> \qquad (5.27)$$

The σ_x represents the extrapolation error of the track whose computation in described in the previous section.

5.2.3 Test of The f_{hi} Approximation

We have plotted the vertex intercept variables (described in section 5.2.2) distributions for linked tracks with indicated cuts on f_{hi} or the fraction of hits in the high resolution region of the SSD. These plots provide an incisive test of our granularity weighting scheme. The widths are summarized in the below table:

Table 5.2. f_{hi} Dependence of Extrapolation Errors

f_{hi} cut	$(x - X_v)/\sigma$	$(y - Y_v)/\sigma$	M.C.$(x - X_v)/\sigma$	M.C. $(y - Y_v)/\sigma$
$f_{hi} = 0$	0.87	1.01	-	-
$0 < f_{hi} < 0.5$	1.12	1.09	0.90	0.95
$0.5 < f_{hi} < 1$	1.15	1.06	0.94	0.90
$f_{hi} = 1$	1.02	1.04	0.91	0.88

The granularity weighting scheme appears to do a surprisingly good job overall in reproducing the observed extrapolation errors. (Their are limited statistics for the case $f_{hi} = 0$ in Monte Carlo.)

5.2.4 Pair Removal

Many events contain e^+e^- pairs that come from multi-brem photons or from photons from a second electron within the event window in time. These pairs are produced very nearly along the direction of travel of the photon or z axis.

Many times we want to flag these pairs in order to reduce backgrounds. This is accomplished by asking if a track is consistent with being produced along the z axis:

$$\chi^2 = ((x' - x'_0)/\sigma_{x'})^2 + ((y' - y'_0)/\sigma_{y'})^2 \tag{5.28}$$

where x'_0 and y'_0 represent a small offset between our z and the beam direction. The confidence level distribution of this χ^2 is flat between zero and one. We identify pairs as those tracks which have $CL > 1\%$.

5.2.5 Matching

It is often necessary to ask if a particular reconstructed track in a Monte Carlo event corresponds to a particular generated track. We accomplish this by comparing microstrip track parameters ($t_\alpha = x, x', y, y'$) with generated parameters (t'_α):

$$\chi^2 = (t_\alpha - t'_\alpha)\ E^{-1}_{\alpha\beta}\ (t_\beta - t'_\beta). \tag{5.29}$$

The confidence level distribution of this χ^2 is reasonably flat between zero and one. We require $CL > 1\%$ to match a track. This confidence level distribution is shown in Figure 5.2.

This method of matching has an advantage over matching by comparing hits because it succeeds when the track was reconstructed correctly *within errors* which is a physics-driven criteria.

5.2.6 Vertex Fit

Most vertex fits are based on minimizing the distance of closest approach of the tracks. Because the tracks in our spectrometer all have very shallow angles, we make the very good approximation that the vertex can be found by minimizing the *transverse* distance of closest approach. The χ^2 of a fit for the vertex of N

tracks is then:

$$\chi^2 = \sum_{i=1}^{N} \left(\frac{x_v - (x_i + x_i' z_v)}{\sigma_{x,i}} \right)^2 + \left(\frac{y_v - (y_i + y_i' z_v)}{\sigma_{y,i}} \right)^2 \qquad (5.30)$$

where x_i' and x_i are the slope and intercept of the ith track and the fit parameters are the vertex position, (x_v, y_v, z_v). The σ's represent the extrapolation error on the track. They include effects of the error on the slope and the intercept and MCS in the target and TR1:

$$\sigma_x^2 = \sigma_{xx}^2 + 2z\sigma_{xx'}^2 + z^2\sigma_{x'x'}^2 + \sigma_{targ}^2 + \sigma_{TR1}^2 \qquad (5.31)$$

There is some explicit z dependence in this error and some implicit in the target and TR1 MCS terms. In principle, the fit could be iterated but we find there is no significant bias when we assume the errors are appropriate to the center of the target. Note that there is no correlation between the x and y terms in the χ^2 because of the symmetry in the microstrip geometry.

This fit is not the usual linear fit in several ways. First, the errors on the measured variables vary from event to event as opposed to, for example, hits in the PWC's which are assumed to have a constant measurement error determined by the wire spacing. Secondly, there is the $x'z_v$ term in the χ^2 which means the transport matrix contains the measured variables x' and y'. These two points mean that the fit matrix must be calculated and inverted on an event by event basis. Because it is only a 3×3 matrix, the inversion time is negligible. Despite these unusual characteristics, the fit is linear in the sense that it converges in one iteration (with the approximation that the errors are not dependent on z).

5.2.7 High Level Fits

It can be proven that in any fit, one should include as much information as available, provided we use the correct errors. If the errors are not completely

correct, it may actually improve resolution on the fitted variables if some information is ignored. This is the case with 5-chamber linked tracks. Since the least squares fits for the track parameters only use the infinite momentum errors for the hits and ignore MCS, it actually improves resolution to ignore the microstrip information when calculating momentum.

However, with the calculation presented above we can find the correct error matrices on the track parameters. Since we now have the full error matrix, we can include all the information and improve momentum resolution. So there are a hierarchy of possible resolutions. The best resolution would be achieved with a fit of track parameters to the chamber and microstrip hits with full covariance matrices including MCS. The second best resolution is achieved by performing separate fits to the chamber and microstrip segments without MCS. One could then refit the tracks to a global set of parameters using the computed track covariance matrix which incorporates MCS information. The worse resolution would be achieved with a fit of the global track parameters to the hits without any MCS information.

The first case is impractical since it involves the inversion of large matrices for every track. Since the second best is practical, we have implemented it and discuss the results here.

For 5-chamber tracks we have developed a fit where the the microstrip segment and chamber segment track parameters are the measured parameters and the global set of (x, x', y, y', p) is the set of fit parameters. One way of envisioning the improvement is to think of the momentum as being measured in both M1 and M2 instead of just in M2. Because the lever arm of the chamber system is so large, the slopes of the tracks are measured better than when just using the microstrip information. For stubs we get less improvement in the momentum resolution but gain some because of the constraint that the chamber and SSD segments intersect in M1.

We can take the process a step further and fit groups of tracks. For example,

if we have a $K\pi$ candidate, we could fit the decay vertex and all the sets of track parameters to the sets of track segments. This introduces the additional constraint that the tracks must come from a common point.

We have evaluated these fits on a $D^0 \to K\pi$ signal in data. Figure 5.3 shows the signal using the standard algorithms, with the individual track segments refit, and with the tracks refit including the vertex constraint. We can see there is a significant gain in using the refitted tracks, but there is little further gain using the vertex constraint.

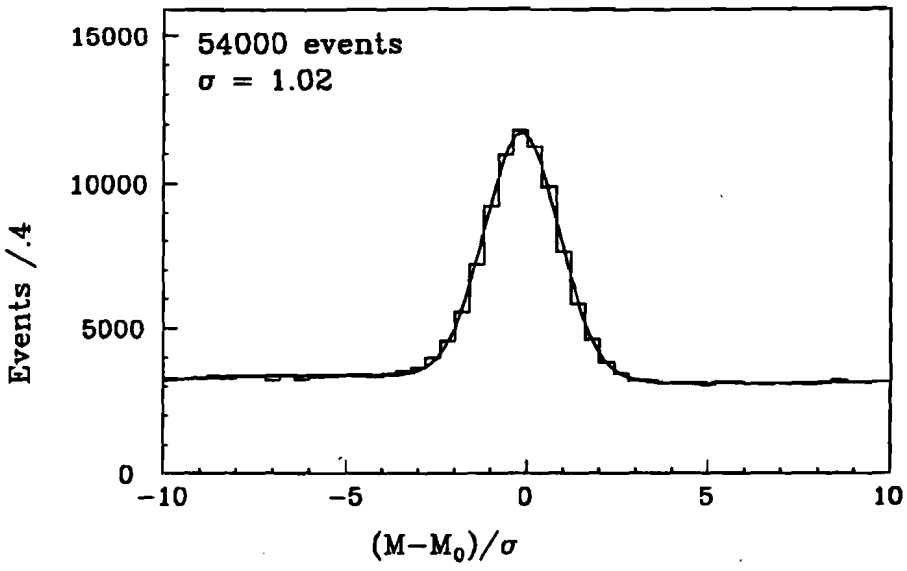

Figure 5.1. The normalized mass ($(M - M_0)/\sigma$) distribution for the combined golden mode signals, $Kn\pi$.

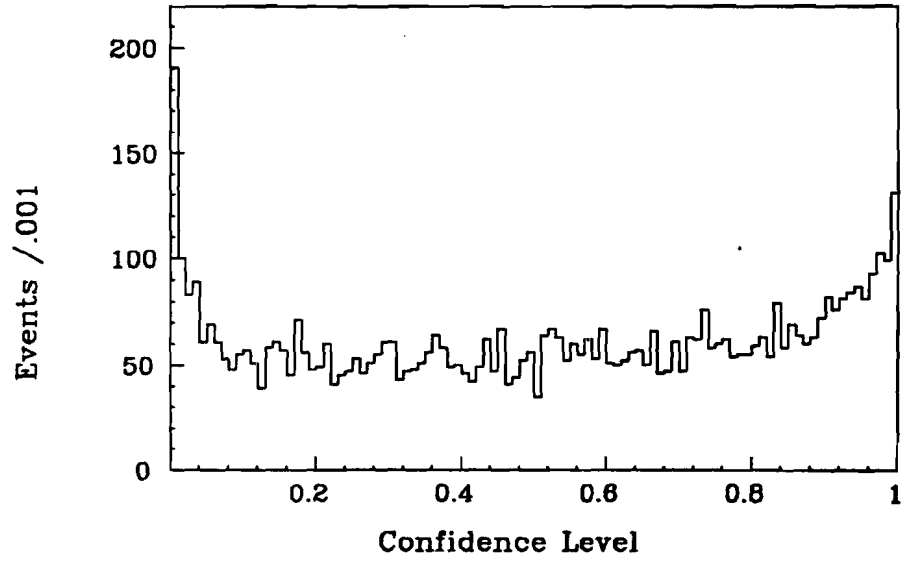

Figure 5.2. The confidence level distribution for the χ^2 used for matching reconstructed tracks to Monte Carlo generated tracks.

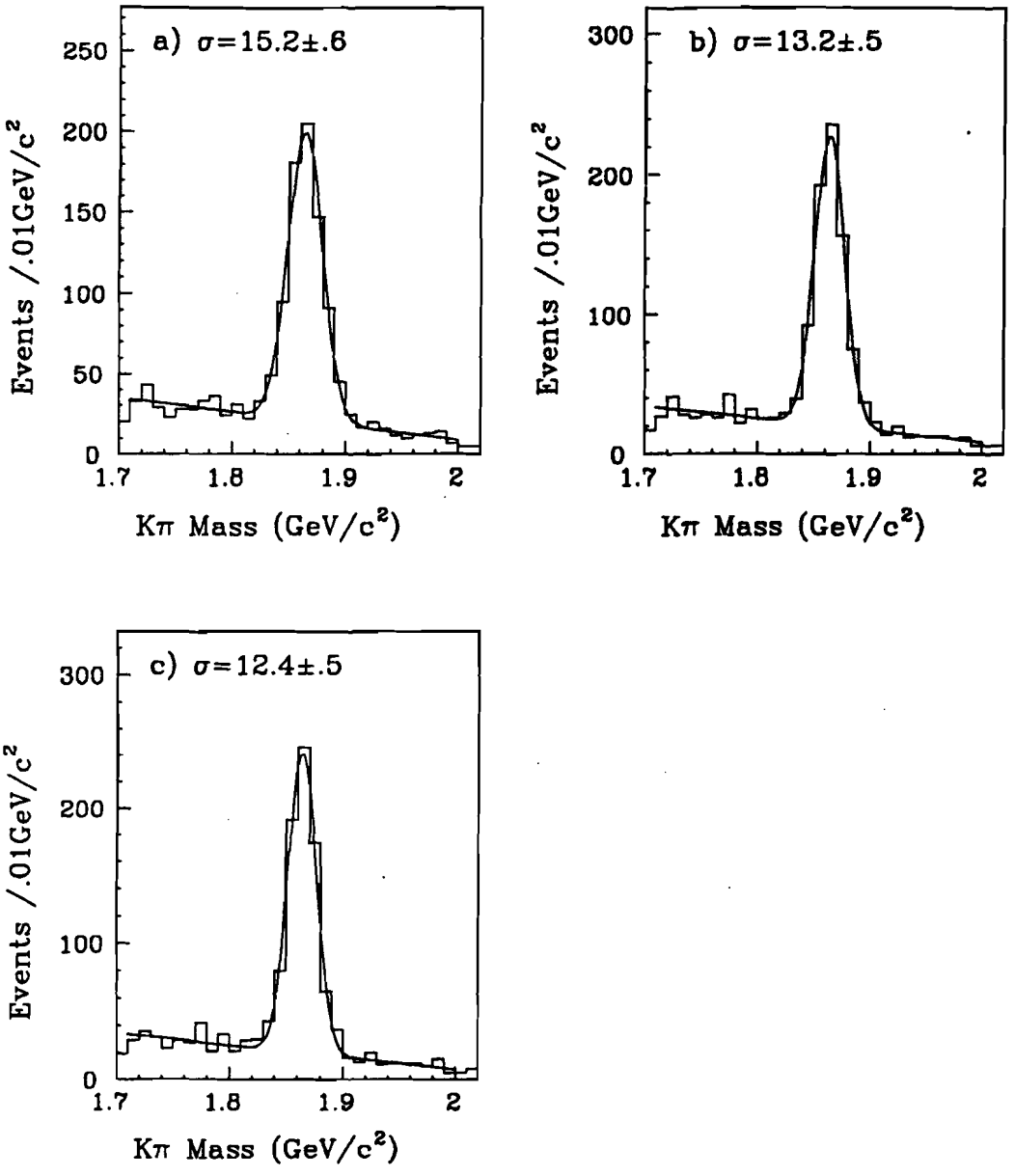

Figure 5.3. The invariant mass for a small sample of $K\pi$ for a) the standard algorithms, b) after refitting the daughter tracks, and c) after refitting the daughter tracks with the vertex constraint.

Chapter 6

Vertexing

E687 data is dominated by events where a hadronic interaction occurs but no charm is produced. In these events, all the charged particles originate from a single vertex. In events where charm is produced, the ground state charm particles typically travel a distance of .6-1.5cm before decaying because these charm particles decay weakly. A D accepted by the trigger and apparatus has an average momentum of about 100GeV/c implying a time dilation factor of $\gamma = E/M \approx p/M \approx 50$. Since the D^0 (D^+) proper time is τ =.42ps (1ps), one expects an average flight distance of $\ell = \tau\gamma c$ = .6cm (1.4cm).

The D is produced at the primary vertex (photon interaction point) along with an average of 2.2 charged tracks. A recoil charm particle is also produced to conserve charm in the strong interaction. The main purpose of vertexing is to exploit the lifetime of charm candidates (which creates the separation of primary and secondary vertices) to distinguish charm events from non-charm events.

This chapter discusses the vertexing scheme used in our analyses. This scheme uses the very good microstrip resolution to find charm candidates that are well separated from the primary vertex. The basic algorithm is to form a D track from the daughter tracks then search for the primary vertex which has to lay along the D track, somewhere upstream. The error calculations from Chapter 5 allow us to make cuts based on statistical significance of the detachment of the charm decay vertex from the primary vertex. This detachment is written ℓ/σ where ℓ is the separation and σ is it's error.

The set of routines is called Super DVERT or SDVERT. This collection of utility routines can be combined to address many specific vertexing needs.

We will discuss the basic algorithm, then the efficiency of the algorithm, and finally tests of the error calculations. We next discuss isolation cuts. These require that the candidate is isolated from other tracks in the event one way

or another and are found to be very effective in suppressing backgrounds. The next section addresses some special cases of the vertexing algorithm and the last section discusses an alternative vertexing scheme that is used for analyses where we don't know the D direction because not all the daughters are reconstructed.

6.1 Algorithm

A typical decay mode that we are investigating is $D^0 \rightarrow K\pi$. The K and π are reconstructed in the spectrometer where we measure their slopes and intercepts (x, x', y, y') in the microstrips and momenta, p, in the PWC system.

We then calculate the daughter's momentum vectors and combine them to form the D momentum vector. We calculate the secondary $(K\pi)$ vertex position in space using the fit described in section 5.2.6. Since the D must have passed through the secondary vertex position and we know the the D direction from the momentum vector, we can calculate the complete set of track parameters for the D, (x, x', y, y', p).

To calculate the error matrix of the D track parameters, we propagate the errors from the daughter track parameters. Since the propagation involves a non-linear fit for the secondary vertex, we do the propagation through finite differences. In other words, we vary each daughter track parameter $t_{\alpha,i}$ and find the effect on the D track parameter t^D_β to find the derivatives $D^\beta_{\alpha,i}$ then propagate using the matrix equation:

$$C = \sum_i D_i^t C_i D_i \tag{6.1}$$

where the sum is over daughters, C is the D track covariance matrix, and C_i is the covariance matrix of the daughter track as described in Chapter 5. These matrices are momentum dependent (include the effects of MCS). They are calculated assuming the daughter track was produced at the center of the target for the MCS calculation. In principle we could recalculate the daughter track error matrix based on the secondary vertex position but we find this is not necessary.

Once we have the D track parameters and their covariance matrix, we propagate once again and find the error on the transverse position of the D track at the center of the target. With this information the D track is ready to be included in a vertex fit with other tracks in the event.

Since the primary vertex must also lie along the D track, we proceed to cluster other tracks around the D vector to form a candidate primary vertex. The algorithm is to first form a subset of microstrip tracks that do not include the daughters of the D candidate. From this subset, we find all tracks that are consistent with forming a vertex with the D. A track is considered consistent if the confidence level of the vertex fit is greater than 1%. If no consistent tracks are found then the algorithm has failed and the candidate is rejected.

If only one intersecting track is found, then this single track is used for the primary vertex. ℓ is calculated as the 3-dimensional distance between the primary and secondary. If the primary is upstream of the secondary, $\ell > 0$, but if the primary is downstream, $\ell < 0$. The error on ℓ is propagated from the error on the two vertices. This is not statistically optimal since the the primary includes the D track which shares some information with the secondary vertex and this correlation is not considered.

If only two tracks are found to be consistent with forming a vertex with the D track then the algorithm checks if the D track will form a vertex with both tracks together. If this is not true then the track with the higher confidence level in the vertex fit is chosen as the primary vertex and ℓ/σ is calculated for the one-track case.

If both tracks together with the D form a good vertex then the two tracks are taken as the primary vertex. Now the D track can be removed from the primary vertex, the vertex is refit and a statistically correct ℓ/σ is calculated.

Now we are left with the case of more than two tracks are consistent with forming a vertex with the D track. In this case, all pairs of tracks are fit together with the D track. If no pairs of tracks form a good vertex, then the single track

with the highest confidence level is taken as the primary. If one or more pairs of tracks are consistent with form a vertex with the D, then the pair with the highest confidence level from the fit is chosen for further processing. The last stage is when the routine attempts to add more tracks to the primary (together with the selected pair and the D) as long as the confidence level of the primary vertex remains over 1%. The tracks are added one at a time starting with the one that contributes the least to the χ^2 of the vertex.

Because of the last step, the confidence level distribution of the primary is not flat but peaked toward low confidence level.

Typically we require that DCL, the confidence level that the daughters form a good vertex, is greater than 1%. This cut removes most background from events where the daughters did not truly originate from the same vertex while it should be 99% efficient.

The range of ℓ/σ cuts varies widely depending on how much rejection is needed. This cut can range from $\ell/\sigma > 0$ for $K\pi$ D^*'s which yields a signal to noise of 1, to $\ell/\sigma > 20$ for $K2\pi$ which yields a signal to noise of approximately 20.

Figure 6.1 shows a $K2\pi$ mass plot for all events, with a DCL>.01 cut, with a cut $\ell/\sigma > 8$ and both. The figure shows that *both* cuts are needed to really bring out a signal. The last plot in the figure show the effect of an isolation cut which is discussed below.

6.2 Tests of the Algorithm

Since it is possible to see a $D^0 \rightarrow K\pi$ signal with a D^* cut and no vertexing requirements, we can test the absolute efficiency of the algorithm. Figure 6.2 shows such a signal with the sole requirement that the $K\pi$ forms a good vertex. Figure 6.2 shows the signal divided between events that pass the requirement that the algorithm succeeded and those that didn't. We conclude that the algorithm is very efficient, $\epsilon > .96$ at the 90% confidence level.

Figure 6.3 shows how the signal survives the DCL cut for data and Monte Carlo. Ideally, these plots should be straight lines going through (1,0). The extent to which they are not straight lines indicates the sensitivity to the assumptions we made in computing the errors. A discrepancy between data and Monte Carlo is noted at low DCL which gets stronger as the multiplicity in the secondary vertex grows. We believe that this problem is probably due to pattern recognition and noise problems in the track fitting which produces non-Gaussian tails in the fitted track parameters

Figure 6.4 shows the distribution of ℓ/σ for a small sample of $K\pi$ candidates just above or below the D mass. This plot is completely dominated by non charm events where we expect $\ell = 0$ and therefore ℓ/σ should be a unit Gaussian if we understand our errors. The data agrees well the displayed fit which is a Gaussian with a width of 1.01. This figure also demonstrates the huge level of non-charm background that we can eliminate by requiring our candidates pass an ℓ/σ cut.

Figure 6.5 shows the survival of a $K2\pi$ signal as a function of the ℓ/σ cut. Overplotted in this figure is the Monte Carlo prediction. It is interesting to note that the logarithmic slope of this plot can be used as an operational definition of our experimental charm proper time resolution. In our experiment, the proper time of a decay (t) is measured directly from the detachment (ℓ) between the primary and secondary vertex according to $t = (M/Pc)\ell$. Because the fractional error on ℓ is much larger than the fractional error on charm momentum P we have the relationship $\sigma_\ell/\ell = \sigma_t/t$. We next show that σ_t is expected to be independent of charm particle momentum.

Because the microstrips measure the transverse separation between tracks, we can show that the ability to measure the longitudinal position of a vertex is proportional to θ^{-1} where θ represents the root mean square angle between any two tracks in the vertex. In the ultrarelativistic limit, all angles scale inversely as the momentum of the charm particle which implies that the error in longitudinal position of the secondary vertex should be proportional to the charm particle

momentum. At high enough charm momentum the secondary vertex error will dominate over the fixed primary vertex error and one will have a detachment error which is proportional to the momentum ($\sigma_\ell = \hat{\sigma}\ P$). Substituting into $\sigma_t = (M/cP)\sigma_\ell$, we have a constant proper time resolution $\sigma_t = (M/c)\hat{\sigma}$ which depends the charm particle mass and decay topology.

Using the relationship $\sigma_\ell/\ell = \sigma_t/t$, we can recast the lifetime survival expression for a particle with a mean lifetime of τ into a detachment survival expression:

$$N(\text{time } > t) = N_0\ e^{-t/\tau} \rightarrow N(\text{detach } > \frac{\ell}{\sigma_\ell}) = N_0\ exp(-\frac{\sigma_t}{\tau}\ \frac{\ell}{\sigma_\ell}) \qquad (6.2)$$

From the logarithmic slope of Figure 6.5 we calculate a proper time resolution which we find to be .045ps. Since increasing the charm particle mass gives decay secondaries a larger p_t with respect to the parent D direction, $\theta \propto M$ and $\hat{\sigma}/M$ should be approximately constant and universal. We therefore expect, and observe, that our proper time resolution of about 0.045 ps is approximately true for all charged particle charm decays where all daughters are reconstructed in the microstrip system.

6.2.1 Primary Vertex Contamination

We have found that there is significant contamination of recoil charm tracks in the primary vertex. Sometimes the recoil charm particle decays near the primary vertex so that its tracks are indistinguishable from the primary vertex. Also the decay may be well separated from the primary but some daughter tracks may point back to the primary. In these cases, there is no harm in including the recoil charm tracks in the primary, however, there is also the case where the primary vertex in an event isn't well represented with many charged tracks but the recoil decay is. If the recoil decay is also near the D seed track, the recoil charm decay may be found as the primary vertex, or the recoil decay may pull the measured primary vertex downstream from the true primary.

Figure 6.6 shows the distribution of the measured proper time minus the true proper time divided by the expected error for a $K2\pi$ Monte Carlo. The pulling of the primary can be seen as a longer tail on the negative side.

If we find a sample of decays where we reconstruct both the charm particle and the recoil charm particle, we can explicitly see how often the recoil charm tracks are included in the primary vertex. Figure 6.7 shows the distribution of the number of linked tracks in the primary vertex for all events compared to events where we can remove the recoil charm tracks. The average number of tracks for these two distributions are 3.3 and 2.2 respectively, indicating that we include about one track from the recoil charm decay on average. This is in good agreement with our Monte Carlo.

6.3 Isolation cuts

We have found that requiring the secondary vertex to be isolated is an effective way to improve signal to noise. The first style of isolation cut, called CL1, requires that the confidence level that any of the daughter tracks is consistent with coming from the primary vertex is less than a cut, typically 20-50%. This cut is designed to remove events where tracks from a charm fragment are unintentionally combined with tracks that come from the primary vertex to form a charm candidate. By requiring that the daughters are not consistent with coming from the primary vertex we can limit this background. We find that we cannot cut very hard on CL1 because it becomes too inefficient, cutting signal where one the daughters accidentally points to the primary vertex.

The second isolation cut, called CL2, requires that the secondary vertex is not consistent with forming a vertex with other tracks in the event, not including the tracks in the primary. We loop over the microstrip tracks that are not in the secondary or primary and fit them in a vertex together with the secondary and require that the largest confidence level is less than .1-1%. This cut is removes background from higher multiplicity decays (at large detachments, charm is the major background). This cut is requiring that the recoil charm decay is far from

the candidate vertex. While this is an implied ℓ/σ cut, it is not exclusively an ℓ/σ cut and it's effectiveness is not well understood. However, the cut is extremely effective at improving signal to noise with little loss in yield and is used extensively in this thesis and in other analyses in E687.

Figure 6.8 shows the effectiveness of the isolation cuts. We plot the signal yield *vs* signal to noise for various isolation cuts.

6.4 Other capabilities of SDVERT

Although these extensions of SDVERT are not used in this thesis, they have been used extensively throughout the collaboration to obtain charm signals in such special decay modes as $D^0 \to K\pi\pi^0$, $D^+ \to K_s\pi$, $\Omega_c^0 \to \Omega^-\pi^+$ [15], $\Xi_c^0 \to \Xi^-\pi^+$ [15], and $\Xi_c^+ \to \Xi^-\pi^+\pi^+$ [16]. The Ω is seen as a ΛK and the Ξ is seen as a $\Lambda\pi$. We include this section for completeness.

6.4.1 One Prong

A one-prong decay is a mode that has complete direction information but incomplete intercept information such as $D^0 \to K_s\pi$. The π is found in the microstrips but the K_s is found in the spectrometer so it has only direction information. Other examples of this case would be $K_sK_s\pi$ and $K\pi^0$. In these cases the combination of the D direction and the intercept information from the single microstrip track defines a *plane* that must contain the primary vertex, as opposed to the usual case where the D track defines a *line* that must contain the primary vertex.

For the one-prong case the algorithm searches for pairs of tracks that are consistent with forming a vertex in the plane defined by the daughters. Since all single tracks will intersect the plane, there is no discrimination power and we cannot allow one-track primaries. Once a pair of tracks that verticize in the plane is found, other tracks are clustered around this pair as long as the confidence level remains above 1%.

When these vertices are being fit, the information from the plane defined by the daughters is included in the fit with an additional χ^2 term:

$$\left(\frac{D}{\sigma_D}\right)^2, \qquad \text{where } D = (\vec{V} - \vec{P}) \cdot \vec{N} \tag{6.3}$$

and $\vec{V}$ is the vertex to be fit for, $\vec{P}$ points to a point in the plane, and $\vec{N}$ is the plane's normal. Since the error on D is strongly dependent on the distance from the daughter measured in the microstrips to the primary vertex, we found that a center of the target approximation is insufficient for calculating the error on D so we use the position of the most upstream VERTIC vertex.

To find ℓ/σ we cannot use the separation of the primary and secondary since there is no secondary vertex position found. We use a fit that is based on the D direction and the transverse distance between the microstrip track and the primary vertex.

6.4.2 Force and Exclusion Lists

The routines have a capability to force anything in the primary vertex. This could be used to force two D's to be in the primary vertex to find a sample of events with two reconstructed D's. This could also be used to force the soft pion from a D^{*+} decay in the primary. This particular trick is not effective because the standard algorithm is already very efficient so forcing the soft pion candidate into the primary only serves to bring in more background.

SDVERT also has the capability to exclude anything from being considered for the primary vertex. Doubly linked microstrip tracks (which are mostly e^+e^- pairs) are excluded by default. Some possible uses of this feature are to exclude high momentum tracks from the primary or tracks identified as kaons. This would be to try to remove the recoil charm from the primary.

6.4.3 Decay Chains

SDVERT has the capability of creating decay chains. An example of this would be the decay $B \to Dn\pi$, $D \to Kn\pi$. The analysis would search for the D,

create the D track, then combine it with pions to form a B track which is then used to seed the search for the primary vertex. There is no limit to the length of the decay chain because once a set of tracks are combined into a single track, that new track is equivalent to any other track.

6.4.4 π^0's, Kinks, and Ξ's

$\pi^0 \rightarrow 2\gamma$ are reconstructed in the electromagnetic calorimeters where the the energy and position of each γ is measured. This information, combined with the assumption that the π^0 comes from the target gives the π^0 momentum vector. There is no useful intercept information because of the target constraint and calorimeter resolution. The π^0 is treated like a K_s found in the magnet, the momentum vector and it's error is used to define the D direction but the π^0 cannot help determine the D vertex position.

A kink is a charged particle that decays into a charged and a neutral particle somewhere between the microstrips and P0, such as $\Sigma \rightarrow p\pi^0$. The Σ is found as a microstrip track so it's slopes and intercepts and their errors are straightforward to calculate. Because the π^0 is not reconstructed, there is usually a two-fold ambiguity in the Σ's momentum and each case is handled separately. To rigorously calculate the error on the Σ momentum would be difficult so the momentum for the Σ is put in the formula for the momentum error on a track.

Ξ's are found in the decay mode $\Lambda\pi$, if the decay is upstream of the microstrips, it is called a type 1, if the decay is downstream of the microstrips, it is called a type 2. For type 1's the algorithm is the same as the one prong case, $K_s\pi$ discussed above. Type 2 Ξ's leave a track in the microstrips so the slopes and intercepts are straightforward to calculate. The error on the momentum of the Ξ is found as the error on the momenta of the two daughters added in quadrature.

6.5 DVFREE

DVFREE is routine that can find a primary vertex in the case that there is no seed track from a charm candidate. This occurs for decays with ν's, such as

$K\pi\mu\nu$ or unreconstructed π^0's, such as $K\pi\pi^0$. Because the daughters are not all found, the D direction is not known so we can't create a seed track.

Typically, a set of tracks is found as a D candidate, these tracks are entered in the exclusion list then DVFREE is called. DVFREE returns a set of vertices formed from the rest of the tracks in the event and a primary vertex is chosen, usually as the most-upstream vertex or the highest multiplicity vertex.

The DVFREE algorithm begins with finding any pair of tracks that form a vertex with a confidence level greater than 1%. It then adds as many tracks as possible to that vertex as long as the confidence level remains above 1%. The tracks are not searched or included in any particular order.

The routine then chooses a track that is not in the first vertex and attempts to cluster other tracks around it. When it is looking for these additional tracks, it considers tracks that might already be in a vertex. This way a track may be in any number of vertices. The process of choosing a track that is not in a vertex and clustering around it is repeated until all tracks are in every vertex they are consistent with or in no vertex at all.

Figure 6.9 compares the performance of DVFREE to the standard algorithm using the seed track for $K2\pi$, $K\pi$, and $K3\pi$. The plots show the yield plotted against the signal to noise for several ℓ/σ cuts. The three lines are for the standard algorithm, DVFREE, and DVFREE with the requirement that the D track points to the primary. It is clear that the DVFREE efficiency is very high and the signal to noise is comparable. For the $K\pi$ case, the signal to noise is actually improved.

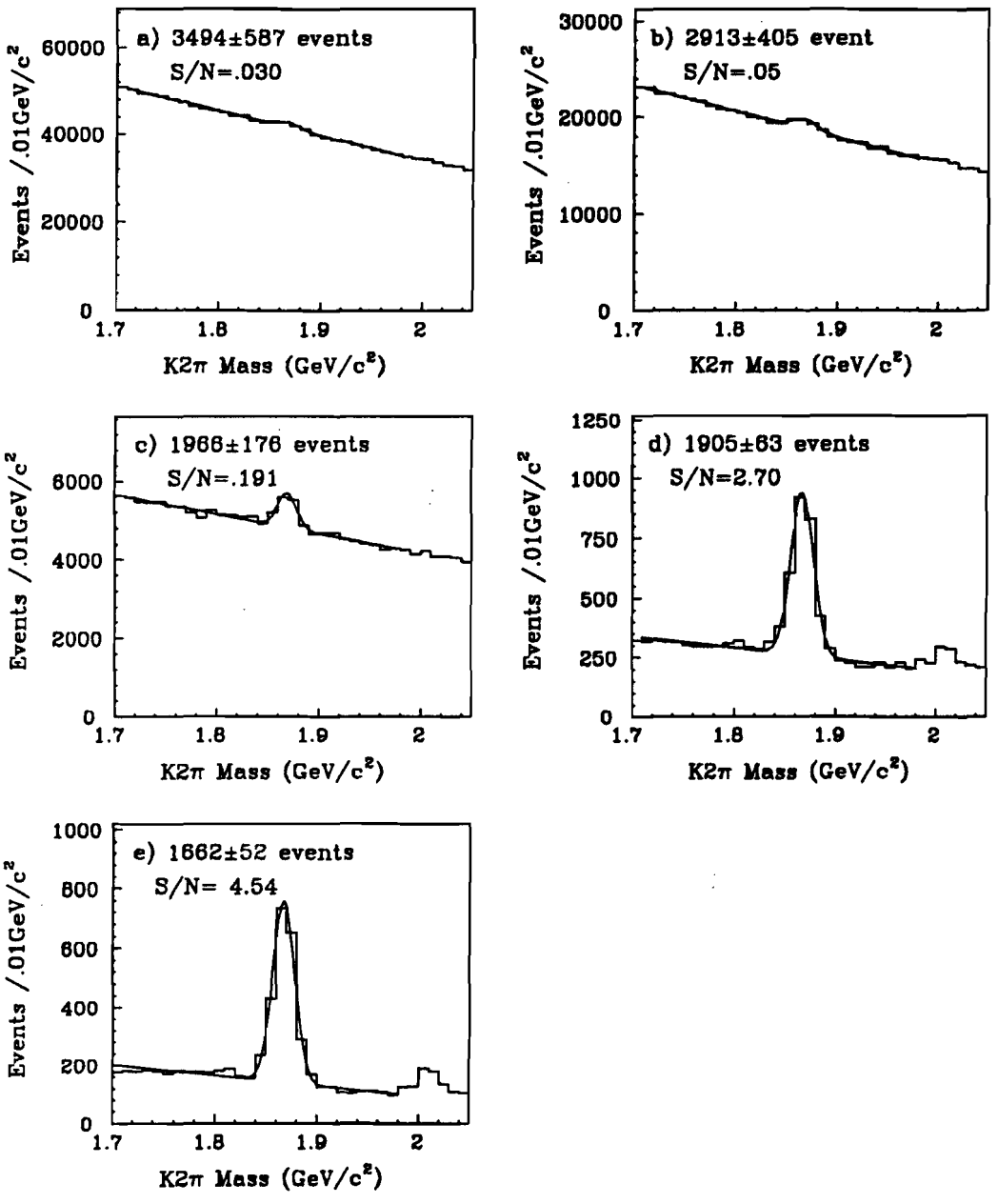

Figure 6.1. Invariant mass plots for a small sample of $K2\pi$ candidates with the requirements: a) none, b) DCL> .01, c) $\ell/\sigma > 8$, d) both DCL> .01 and $\ell/\sigma > 8$, and e) all the previous cuts and CL2< .01.

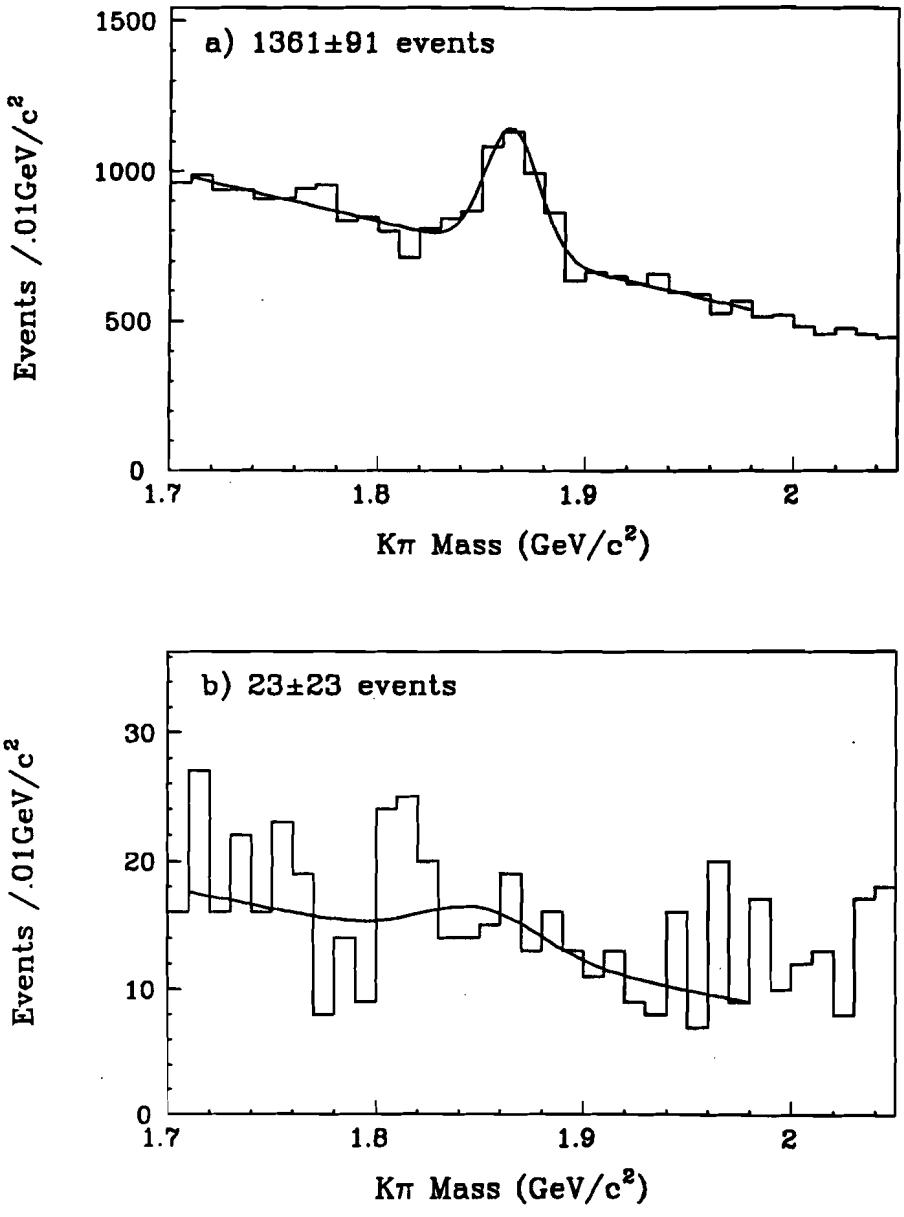

Figure 6.2. Invariant mass plots for a small sample of $D^{*+} \rightarrow (K\pi)\pi$ candidates that a) have a primary vertex found by the SDVERT algorithm, b) do not have a primary vertex found by the SDVERT algorithm.

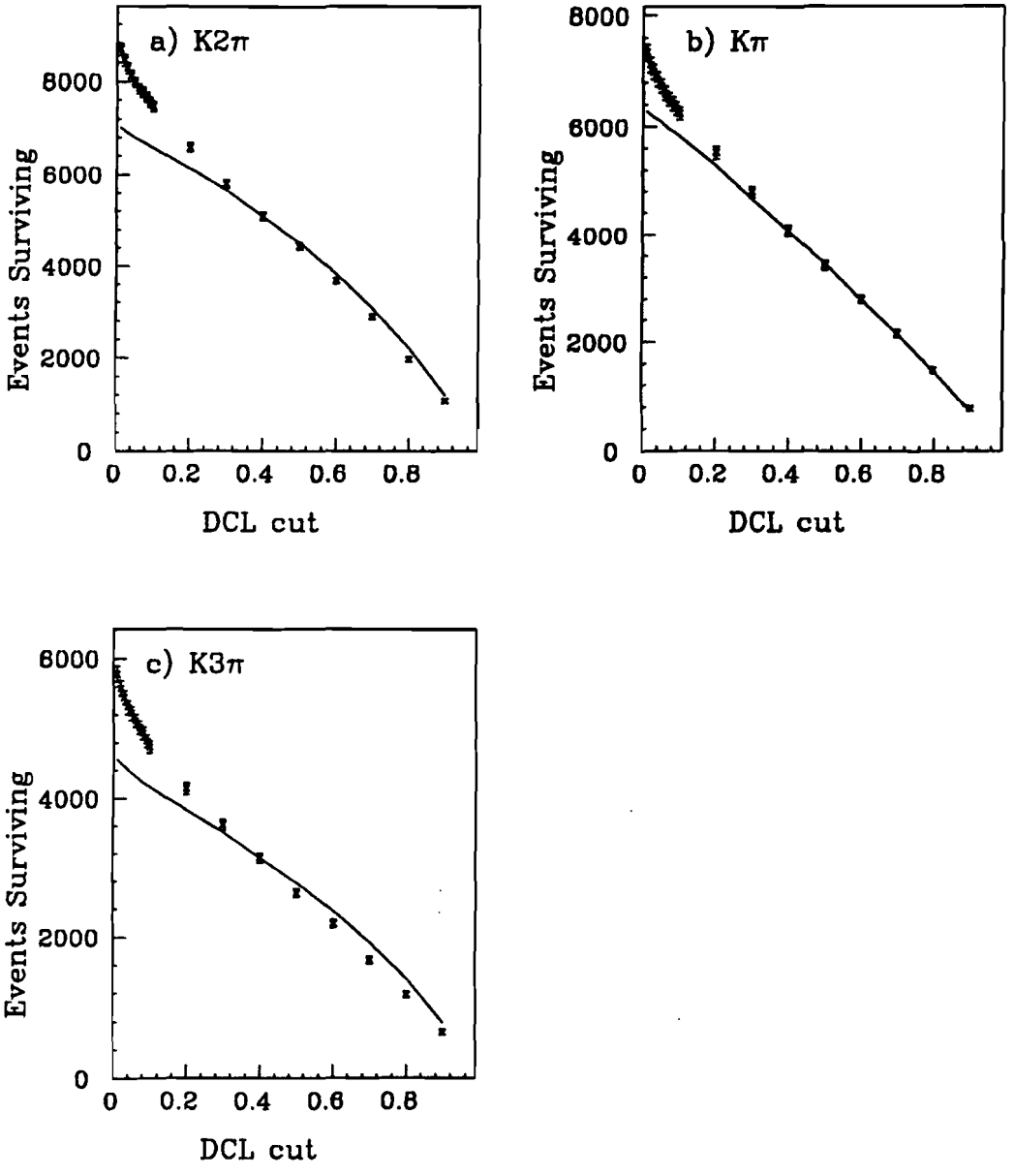

Figure 6.3. The survival of golden mode signals *vs* the DCL cut for a) $K2\pi$, b) $K\pi$, and c) $K3\pi$. The data is shown as the points with the error bars and the Monte Carlo prediction is shown as the solid line.

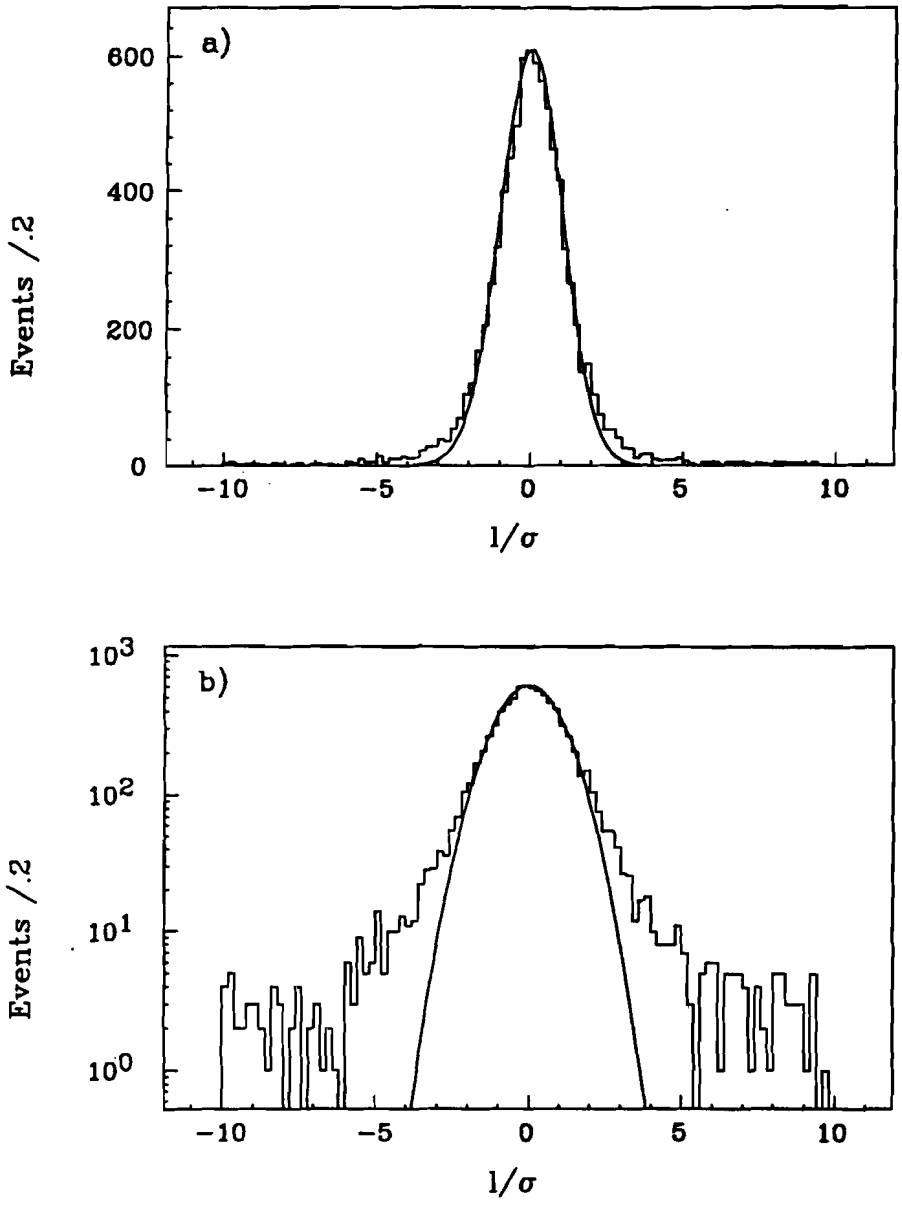

Figure 6.4. The distribution of ℓ/σ for background events where we expect $\ell = 0$ and ℓ/σ to be a unit Gaussian. The histogram is the data and the solid line is a Gaussian fit with width 1.01. a) is the distribution on a linear scale and b) is the distribution on a log scale.

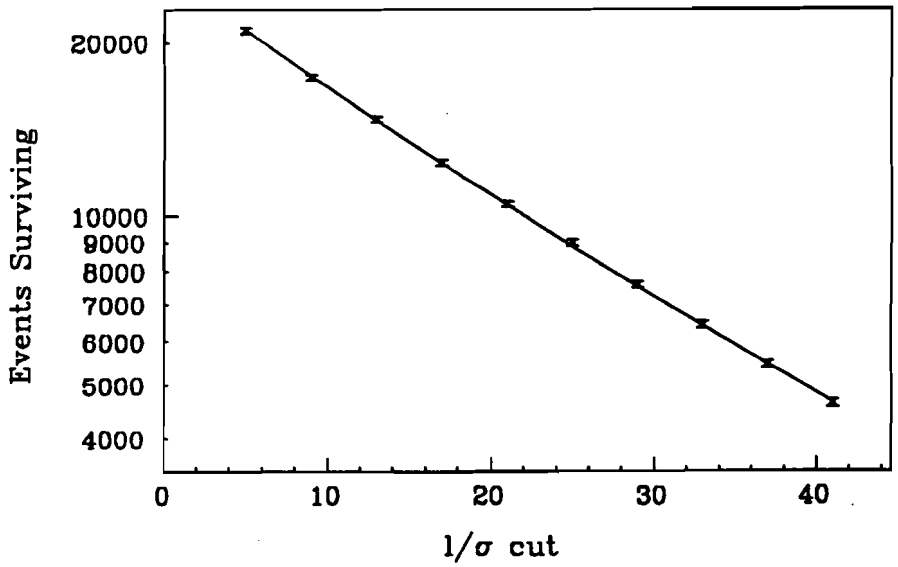

Figure 6.5. The survival of the $K2\pi$ signal *vs* the ℓ/σ cut. The data is shown as the points with the error bars and the Monte Carlo prediction is shown as the solid line.

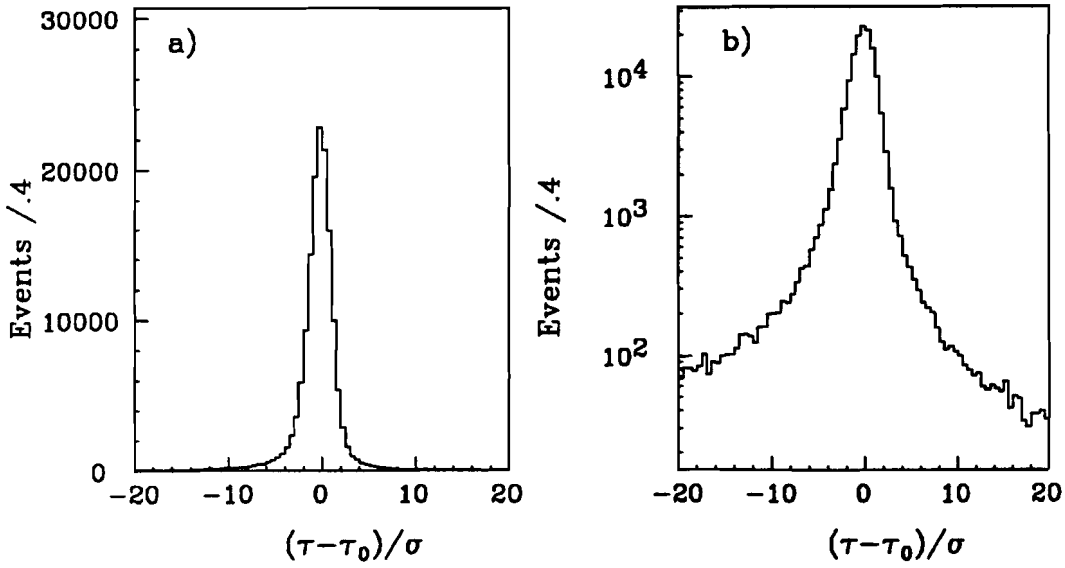

Figure 6.6. The distribution of the measured proper time minus the true proper time divided by the expected error for a $K2\pi$ Monte Carlo. a) is a linear scale, b) is the same distribution on a log scale. Note the negative bias in this distribution which indicates an average downstream pull of the primary vertex due to the inclusion of tracks from the recoil charm.

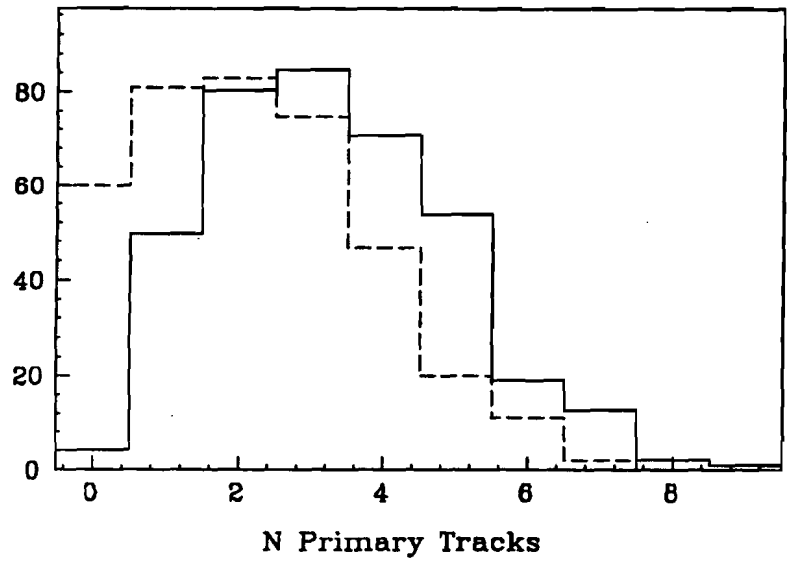

Figure 6.7. The distribution of the number of linked tracks found in the primary vertex by the SDVERT algorithm for the case: no restrictions (solid), and the recoil charm decay daughter tracks removed (dashed).

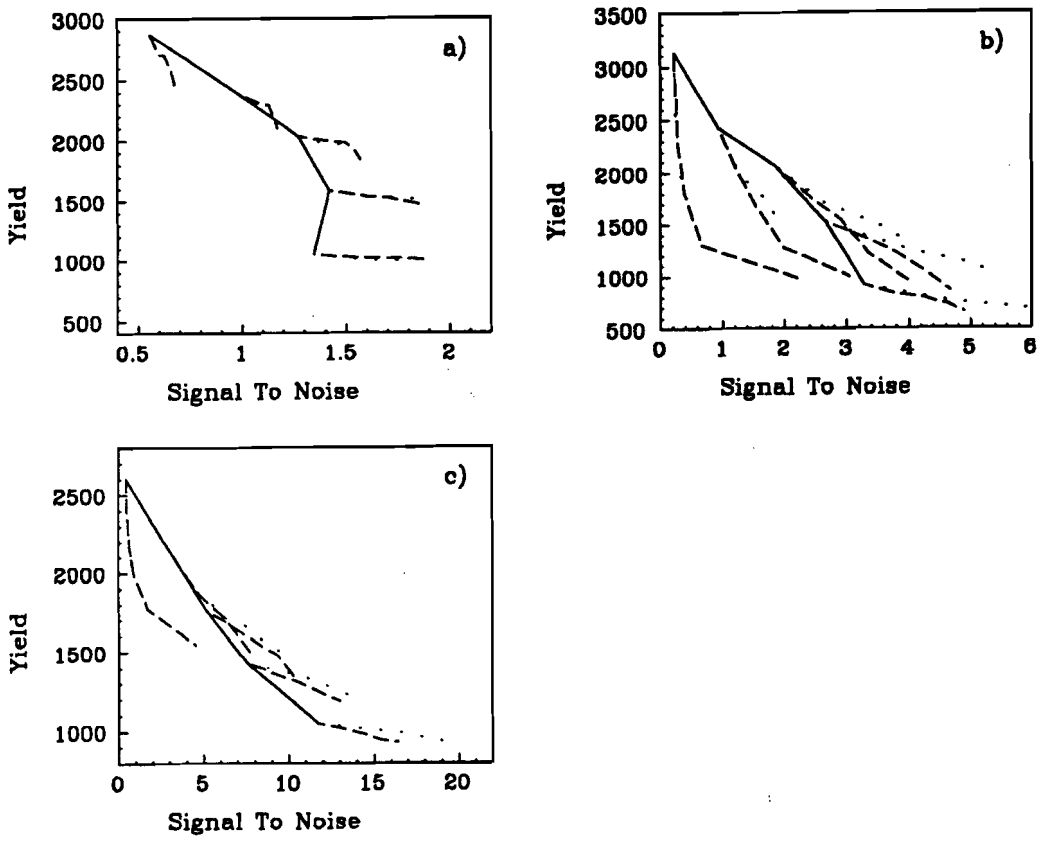

Figure 6.8. The effectiveness of isolation cuts CL1 and CL2 for a) $K\pi$, b) $K3\pi$, and c) $K2\pi$. Each plot contains a solid line which indicates the effect of cutting only on ℓ/σ, as the cut gets harder, the line moves to lower yield and higher signal to noise. At selected ℓ/σ cuts (labeled on the figure) we then make harder and harder isolation cuts. The effect of the CL1 cut is traced out by the dashed line, the effect of the CL2 cut is traced out by the dotted line. Effectiveness can be judged by comparing the yields of events with various isolation cuts at the same signal to noise.

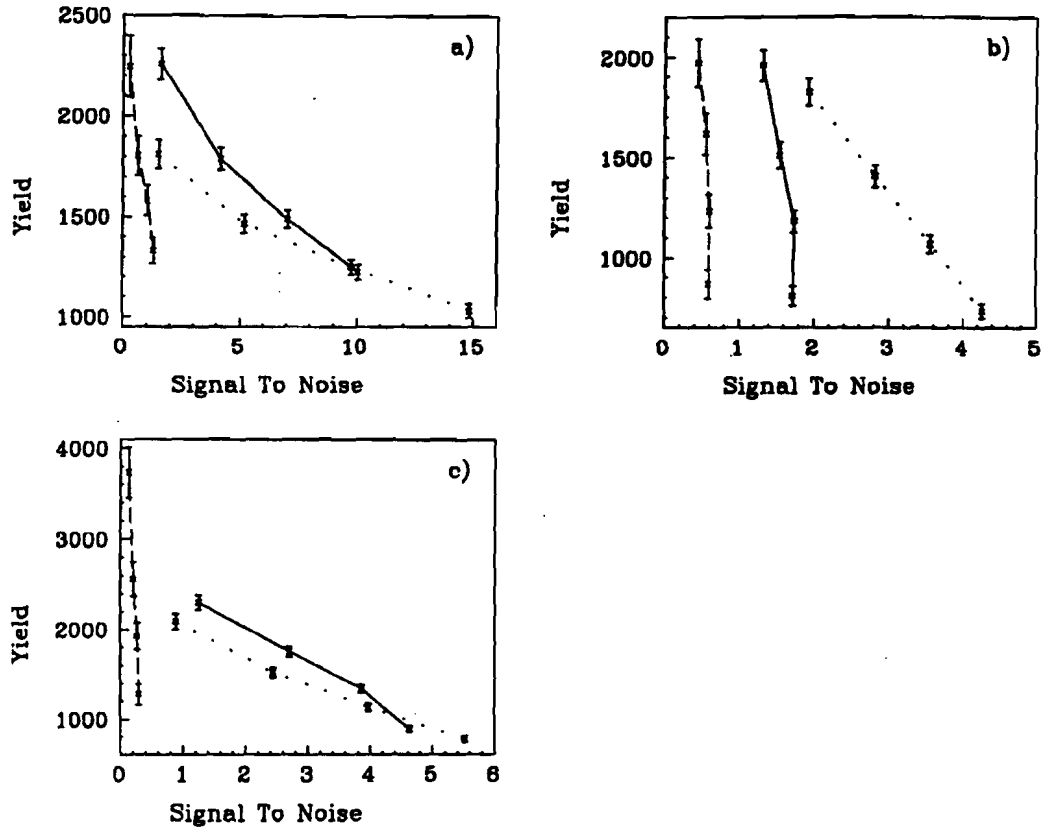

Figure 6.9. The comparison of yields and signal to noise ratios for a) $K2\pi$, b) $K\pi$, and c) $K3\pi$. Each plot contains a solid line which indicated the effect of cutting only on ℓ/σ from the standard algorithm. As the cut gets harder, the line moves to lower yield and higher signal to noise. The effect of cutting on ℓ/σ from DVFREE is traced out by the dashed line, the effect of adding the pointback requirement to the DVFREE result is traced out by the dotted line.

Chapter 7

$D^+ \to \overline{K}^{*0}\mu^+\nu$

In this chapter we analyze the decay $D^+ \to (K\pi)\mu\nu$ with the $K\pi$ forming a $\overline{K}^{*0}(892)$. We will show that the $K\pi$ spectrum is dominated by the $\overline{K}^{*0}$ and address the level of nonresonant decays and possible backgrounds.

We will first address the cuts used to extract a signal. The basic analysis is to find detached $K\pi\mu$ vertices, plot the $K\pi$ mass, and use the area under the $\overline{K}^{*0}$ peak as an estimate of the signal. Because we do not detect the neutrino, we are not fully reconstructing the decay, so we will present tests that the signal is the decay mode we are looking for. To further distinguish the signal from backgrounds, we will present a fit for the signal using all the available kinematic information.

After establishing the signal, we will present the branching ratio $\Gamma(D^+ \to \overline{K}^{*0}\mu^+\nu)/\Gamma(D^+ \to K^-\pi^+\pi^+)$ Finally, we will present a fit for the form factors governing the decay (see Chapter 2).

7.1 $D^+ \to \overline{K}^{*0}\mu^+\nu$ Signal

We use the global vertex skim to search for the signal (see section 4.3.3). This skim should be very efficient since it requires a mildly detached two-track vertex and the signal we are looking for has highly detached three-track vertex.

In this analysis, all tracks are searched for correct sign, mass, lepton and Cherenkov identification combinations to form $K\pi\mu$ candidates. All daughter tracks must be found in both the microstrips and the PWC system. The muon is identified in the inner muon detector. The kaon must be identified by the Cherenkov system as kaon definite or kaon-proton ambiguous and the pion and muon must not be identified as either a kaon or proton.

We require the $K\pi\mu$ combination to form a good vertex with a confidence level greater than 10%, thus greatly reducing the background from events where the K, π, and μ do not come from the same vertex.

The muon system is shielded by many radiation lengths of material. This causes some difficulty in matching muon system hits to low momentum tracks because of the large multiple scattering. To avoid this region of confusion, we require the muon to have a momentum greater than 10 GeV/c. The $K\pi\mu$ combination must have a momentum greater than 50 GeV/c.

Background from $D^+ \rightarrow K2\pi$, where a pion is misidentified as a muon, is eliminated by requiring that the reconstructed $K\pi\mu$ mass be less than 1.8GeV/c^2.

We find the primary vertex by searching for the most upstream high-quality vertex in the target region that can be made from the tracks which remain after the $K\pi\mu$ combination is removed. This is the DVFREE algorithm explained in section 6.5 where we show that the algorithm is highly efficient.

In order to suppress that large level of non-charm background, we exploit the long lifetime of the D^+ by requiring the candidate to be well detached from the primary vertex. For the major results discussed here, we require the separation divided by its error, ℓ/σ is greater than 20 (about one D^+ lifetime).

We require that the $K\pi\mu$ vertex be isolated from other tracks in the event (not including tracks in the primary vertex) by requiring that the maximum confidence level for another track to form a vertex with the candidate be less than 1%. This cut removes any possible background from higher multiplicity decays. It also removes background from events where a hadron has reinteracted in the target to fake a detached vertex. These interactions, being hadron-nucleon, are expected to be larger multiplicity.

The quark constituents of the D^+ are the c and $\bar{d}$. In the spectator decay (Figure 2.1) the c quark decays to an s quark and a W^+ which decays to $\mu^+\nu$. The s and the spectator $\bar{d}$ form the $\overline{K}^{*0}$ which decays to $K^-\pi^+$. This decay chain gives the charge correlation $Q_\mu \neq Q_K$. Real charm decays will produce an excess of right-sign events over wrong-sign. We will subtract the wrong-sign sample from our right-sign data distributions.

In the next section we will discuss the vertexing cuts in more detail.

7.1.1 Signal Cut Response

Figure 7.1 shows the wrong-sign subtracted signals for several ℓ/σ cuts. Note that the low mass bump from the decay $D^{*+} \rightarrow (K^-\mu^+\nu)\pi^+$ disappears with larger detachment cuts due to the shorter D^0 lifetime. We can identify this reflection by its distinctive $K\pi$ mass spectrum as computed with a Monte Carlo. Figure 7.2a shows the signal's survival *vs* the ℓ/σ cut compared to the survival predicted by our D^+ Monte Carlo. The very good agreement at longer detachments indicates little contamination from shorter lived charm states beyond $\ell/\sigma > 5$.

Figure 7.2b shows the signal survival as a function of the minimal confidence level requirement for the secondary vertex compared to that predicted by our Monte Carlo. The accumulation of events at low secondary vertex confidence level in the data suggests there is some contamination from charm backgrounds where the $K\pi\mu$ tracks do not originate from a common vertex. Most of this background is eliminated by the requirement that the secondary vertex confidence level exceeds 10%.

Figure 7.2c compares the data and Monte Carlo response to the secondary vertex isolation cut. Here the vertex is more isolated as the confidence level cut gets smaller. Agreement is good indicating negligible potential background from charm states with an additional charged track in the same vertex as the $K\pi\mu$ candidate. We require this confidence level to be less than 1%.

7.2 Limits on $D^+ \rightarrow (K^-\pi^+)\pi^0\mu^+\nu$ and $D^+ \rightarrow K^-\pi^+\mu^+\nu$

The decay modes may appear appear as right sign excess in the $(K\pi)\mu\nu$ sample are:

Table 7.1. $K\pi\mu$ Backgrounds

number	mode	fit parameter
1	$(K\pi)\mu\nu$ (signal)	$1 - f_1 - f_2 - f_3$
2	$K\pi\mu\nu$ (nonresonant)	f_1
3	$D^{*+} \rightarrow (K\mu\nu)\pi$	f_2
4	$(K\pi)\pi^0\mu\nu$	$f_3/2$
5	$(K\pi^0)\pi\mu\nu$	$f_3/2$

We make the standard assumption [17] that the last two final states are produced through the decay of a hypothetical isospin 1/2 resonance into a $K^*\pi$ final state. Under this assumption the yields of process 4 and 5 are the same as shown in the following table of the relevant branching ratios deduced by isospin symmetry (Clebsch-Gordon decompositions)

Table 7.2. Clebsch-Gordan Coefficients

number	mode	coefficient
1	$BR(K^{*0} \rightarrow K^-\pi^+)$	2/3
2	$BR(K^{*0} \rightarrow K^0\pi^0)$	1/3
3	$BR(K^{*-} \rightarrow K^-\pi^0)$	1/3
4	$BR(K^{*-} \rightarrow K^0\pi^-)$	2/3
5	$BR((1/2,1/2)^0 \rightarrow K^{*0}\pi^0)$	1/3
6	$BR((1/2,1/2)^0 \rightarrow K^{*-}\pi^+)$	2/3
7	$BR((1/2,-1/2)^- \rightarrow K^{*-}\pi^0)$	1/3
8	$BR((1/2,-1/2)^- \rightarrow K^{*0}\pi^-)$	2/3

The yield of the fourth decay mode is the product of the fifth entry in Table 7.2 and the first entry which gives 2/9. The yield of the fifth decay mode is the product of the sixth entry and the third entry which is also 2/9.

We fit the two dimensional distribution of the $K\pi$ mass and the $K\pi\mu$ mass. For the fitting function we use the Monte Carlo distributions of these variables and for the $(K\pi)\mu\nu$ mode we include the effects of the matrix element which are significant. All modes are generated according to phase space except where the $K^*(892)$ is indicated. We constrain the total number of events in the fit, and the the yields of the last two modes are constrained to be the same so we are left with 3 fit parameters which are the fraction of events in the decay mode.

The fit is binned maximum likelihood. There are 23 bins in the $K\pi$ mass and 6 bins in $K\pi\mu$ mass. The fit prediction is the Monte Carlo distributions scaled by the fit parameters plus the wrong-sign distribution. The binning is displayed in Figure 7.3 which shows the projections of the distributions and the fit results. The fit results are summarized in Table 7.3.

Table 7.3. Nonresonant Fit Results

mode	fit parameter	result
$(K\pi)\mu\nu$ (signal)	$1 - f_1 - f_2 - f_3$	$.884 \pm .031$
$K\pi\mu\nu$ (nonresonant)	f_1	$.073 \pm .026$
$D^{*+} \to (K\mu\nu)\pi$	f_2	$.043 \pm .012$
$(K\pi)\pi^0\mu\nu + (K\pi^0)\pi\mu\nu$	f_3	$0 \pm .018$

Since the efficiencies for resonant and nonresonant decays are the essentially same we obtain a measurement of the branching ratio:

$$\frac{\Gamma(D^+ \to K^-\pi^+\mu^+\nu(\text{nonresonant}))}{\Gamma(D^+ \to (K^-\pi^+)\mu^+\nu)} = .083 \pm .029$$

or a limit of $< .12$ at the 90% confidence level. The previous limit on this decay was $< .23$ [18].

To find the limit on f_3 we integrate the likelihood to the 90% point and find $f_3 < .059$. Since this is the limit on the last two decay modes, the limit on each

mode individually is $< .029$. Our Monte Carlo finds that the modes with an additional π^0 have an efficiency that is 70% of the $(K\pi)\mu\nu$ efficiency so the limit is corrected by this factor and we obtain:

$$\frac{\Gamma(D^+ \to (K^-\pi^+)\pi^0\mu^+\nu)}{\Gamma(D^+ \to (K^-\pi^+)\mu^+\nu)} < .042$$

or correcting by the K^* branching ratios from Table 7.2 (a factor of 9/4) we obtain:

$$\frac{\Gamma(D^+ \to (K^*\pi)^0\mu^+\nu)}{\Gamma(D^+ \to (K^-\pi^+)\mu^+\nu)} < .095$$

The previous limit on this decay was $< .87$ [17].

7.3 $\Gamma(D^+ \to \overline{K}^{*0}\mu^+\nu)/\Gamma(D^+ \to K^-\pi^+\pi^+)$

We are only using the 1988 and 1990 samples for this branching ratio because the increased noise in the 1991 muon system (see 3.5.2) would introduce a systematic error which is comparable to the statistical error in this high-statistics analysis.

We find the $K2\pi$ signal with the same vertexing scheme and the same cuts (except for the muon cuts). The resulting signal is show in Figure 7.4. Background from $\overline{K}^{*0}\pi^+\pi^0$ where the pion is misidentified as a muon is corrected for by assuming a 1.3% misidentification probability which we measure with high statistics charm decays.

Possible contamination from $\overline{K}^{*0}\pi^0\mu\nu$ is included as a systematic error. We also consider the effect of changing the K^* lineshape based on uncertainty in the form factors. Since the muon does not strongly interact, we include as a systematic error due to the possible loss in efficiency from elastic nuclear scattering of the extra π in $K2\pi$. Since the muon does not leave as much energy in the HC for the trigger, we include a systematic based on varying the HC trigger response by 20%. We add these contributions in quadrature.

Table 7.4. Branching Ratio Systematics Summary

source	% error
line shape	5
scattering	5
ℓ/σ variation	6
HC	3
total	10

The result is $\Gamma(D^+ \to \overline{K}^{*0}\mu^+\nu)/\Gamma(D^+ \to K^-\pi^+\pi^+) = .56 \pm .04 \pm .06$. This ratio includes a correction factor for the undetected decay $\overline{K}^{*0} \to \overline{K}^0\pi^0$. The current world average (measured using the equivalent electron decay mode) is $.51 \pm .05$ [19].

7.4 Form Factors

In this section we will fit for the form factors that govern the decay $D^+ \to (K\pi)\mu\nu$. We will first discuss the how the kinematics are reconstructed, then discuss the fit itself, Monte Carlo studies, and finally systematics and results.

The form of the matrix element is described in Chapter 2. There are four kinematic variables, $\cos\theta_v$, $\cos\theta_\mu$, $t = M(\mu\nu)$, and χ. We will use the distributions of the first three variables as the measured distributions in the fit. We ignore χ as justified below in section 7.4.4. $\cos\theta_v$ is the angle between the π and the D direction in the $\overline{K}^{*0}$ rest frame, $\cos\theta_\mu$ is the angle between the ν and the D direction in the $\mu\nu$ rest frame. D^- decays have the same definition of variables and no change is required in the matrix element (see Chapter 2).

As explained in Chapter 2, in the absence of lepton mass effects, there are two axial and one vector form factor, $A_1(t)$, $A_2(t)$, and $V(t)$. We assume these form factors have a simple pole dependence with masses $M_A = 2.5$ GeV and $M_V = 2.1$ GeV, and fit for the ratio of the form factors evaluated at $t = 0$: $R_v = V(0)/A_1(0)$ and $R_2 = A_2(0)/A_1(0)$.

We now discuss specifics of how the kinematic variables are calculated in the following two sections on unphysical decays and reconstructing the kinematic variables.

7.4.1 Unphysical Decays

Due to resolution and pattern recognition (determining which particles belong) of the primary vertex, we sometimes reconstruct a $D^+ \rightarrow K\pi\mu\nu$ decay such that the kinematics of the decay are unphysical. With the D^+ direction and the total momentum vector of the charged ($K\pi\mu$) particles, $\vec{p}_c$, we can test if the decay is physically allowed. First we find the component of $\vec{p}_c$ that is perpendicular to the D^+ direction, $p_{\perp c}$. If we then boost into the D^+ rest frame, this component does not change $p^*_{\perp c} = p_{\perp c}$. The charged transverse momentum is balanced by $p_{\perp \nu}$ and $p^*_{\perp \nu} \leq E^*_\nu$ where $E^*_\nu = (M_D^2 - M_c^2)/2M_D$. If the decay is physical we find $p^*_{\perp c} = p^*_{\perp \nu} \leq E^*_\nu$ while if the the reconstruction of the decay is unphysical we find $p^*_{\perp c} > E^*_\nu$.

Figure 7.5 is a histogram of $E^*_\nu - p^*_{\perp c}$. About 50% of the events have this variable greater than zero, indicating an unphysical reconstruction. Overplotted is the Monte Carlo prediction which shows good agreement.

Another way to picture the decay is that $p_{\perp c}$ defines a cone for allowed positions of the primary vertex with the apex at the D^+ vertex and spreading out towards the primary vertex. If the reconstruction of the decay is physical, the primary will be in this cone, otherwise it will be outside this cone. To recover unphysical decays, we move the primary vertex position to the nearest allowed position on this cone and recompute the kinematic variables. Figure 7.6 compares the resolution in the cosines for events that were originally reconstructed as physical and for all decays. There is very little difference in these resolutions so we will include these events in the analysis. We also found very little improvement in the signal to noise by requiring that the decay was originally reconstructed as physical so we make no requirement on this condition.

7.4.2 Reconstructing the Kinematic Variables

The fit for the form factors is a fit to the kinematic variables describing the decay (see Chapter 2). These are $\cos\theta_v$, the angle between the π and the D direction in the $\overline{K}^{*0}$ rest frame, $\cos\theta_\mu$, the angle between the ν and the D direction in the $\mu\nu$ rest frame, and t, the square of the $\mu\nu$ mass. D^- decays have the same definition of variables.

We start by checking that the decay is physical, and if it is not, then recover it. The charged tracks are measured in the spectrometer so we have their four-vectors. We assume the D^+ momentum vector points along the direction between the primary and secondary vertices, we fix the D^+ mass to be 1.8693 GeV/c^2, and we fix the ν mass to be zero.

We start with the four vector equation: $\vec{\mathbf{p}}_D = \vec{\mathbf{p}}_c + \vec{\mathbf{p}}_\nu$. Squaring this we have

$$E_D E_c = |\vec{p}_D||\vec{p}_c|\cos\theta_{Dc} + M^2 \tag{7.1}$$

where $M^2 = (M_D^2 + M_c^2)/2$ and $\cos\theta_{Dc}$ is the cosine of the angle between the charged track momentum and the D^+ direction. Putting $E_D = \sqrt{p_D^2 + M_D^2}$ and squaring again we get:

$$(E_c^2 - p_c^2\cos\theta_{Dc})\,p_D^2 \;-\; 2p_c M^2\cos\theta_{Dc}\,p_D \;+\; M^4 + M_D^2 E_c^2 \;=\; 0 \tag{7.2}$$

which is a quadratic equation for p_D. We chose the lower $|\vec{p}_D|$ solution. Since we have the D direction and magnitude, we have the D four-vector and with that we can find the neutrino four-vector and proceed find the kinematic variables.

To justify the choice of the lower momentum solution, we histogram the reconstructed cosines minus the true value for both solutions in Figure 7.7 and find no significant difference. The lower momentum solution has a marginally better resolution in the kinematic variables so we choose that solution.

7.4.3 The Fit

The fit is binned maximum likelihood with three equal bins in $\cos\theta_v$, three in $\cos\theta_\mu$, and two in t/t_{max}. Because the matrix element tends to produce relatively broad structures in the kinematic variables, we can use a rather coarse binning to extract the form factors without much loss in statistical power. This allows us to use moderate size Monte Carlo samples, facilitates our ability to compare the fit to the data, and tends to minimize the effects of resolution. We also can avoid hot spot regions where the decay intensity is nearly zero and we would be sensitive to each background event. The bins are displayed in Figure 7.8.

To justify this binning further we can linearize the fit and use matrix algebra to predict the loss of statistical power. The information can be summarized by the matrix equation $t^* = \rho X$. where t^* is a vector containing the form factors, and X is a vector containing the bin populations. In this linearized picture, ρ is essentially a weight for each bin and the fit parameters are weighted averages of the bin populations. Figure 7.9 shows the elements of the ρ matrix. Since Γ_l/Γ_t is a combination of the form factors, an equivalent set of ρ matrix elements can be calculated for this ratio from the derivatives of the decay intensity with respect to the form factors. These are also shown in Figure 7.9. The underlying workings of the fit can be seen in these figures. For example, a positive polarization ratio should be revealed in a positive curvature in $\cos_v$ which can be seen in the Γ_l/Γ_t ρ matrix elements *i.e.* the central $\cos\theta_v$ bins are weighted more negatively than the outer $\cos\theta_v$ bins. The ρ matrix gives expected errors in terms of the the autocorrelation of the fit parameters ($< \delta t \delta t^t >$) which depends on the ρ matrix and the poisson fluctuations of the bin yield, $< \delta t \delta t^t >= \rho^t < \delta x \delta x^t > \rho$. This allows us to assess the statistical power of various binning schemes, summarized in Table 7.4. The 18 bins we use are the smallest number of bins that gives a negligible loss in statistical power ($\approx$21%). This is easy to understand. The three bins in $\cos\theta_v$ and $\cos\theta_\mu$ gives us the ability to measure separate curvature and asymmetries in those variables. The two bins in $y = t/t_{max}$ allows one to follow their t evolution to get additional statistical power.

Table 7.4. Anticipated Errors *vs* Binning Scheme

Case	N_v	N_μ	N_y	$\sigma(R_v)\sqrt{N}$	$\sigma(R_2)\sqrt{N}$	Corr	$\sigma(\Gamma_\ell/\Gamma_t)\sqrt{N}$
0	∞	∞	∞	6.56	4.18	-.33	2.86
1	10	10	10	6.66	4.34	-.34	2.96
2	5	5	3	7.10	4.56	-.35	3.09
3	3	3	2	7.93	5.00	-.36	3.38
4	2	2	2	10.13	5.96	-.29	4.24
5	2	2	10	9.73	5.17	-.27	3.79
6	1	1	10	42.7	5.35	-.06	10.07
7	3	3	1	9.11	8.02	-.57	4.84
8	2	2	1	108	152	-.996	83

In the fit, the prediction of the yield in each bin is the integral of the matrix element over the bin. This number is multiplied by a Monte Carlo correction factor which is the number of events reconstructed in the bin divided by the number generated in the bin with a trial set of form factors. The correction is largest at low $\cos\theta_\mu$ and low t, where the efficiency is approximately half the maximum efficiency. Because of finite bin size and resolution, the Monte Carlo correction depends on the form factors so we take the current fit results, recalculate the correction, and perform the fit again. We find that only two iterations are necessary.

To predict the background in a right-sign bin, we add the wrong-sign yield in the bin, scaled by a third fit parameter, the background level. This fit parameter allows background level fluctuations to be reflected in the form factor errors, and it is tied to the observed number of wrong-sign events through an additional Poisson factor in the likelihood.

This fit procedure eliminates any biases from events where the wrong solution is chosen, recovered unphysical events, and resolution. It has the advantage that

we are not required to invent a background parameterization.

The correction due to finite muon mass is done in two stages. The matrix element in the fit function includes an overall factor of $(1 - m_\mu^2/t)^2$. The (much smaller) additional finite mass terms are included in the Monte Carlo correction factors on successive iterations. We assume that the third form factor in the finite mass terms, R_3, is zero.

7.4.4 Mini-Monte Carlo Studies

A mini-Monte Carlo is a program that simulates data samples using approximations for the effects of spectrometer resolution. It is a stand-alone program apart from the full Monte Carlo simulation. This faster simulation of data sets allows us to generate and fit many data sets to test systematics of the fitting process.

To simulate a data set we generate decays according to phase space and reject on the matrix element. We then allow for resolution by drawing a momentum, lifetime, and primary and secondary vertices for the decay and require $\ell/\sigma > 20$. We give the primary vertex a transverse position error of 30μm as a rough estimate of the true total primary and secondary vertex resolution. We then solve for the decay the same way as it is done in the data including the effects of resolution and the quadratic ambiguity. Figure 7.10 shows the distribution of the difference between the reconstructed and true cosines for the mini-Monte Carlo and for the full Monte Carlo. The distributions are almost identical, indicating that we have functionally recreated almost all the resolution effects in the mini-Monte Carlo. We also generate background according to the projections of the wrong-sign data in the kinematic variables.

First, the mini-Monte Carlo is used to test the value of including the coplanarity, χ, in the fit. We find that including it cannot reduce the error on R_v and can reduce the error on R_2 by only 25%. This is a negligible gain for a measurement that has systematic error comparable to the statistical error.

By allowing the background level to vary in the fit, we allow for the uncertainty in the number of background events but this does not allow for the uncertainty due to using the finite wrong-sign sample as the parent population of the background in the fit. One way to think of this is that we allow for the uncertainty from the background level, but not from the background shape. The additional uncertainty from this source can be measured with the mini-Monte Carlo and is found to increase the reported uncertainty by 14%.

As explained in Chapter 2, the finite muon mass allows for a third form factor ratio, R_3 which assume is zero. To assess our sensitivity to this assumption, we fit for R_v and R_2 in mini-Monte Carlo samples generated with $R_3 = 0$ and $R_3 = 3$ and found the results varied by less than 7% of our statistical error.

Finally, the mini-Monte Carlo is used to test the general reliability of the errors reported by the fit. The fit cannot include in the reported errors the additional uncertainty due to the effect of events moving from one bin to another due to resolution. This effect can be seen in the limit of resolution so poor that all the measured distributions are flat so no measurement can be made and the uncertainties should approach infinity. We find that the errors are accurate, that this resolution-based source of error is negligible. Also we find there is no significant bias.

7.4.5 Systematics

If the muon system is uniformly inefficient, there will be no systematic effect in the form factors because they are determined from the shape of the distributions of the kinematic variables. However, if there is non-uniform inefficiency, there may be some distortion of the distributions. To compute this source of systematic error, we again linearize the fit and the information can be summarized by the matrix equation $t^* = \rho X$ where t^* is a vector containing the form factors, and X is a vector containing the bin populations. A nonuniform muon efficiency can be translated to a non-uniform efficiency in each of the bins in a Monte Carlo

then the systematic error can be found as $\delta t^* = \rho \delta X$ where δX represents the change in the bin populations due to the additional, non-uniform efficiency.

We conservatively estimate a possible non-uniform inefficiency as the difference between uniform efficiency and the efficiency as seen in the 1991 system which varied in the transverse dimension due to noise. This estimated systematic error is summarized in Table 7.5.

We can apply the same procedure to find the systematic due to the fact that the HC triggering threshold is uncertain. Here we take the change in the efficiency for each fit bin when the threshold is raised by $30\text{GeV}/c^2$ and again propagate the bias into the form factors.

The largest source of systematic error is found by scaling the background by 1.5 before subtracting it in the fit. The factor of 1.5 is the factor necessary to remove the non-K^* right-sign excess. Although we feel the excess is due to know charm decays, we have no knowledge of the matrix elements that these decays proceed by. Table 7.5 summarizes the sources of systematic error and shows the total, which is the contributions added in quadrature.

Table 7.5. Form Factor Systematics

	μ	HC	BG	total
R_v	.04	.09	.26	.28
R_2	.014	.06	.08	.10
Γ_l/Γ_t	.02	.07	.11	.13

7.4.6 Results

The fit results are [11] $R_v = 1.74 \pm .27 \pm .28$ and $R_2 = .78 \pm .18 \pm .10$ with a correlation of $-.15\%$. As described in Chapter 2, we calculate the polarization for for the electron decay, $\Gamma_l/\Gamma_t = 1.20 \pm .13 \pm .13$. The fit is displayed in Figure 7.11.

Table 7.6 compares this result to other recent measurements and Table 7.7 shows some theoretical predictions.

Table 7.6. Form Factor Ratio Comparisons

Exp	R_2	R_v	Γ_l/Γ_t
This result [11]	$.78 \pm .18 \pm .10$	$1.74 \pm .27 \pm .28$	$1.20 \pm .13 \pm .13$
E691 [7]	$0.0 \pm .5 \pm .2$	$2.0 \pm .6 \pm .3$	$1.8 \pm^{.6}_{.4} \pm .3$
E653 [8]	$.82 \pm^{.22}_{.23} \pm .11$	$2.00 \pm^{.34}_{.32} \pm .16$	$1.18 \pm .18 \pm .08$

Table 7.7. Form Factor Ratio Predictions

Authors	R_2	R_v	Γ_l/Γ_t
BSW [20]	1.31	1.44	.91
KS [10]	1.0	1.0	1.16
AW/GS[9]	.75	1.88	1.20
BBD [21]	$1.2 \pm .2$	$2.2 \pm .2$	$.86 \pm .11$
ELC [22]	$.01 \pm .7$	$1.63 \pm .27$	$1.84 \pm .63$
BES [23]	$.70 \pm .16 \pm^{.20}_{.15}$	$1.99 \pm .22 \pm^{.31}_{.35}$	$1.21 \pm .12 \pm^{.15}_{.13}$

As described in Chapter 2, we can calculate the values of the overall form factor, $A_1(0)$, from the form factor ratios given the branching ratio, $\Gamma(D^+ \to \overline{K}^{*0}\mu^+\nu)/\Gamma(D^+ \to K^-\pi^+\pi^+) = .56 \pm .04 \pm .06$ [11], the absolute branching ratio, $\Gamma(D^+ \to K^-\pi^+\pi^+)/\Gamma(D^+ \to \text{all}) = .08 \pm .0075$ [19], $\tau_{D^+} = 1.066 \pm .023$ps [19], and $|V_{cs}| = .975$ [19]. The results are summarized in Table 7.8 which compares our measurement to the only other recent measurement. Using our value for $A_1(0)$ and our values for the form factors ratios, and properly propagating errors, we can calculate $A_2(0)$ and $V(0)$ which are also in Table 7.8. Table 7.9 summarizes some theoretical predictions.

Table 7.8. Form Factor Comparison

Exp	$A_1(0)$	$A_2(0)$	$V(0)$
This result	$.56 \pm .04 \pm .03$	$.44 \pm .09 \pm .06$	$.98 \pm .19 \pm .18$
E691 [7]	$.46 \pm .05 \pm .05$	$0.0 \pm .2 \pm .1$	$.9 \pm .3 \pm .1$

Table 7.9. Form Factor Predictions

Authors	$A_1(0)$	$A_2(0)$	$V(0)$
BSW [20]	.88	1.15	1.27
KS [10]	.82	.82	.82
AW/GS[9]	.8	.6	1.5
BBD [21]	$.50 \pm .15$	$.60 \pm .15$	$1.10 \pm .25$
ELC [22]	$.52 \pm .07$	$.05 \pm .35$	$.85 \pm .08$
BES [23]	$.83 \pm .14 \pm .28$	$.59 \pm .14 \, ^{+.24}_{-.23}$	$1.43 \pm .45 \, ^{+.48}_{-.49}$

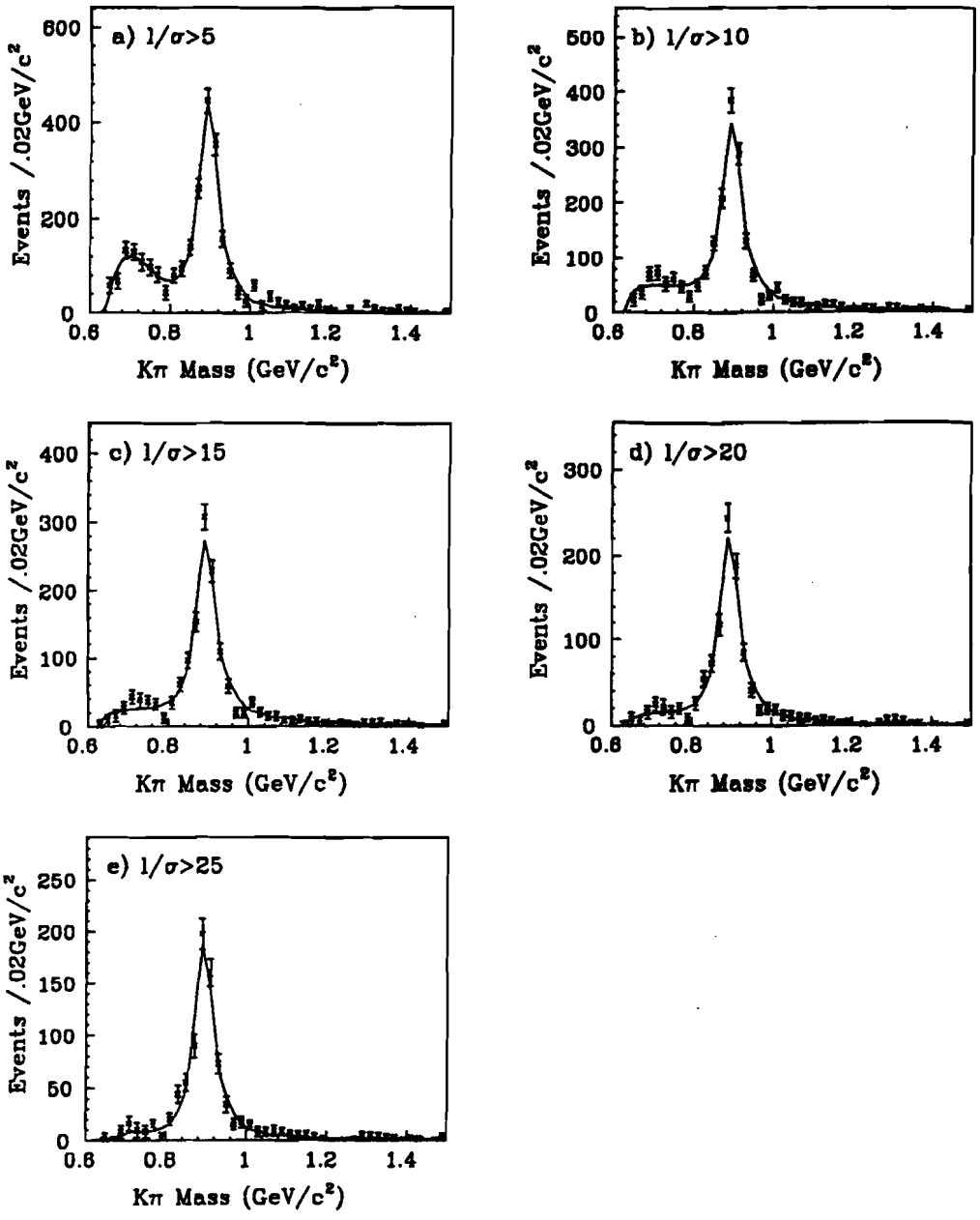

Figure 7.1. $D^+ \to \overline{K}^{*0}\mu^+\nu$ signal after wrong-sign subtraction for the indicated ℓ/σ cuts. The fit for the signal yield is the solid line. The fit uses a Monte Carlo prediction for the lineshape, based on our measurement of the form factors. The background term is of the form $a_1 x^{a_2} e^{-a_3 x}$ where a_i are the fit parameters and x is $M(K\pi) - (M(K) + M(\pi))$.

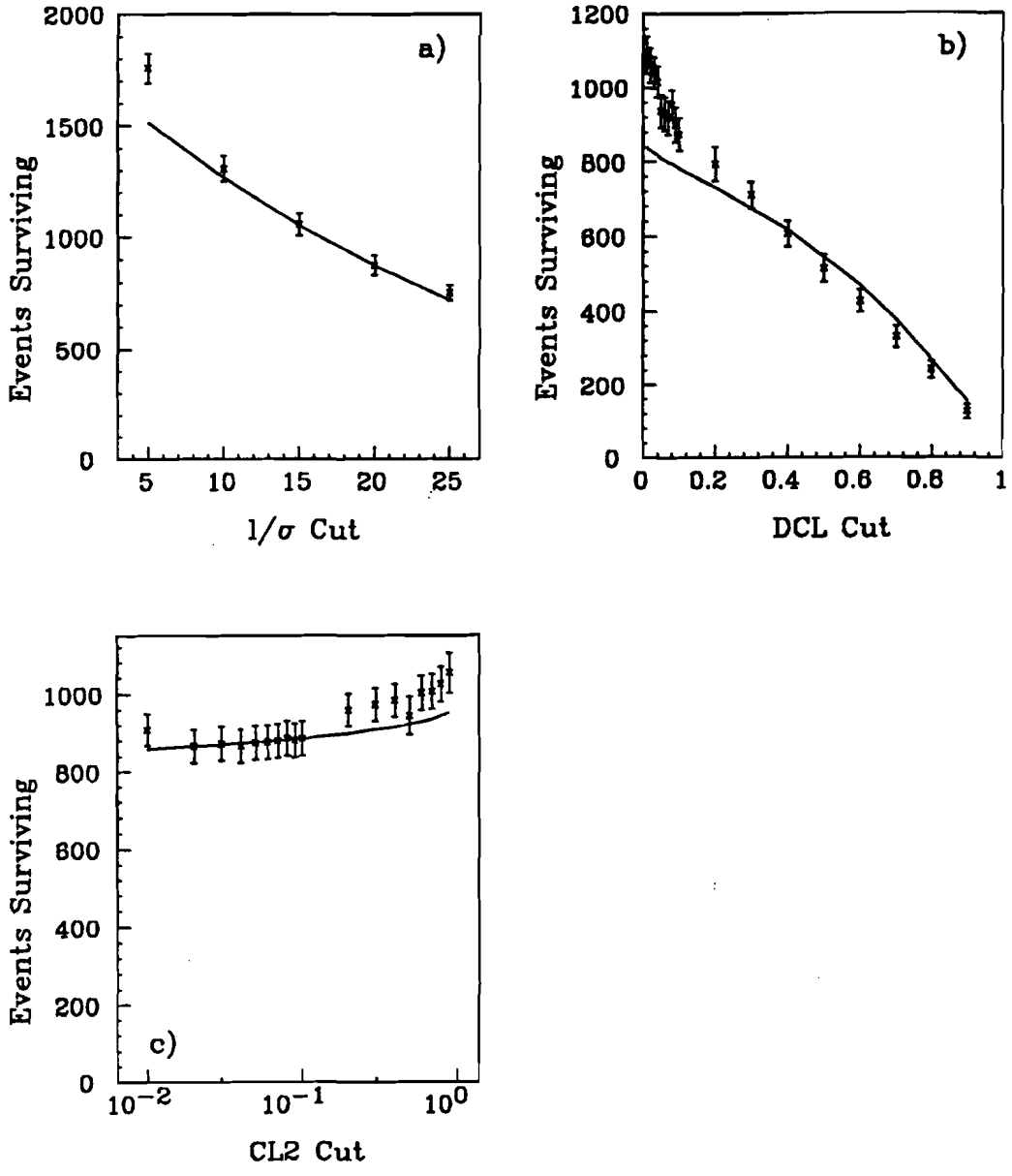

Figure 7.2. The $D^+ \to \overline{K}^{*0}\mu^+\nu$ signal survival plotted *vs* the cut for a) $\ell/\sigma >$ cut, b) DCL < cut, and c) CL2 < cut. The solid lines are the Monte Carlo prediction.

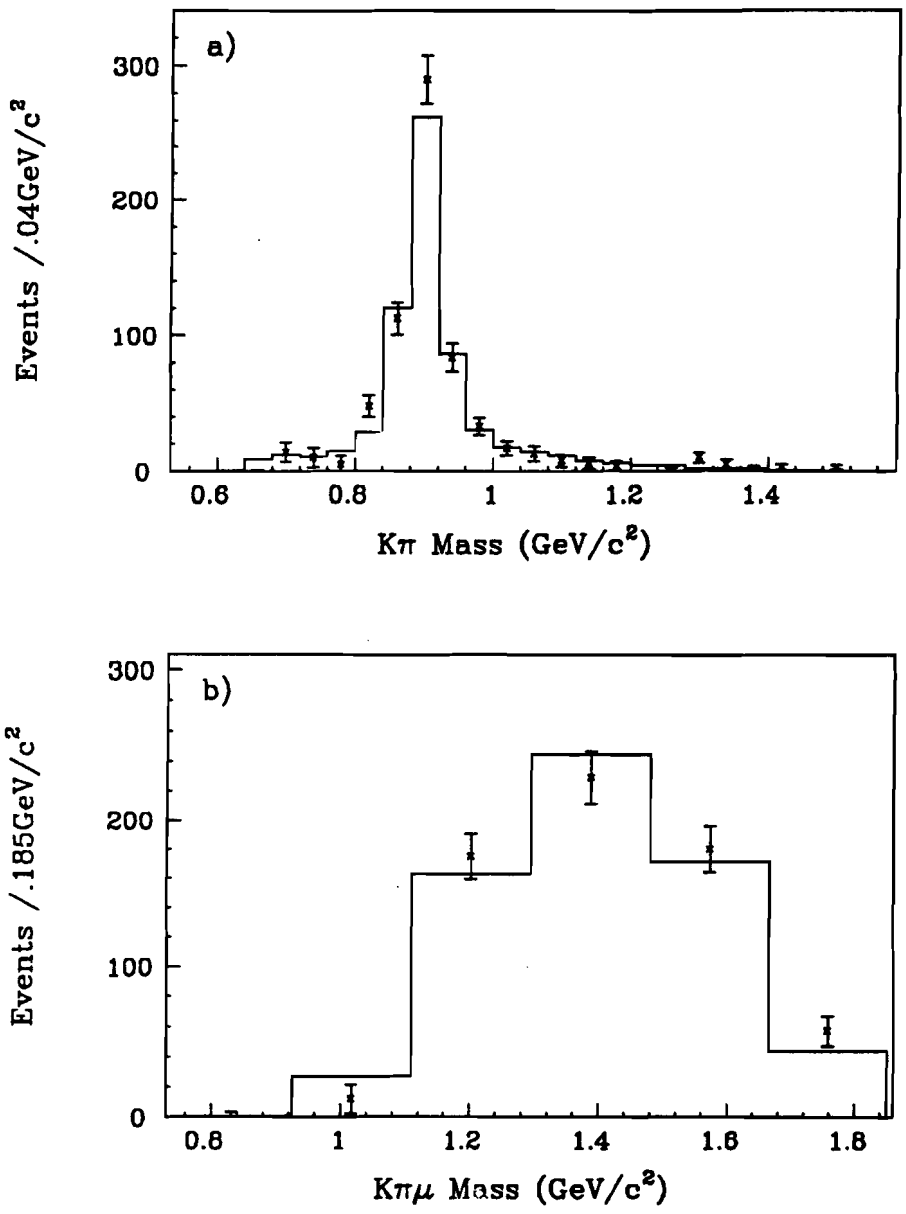

Figure 7.3. The projections of the nonresonant fit results. The data are shown as the points with the errors bars. The fit result is displayed as a solid histogram. The two dimensions are a) $M(K\pi)$ and b) $M(K\pi\mu)$.

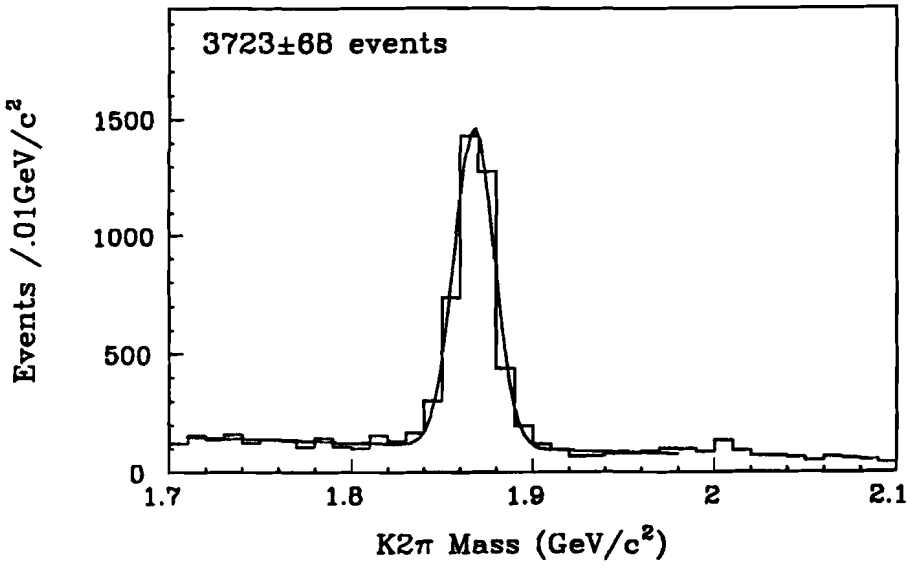

Figure 7.4. The invariant mass for the $K^-\pi^+\pi^+$ sample used for the branching ratio $\Gamma(D^+ \to \overline{K}^{*0}\mu^+\nu)/\Gamma(D^+ \to K^-\pi^+\pi^+)$

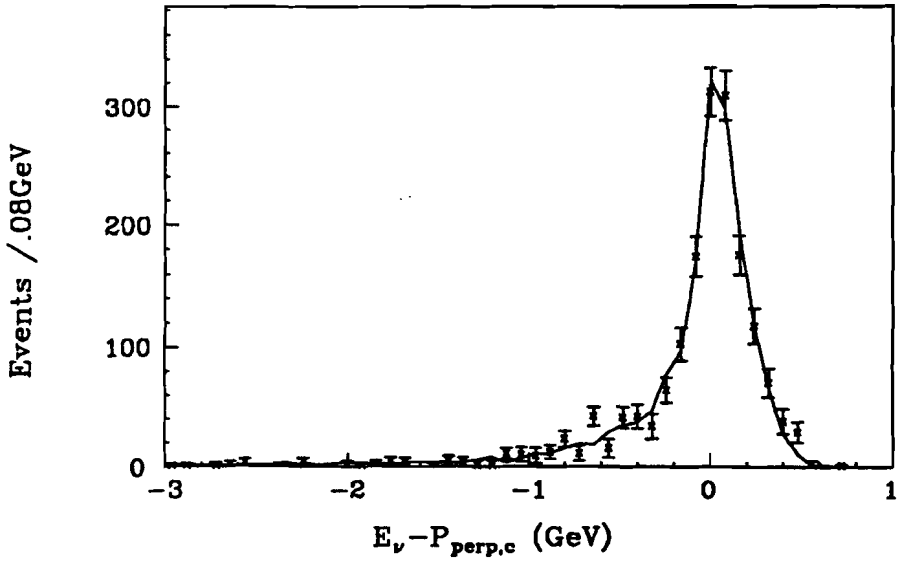

Figure 7.5. $E^*_\nu - p^*_{\perp c}$ for $D^+ \to \overline{K}^{*0}\mu^+\nu$ candidates. The data are shown as the points with error bars, the solid line is the Monte Carlo prediction.

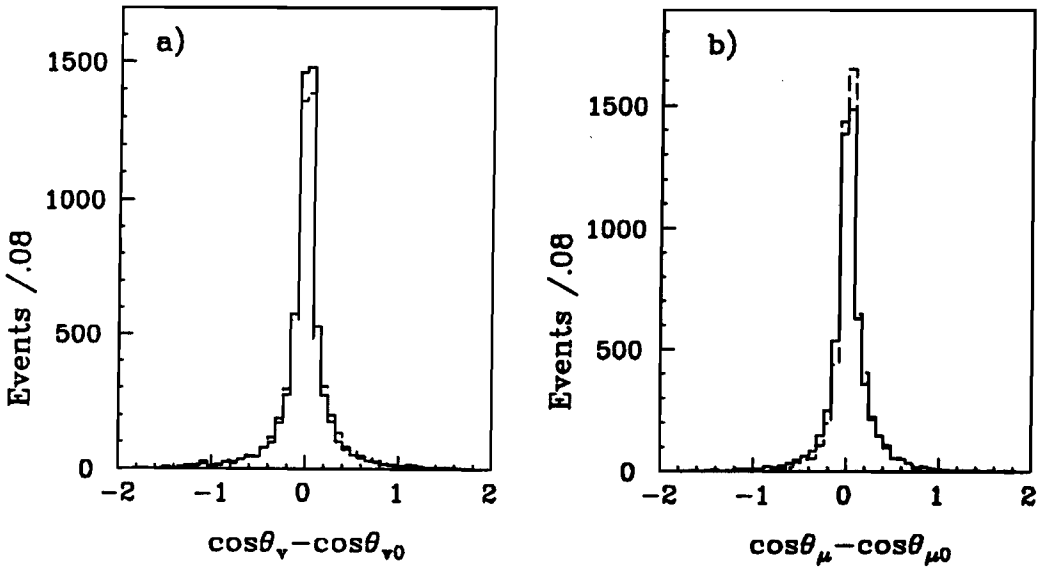

Figure 7.6. The distributions of the measured cosine minus the true cosine for Monte Carlo events. The solid histogram is for all events and the dashed histogram is for events that are not recovered. The two plots are a) $\cos\theta_v$ and b) $\cos\theta_\mu$.

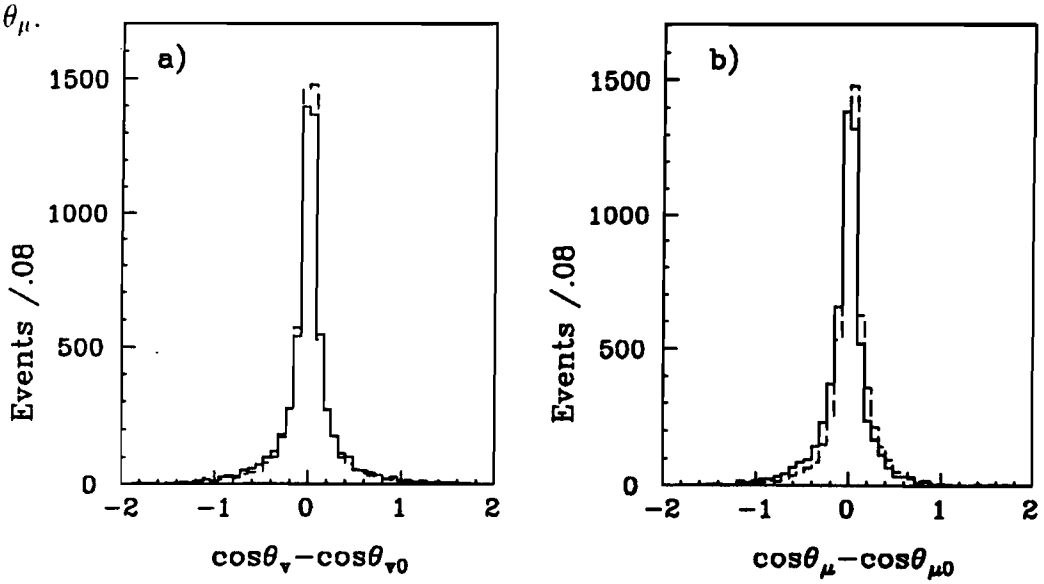

Figure 7.7. The distributions of the measured cosine minus the true cosine for Monte Carlo events. The solid histogram is for the high D momentum solution and the dashed histogram is for the low D momentum solution. The two plots are a) $\cos\theta_v$ and b) $\cos\theta_\mu$.

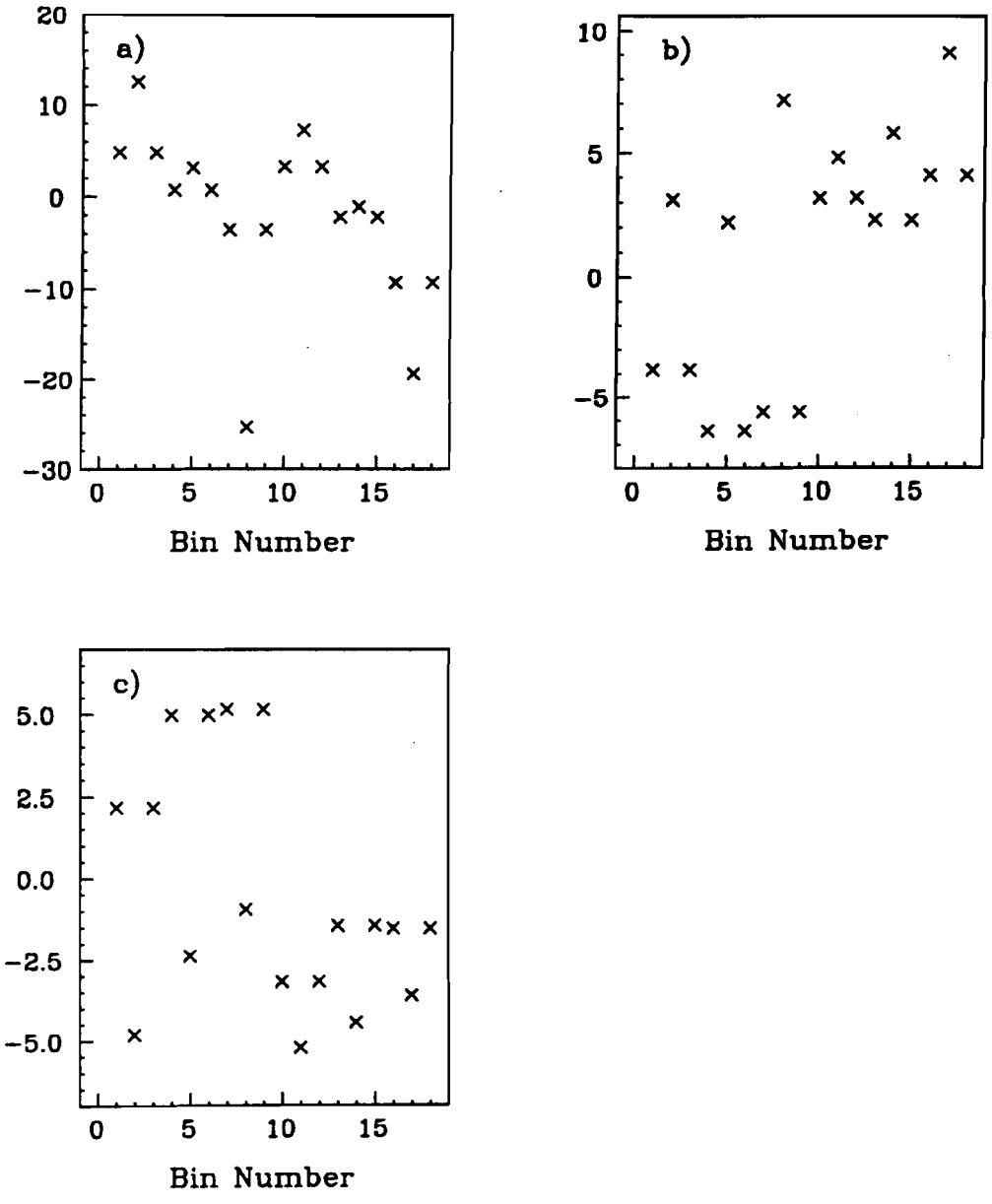

Figure 7.9. The 18 elements of the ρ matrix for a) R_v, b) R_2, and c) Γ_l/Γ_t

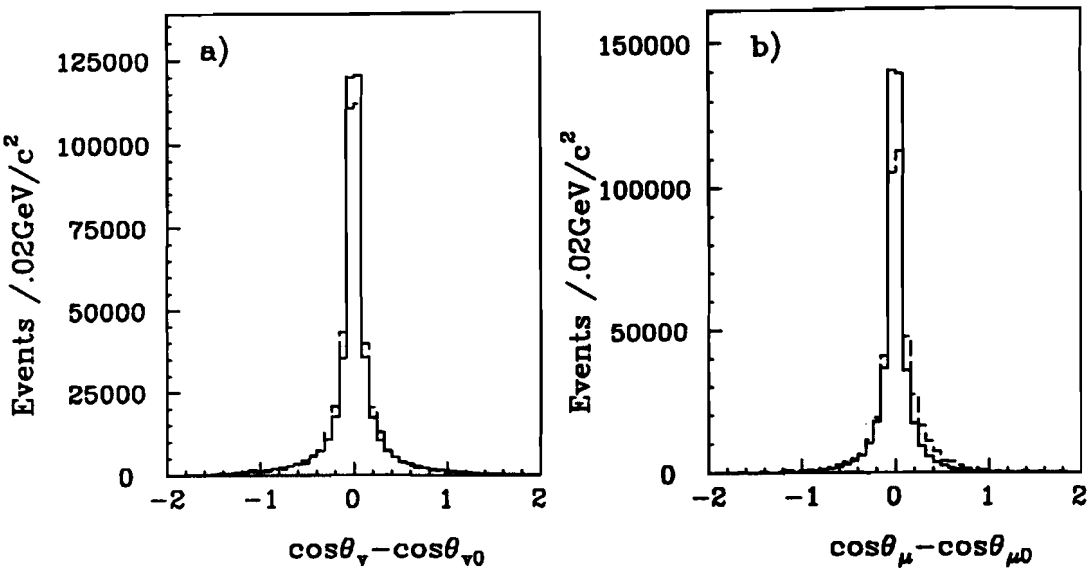

Figure 7.10. The distributions of the measured cosine minus the true cosine for Monte Carlo events. The solid histogram is for the mini-Monte Carlo and the dashed histogram is for the complete Monte Carlo. The two plots are a) $\cos\theta_\nu$ and b) $\cos\theta_\mu$.

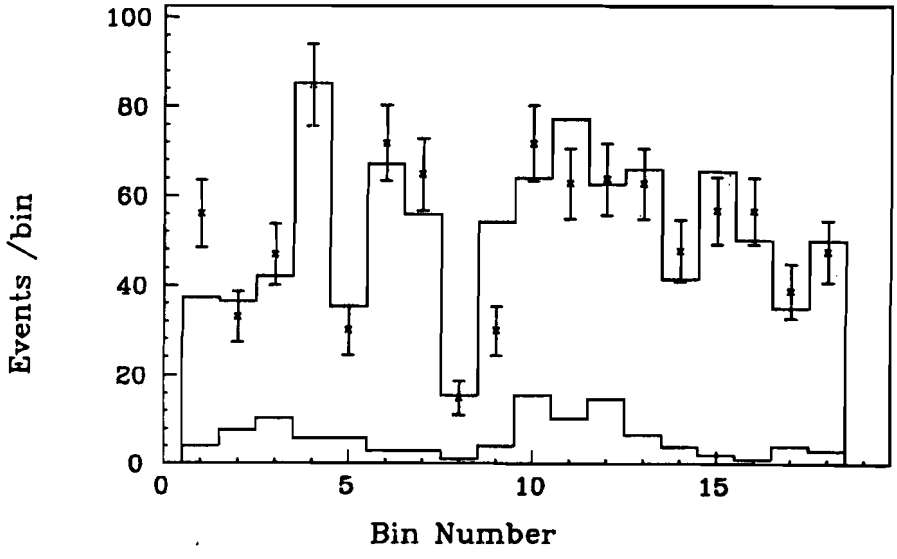

Figure 7.11. The form factor fit result. The data are shown as the points with the error bars, the upper histogram is the fit result, the lower histogram is the wrong-sign distribution which is used to estimate the background.

Chapter 8

$D^0 \to K^{*-}\mu^+\nu$

In this chapter we analyze the decay $D^0 \to K^{*-}\mu\nu$ with the $K^{*-}(892)$ detected in the $K_s\pi^-$ decay mode.

There is a big difference between this decay mode and $D^+ \to \overline{K}^{*0}\mu^+\nu$, discussed in Chapter 7. The basic analysis is similar: we find detached $\pi\mu$ vertices in events with a K_s, plot the $K_s\pi$ mass, and use the K^{*-} peak as the signal. The K_s decays downstream of the microstrips 85% of the time and in this case we cannot require that it is in the vertex with the π and μ. This results in a large background, mostly from events with a $X^-\mu^+$ vertex in one charm decay and a K_s from the recoil charm decay. We can, however, subtract the wrong-sign sample where the π and μ have the same charge to eliminate some non-charm background and charm backgrounds where the π and μ come from different vertices.

Following Chapter 7, we will first address the cuts used to extract a signal. Again, because we do not detect the neutrino, we are not fully reconstructing the decay so we will present tests that the signal dominated by the decay mode we are looking for.

After establishing the signal, we will present the ratio of the widths $\Gamma(D^0 \to K^{*-}\mu^+\nu)/\Gamma(D^+ \to \overline{K}^{*0}\mu^+\nu)$ We present this ratio as opposed to, for example, $\Gamma(D^0 \to K^{*-}\mu^+\nu)/\Gamma(D^0 \to K\pi)$ to reduce systematics. Also it is a test of the prediction $\Gamma(D^0 \to K^{*-}\mu^+\nu) \approx \Gamma(D^+ \to \overline{K}^{*0}\mu^+\nu)$. This follows from the fact that the weak semileptonic decays proceed by isosinglet currents which connect the isosinglet c and s quarks.

8.1 $D^0 \to K^{*-}\mu^+\nu$ Signal

We use the global vertex skim to search for the signal (see section 4.3.3). This skim should be efficient since it requires a mildly detected two-track vertex and

the signal we are looking for has a detached two-track vertex. Using this skim will also reduce systematics in the ratio of the widths presented below.

In this analysis, all tracks are searched for correct sign, mass, lepton and Cherenkov identification combinations to form $K_s\pi\mu$ candidates. The π and μ tracks must be found in the microstrips and the PWC system (they are linked). The muon is identified in the inner muon detector. The K_s must pass basic cleanup cuts (see section 4.1.7). The π and μ must not be identified as a kaon or proton by the Cherenkov system.

We require the $\pi\mu$ combination to form a good vertex with a confidence level greater than 10%. (When the K_s decays upstream of the microstrips, we include the K_s track in this fit.) The muon must have a momentum greater than 10GeV/c and the $K_s\pi\mu$ combination must have a momentum greater than 50GeV/c. Background from $D^0 \rightarrow K_s 2\pi$, where a pion is misidentified as a muon, is eliminated by requiring that the reconstructed $K_s\pi\mu$ mass be less than 1.8GeV/c^2.

We find the primary vertex by searching for the most upstream high-quality vertex in the target region that can be made from the tracks which remain after the $K_s\pi\mu$ combination is removed. This is the DVFREE algorithm explained in section 6.5.

Finally, we require that the $\pi\mu$ vertex be isolated from other tracks in the event (not including tracks in the primary vertex) by requiring that the maximum confidence level for another track to form a vertex with the candidate be less than 1%.

8.1.1 Signal Cut Response

Figure 8.1 shows the wrong-sign subtracted signals for several ℓ/σ cuts.

The first plot in Figure 8.2 shows the signal's survival *vs* the ℓ/σ cut compared to the survival predicted by our D^+ Monte Carlo. The very good agreement

indicates little contamination from shorter lived charm states or the longer-lived D^+

Figure 8.2b shows the signal survival as a function of the minimal confidence level requirement for the secondary vertex compared to that predicted by our Monte Carlo. The agreement is very good indicating there is negligible background from events where the π and μ do not originate from the same vertex.

Figure 8.2c compares the data and Monte Carlo response to the secondary vertex isolation cut. Here the vertex is more isolated as the confidence level cut gets smaller. Agreement is good indicating negligible potential background from charm states with an additional charged track in the same vertex as the $K_s\pi\mu$ candidate. We require this confidence level to be less than 1%.

8.2 $\Gamma(D^0 \to K^{*-}\mu^+\nu)/\Gamma(D^+ \to \overline{K}^{*0}\mu^+\nu)$

Table 8.1 shows the yields and efficiencies for these two decay modes.

Table 8.1. Semileptonic Signals

Signal	Yield	Efficiency	Corrected Yield
$D^0 \to K^{*-}\mu^+\nu$	243 ± 59	.01265	19200 ± 4700
$D^+ \to \overline{K}^{*0}\mu^+\nu$	874 ± 44	.02237	39000 ± 2000

We need to include some *post-hoc* corrections to the yield of D^+'s. Detailed comparisons of data and Monte Carlo show that the Monte Carlo is optimistic about the efficiency to link a PWC track to a microstrip track. Since the analysis of the D^+ mode requires the kaon is linked while there is no such requirement on the K_s in the D^0 mode, we will lower the D^+ yield by 3%.

We also correct for the presence of charm backgrounds where a pion has been misidentified as a muon. We have measured the probability of misidentification using the high-statistics all-charged decay $K2\pi$. $D^+ \to \overline{K}^{*0}\pi^+\pi^0$ can appear in the D^+ signal when the pion is misidentified as a muon so we lower the D^+ yield

by 1.3%. Similarly, because $D^0 \to K^{*-}\pi^+\pi^0$ can appear in the D^0 signal through misidentification, we lower the D^0 yield by 7%.

Finally, to extract the ratio of the widths we have to include production ratio of D^+/D^0 and the ratio of the total widths, which is the inverse of the ratio of the lifetimes, τ_+/τ_0:

$$\frac{\Gamma(K^{*-}\mu^+\nu)}{\Gamma(\overline{K}^{*0}\mu^+\nu)} = \frac{D^+}{D^0}\ \frac{\tau_+}{\tau_0}\ \frac{\text{Yield}(K^{*-}\mu^+\nu)}{\text{Yield}(\overline{K}^{*0}\mu^+\nu)} \tag{8.1}$$

In the 1988 data, E687 measured the production ratio $D^+/D^0 = 0.42 \pm .05$ [24]. This ratio was measured by comparing the yield of $D^0 \to K\pi$, $D^0 \to K3\pi$ and $D^+ \to K2\pi$ and correcting with the known [19] branching ratios. This production ratio is also consistent with a simple model where both isospin states (D^0 and D^+ or D^{*0} and D^{*+}) are photoproduced equally and the D^*'s (with their three spin states) are produced three times as often as the D's. This simple model, combined with the known [19] D^* branching ratios, lead to essentially the same production ratio.

In the 1988 data, E687 measured the lifetime ratio $\tau_+/\tau_0 = 2.52 \pm .17$ [25]. Putting the all the numbers together, we find the ratio of the partial widths is $1.37 \pm .34$.

Most of the systematics such as muon identification probability and trigger variations cancel. We include a 10% systematic for the potential mismodeling of the Cherenkov cut on the kaon in the D^+ decay mode and another 10% for the potential mismodeling of the K_s reconstruction efficiency in the D^0 mode.

Possible contamination of the D^0 from $K^{*-}\pi^0\mu^+\nu$ is included as an asymmetric systematic error of -32% from the current limit [26]. Possible contamination of the D^+ from $\overline{K}^{*0}\pi^0\mu\nu$ is included as an asymmetric systematic error of $+5\%$ from the limit presented in Chapter 7.

The result is consistent with the expected ratio of unity:

$$\frac{\Gamma(K^{*-}\mu^+\nu)}{\Gamma(\overline{K}^{*0}\mu^+\nu)} = 1.37 \pm .34 \, ^{+.15}_{-.35}$$

This is the first confirmation of the expectation that that weak current responsible for Cabibbo favored semileptonic decay acts as an isosinglet since it shows that one gets a consistent decay rate under the simultaneous rotation of the D^+ into the D^0 and the K^{*-} into the $\overline{K}^{*0}$. If we assume that the isospin test must work, this result could be interpreted as a test of the absolute branching ratios used to find the E687 D^+/D^0 production ratio.

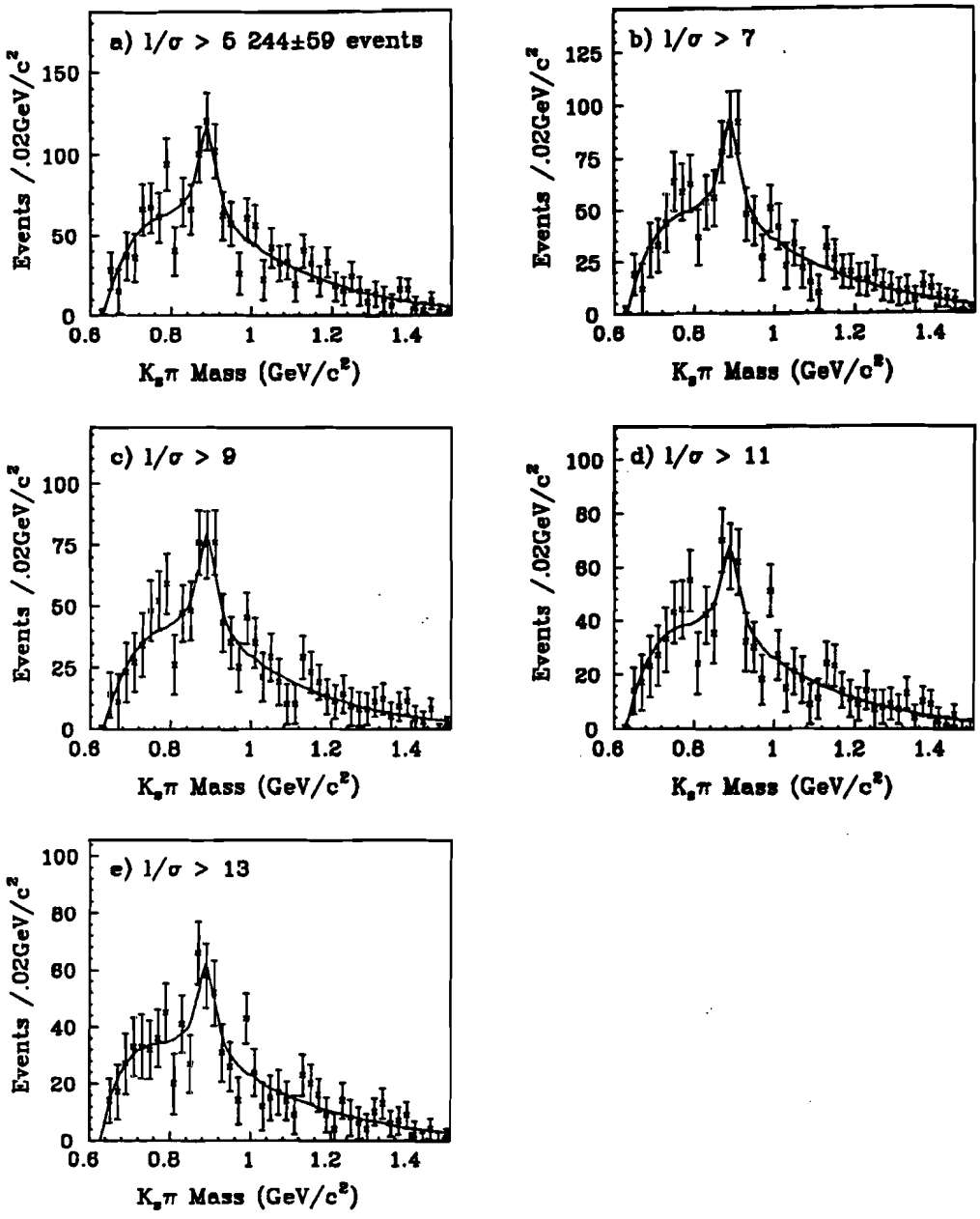

Figure 8.1. $D^0 \to K^{*-}\mu^+\nu$ signal after wrong-sign subtraction for the indicated ℓ/σ cuts. The data are the points with the error bars and the fit for the signal yield is the solid line. The fit uses a Monte Carlo prediction for the lineshape, based on our measurement of the form factors in Chapter 7. The background term is of the form $a_1 x^{a_2} e^{-a_3 x}$ where a_i are the fit parameters and x is $M(K_s\pi) - (M(K_s) + M(\pi))$.

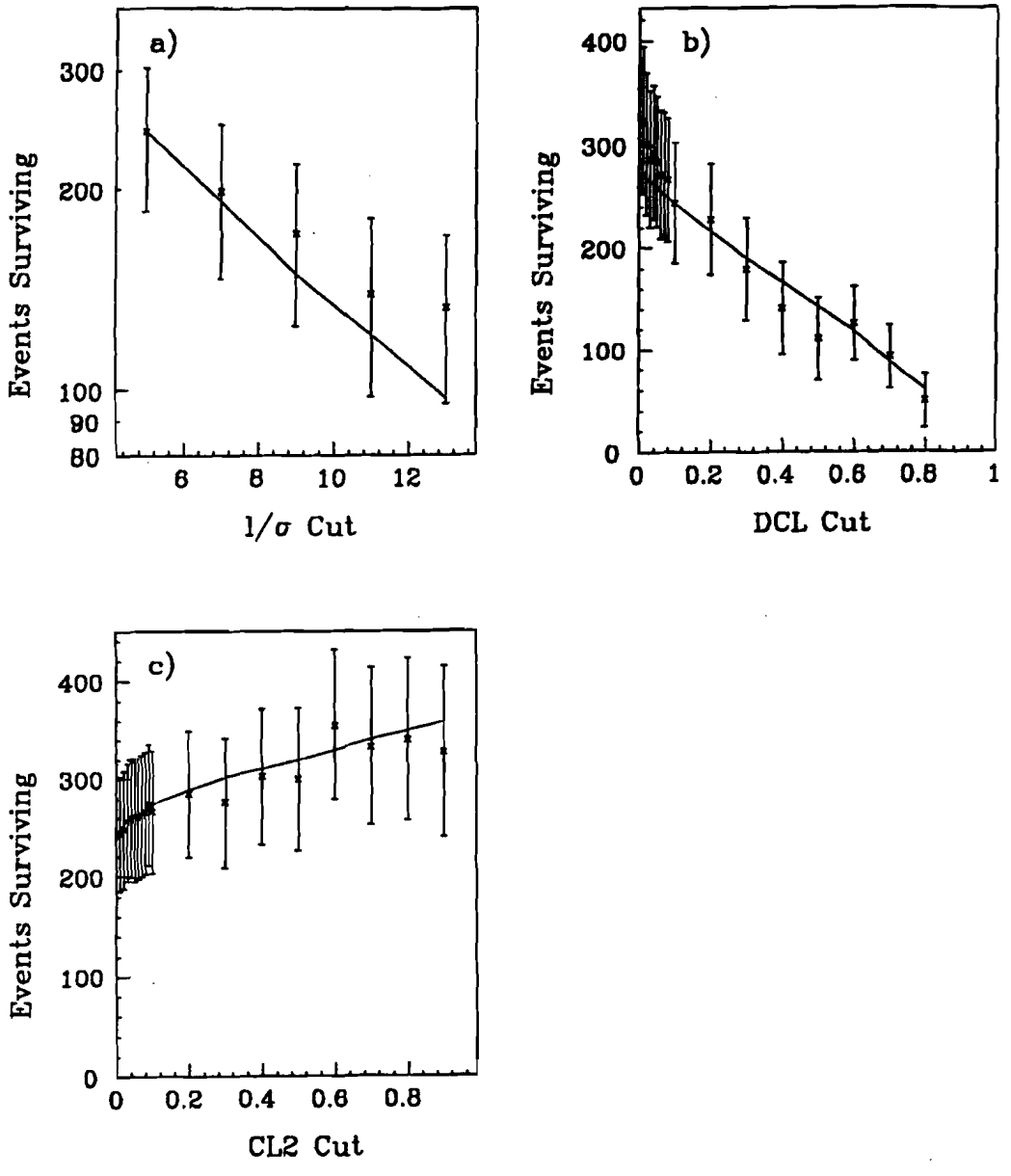

Figure 8.2. The $D^0 \to K^{*-}\mu^+\nu$ signal survival plotted *vs* the cut for a) $\ell/\sigma >$ cut, b) DCL< cut, and c) CL2 < cut. The solid lines are the Monte Carlo prediction.

Chapter 9

$D_s^+ \to \phi\mu^+\nu$

The decay $D_s^+ \to \phi\mu\nu$ is the D_s^+ analogy of the decay $D^+ \to \overline{K}^{*0}\mu\nu$ discussed in Chapter 7. As discussed in [19], this branching ratio is used to normalize all D_s^+ branching ratios. Theory predicts $\Gamma(D_s^+ \to \phi\mu\nu) \approx \Gamma(D^+ \to \overline{K}^{*0}\mu\nu)$. This prediction, combined with the branching ratio reported in this chapter, the D^+ and D_s^+ lifetimes, and $\Gamma(D^+ \to \overline{K}^{*0}\mu\nu)$ allows us to calculate the partial width $\Gamma(D_s^+ \to \phi\pi)$. This is critical because all other D_s^+ branching ratios are measured as ratios to $\phi\pi$.

In this chapter we will discuss the analysis used to find the $D_s^+ \to \phi\mu\nu$ signal. As in the D^+ case, we are only reconstructing part of the final state because we do not detect the neutrino so we discuss the signal's response to analysis cuts, investigating possible contaminations. Next, we perform a fit to distinguish the signal from background using all the available kinematic information. Next, we obtain a signal in $D_s^+ \to \phi\pi$ and report a measurement of $\Gamma(D_s^+ \to \phi\mu\nu)/\Gamma(D_s^+ \to \phi\pi)$. Finally we report a new measurement of $\Gamma(D_s^+ \to \phi\pi)/\Gamma(D_s^+ \to \text{all})$

9.1 Analysis Method

Following the D^+ semileptonic analysis, we will find detached $K^+K^-\mu^+$ vertices, plot the K^+K^- mass and use the ϕ peak as the signal.

In the D^+ case we can find wrong-sign muons with a $\overline{K}^{*0}$ because of the $K-\mu$ charge correlation of the signal. This allows us to subtract backgrounds from a random muon with a $\overline{K}^{*0}$. In the D_s^+ case, we have a $\phi \to K^-K^+$ for the resonance so there is no $K-\mu$ charge corelation to separate a right-sign from wrong-sign and allow the subtraction of the background from a ϕ combined with a random muon. Without a wrong-sign subtraction we have to even more careful that all backgrounds are removed or understood.

To begin, we find all ϕ candidates which form a good vertex (DCL> .2) with a muon identified in the inner muon detector. We call DVFREE to find the

primary vertex and require $\ell/\sigma > 3$. We require CL2< .1 and KP Cherenkov identification on both kaon candidates. To avoid a possible contamination from diffractively produced ϕ's, we require the $p_\perp^2$ of the ϕ is greater than .05GeV^2/c^2.

Figure 9.1 shows the ϕ mass histogram for candidates passing these cuts for the 1990 and 1991 data sample.

9.2 Signal Cut Response

Figure 9.2 shows the ϕ signal response for successively larger ℓ/σ cuts. Figure 9.3a shows the ϕ yield *vs* the ℓ/σ cut and compares it to the $D_s^+ \to \phi\mu\nu$ Monte Carlo prediction, showing good agreement. This implies the signal is not dominated by a D^+ signal which would have a significantly longer survival, or any background with a lifetime different from the D_s^+.

Figure 9.3b-d shows the ϕ yield *vs* three different analysis cuts compared to the $D_s^+ \to \phi\mu\nu$ Monte Carlo prediction. The first (b) shows the DCL cut response has a significant build-up at low DCL compared the Monte Carlo. This implies a significant background from events where the $\phi\mu$ did not originate from a single vertex. To avoid this background we require DCL> .2 for all further analysis.

The dashed line on Figure 9.3b, the DCL cut response, is the result of running the analysis on a $c\bar{c}$ LUND Monte Carlo. This Monte Carlo will have the signal as well as all known charm decay modes in approximately the right ratios. We find the DCL response tends to peak up at low DCL, like the data. We find this background is from $D_s^+ \to \phi\pi\pi^0$, with the π going undetected and the muon from the semileptonic decay of the $\bar{c}$ meson. (Also see the discussion of DCL in section 6.2.)

Figure 9.3c shows the response to the CL2 cut, again we are seeing a build-up, but this time it is at large CL2 where we expect backgrounds from higher-multiplicity decay modes such as $\phi 3\pi$ with a π being misidentified as a μ. We

can greatly reduce this background by requiring CL2< .1. Figure 9.3d shows the CL1 response agrees very well.

Figure 9.4 compares the ϕ signal's $KK\mu$ mass to the Monte Carlo prediction. The agreement is reasonable, the data might tend to a lower $KK\mu$ mass.

Figure 9.5 shows the $p_\perp^2$ (relative to the beam direction) distribution for the ϕ. This distribution shows a small excess at very low $p_\perp^2$ which is not predicted by the Monte Carlo. This is probably due to diffractively produced ϕ's from beam photons combined with a random muon. To avoid these ϕ's completely we require $p_\perp^2 > .05$ for the final branching ratio.

9.3 Kinematic Fit

To extract the yield of $D_s^+ \to \phi\mu\nu$ we will fit the distributions of the kinematic variables. In practice, we find the most difficult background to discriminate against is $\phi\pi^0\mu\nu$.

We can reconstruct all the kinematics of the decay using the method outlined in Chapter 7 for $D^+ \to \overline{K}^{*0}\mu\nu$. We can then proceed to calculate the magnitude of the matrix element for each $D_s^+ \to \phi\mu\nu$ candidate. As discussed in Chapter 2, the values for R_v and R_2 for the D_s^+ decay should be the same as for the D^+ decay [12]. $D_s^+ \to \phi\mu\nu$ decays should proceed by the semileptonic matrix element and preferentially populate larger values of the matrix element than decays that proceed through phase space, allowing some discrimination between the two.

Figure 9.6 shows six possible distributions that we could use to try to separate the signal from backgrounds. We show the expected distributions for the signal and the $\phi\pi^0\mu\nu$ contamination. In this figure we see that the $\phi\mu$ mass should discriminate between the signal and the $\phi\pi^0\mu\nu$, but the distribution of the matrix element is not a good discriminant. This is because $\phi\pi^0\mu\nu$ populates lower values of $\cos\theta_\mu$ which has a large value of the matrix element.

Of the three variables which are used to characterize the angular decay distribution, only $\cos\theta_\mu$ and $\cos\theta_v$ show good discrimination power, $y = t/t_{max}$

does not. On the ϕ resonance, one can compute the $\phi\mu$ mass given $\cos\theta_\mu$ and $y = t/t_{max}$. Therefore we expect no gain in overall discrimination power by including all three angular discriminants rather than just any two of the three. Because of the similarity between the signal and background y distributions, we also expect a fairly modest gain in discrimination power by including, say, $\cos\theta_\mu$ as well as the $\phi\mu$ mass compared to the use of the $\phi\mu$ mass as the sole angular discriminant.

To quantitatively determine which discriminants are best and what bin sizes are needed, we calculate the effectiveness of each choice of discriminant and binning. We work with a simplified model where there is only the signal and the $\phi\pi^0\mu\nu$ contamination and there is no non-ϕ background. We bin the Monte Carlo distributions and calculate the estimated error in a binned likelihood fit with one fit parameter, f, which is the fraction of events that are the background, additional π^0, mode:

$$\frac{1}{\sigma^2} = \frac{1}{2}\frac{d^2w}{df^2} \qquad w = -2\ln\mathcal{L} \tag{9.1}$$

$$\mathcal{L} = \sum_{bins} \frac{\mu_i^{N_i}\epsilon^{-\mu_i}}{N_i!} \qquad \mu_i = (1-f)f_{sig} + f f_{\pi^0} \qquad N_i = (1-f_0)f_{sig} + f_0 f_{\pi^0}$$

We compute these *a priori* errors for the case of a parent population background level of $f_0 = 27\%$. Because the parent bin populations are normalized to unity, the calculation will return $\sigma\sqrt{N}$ where N is the total ϕ yield.

Table 9.1. ϕ Fit Discriminants

N $M(\phi\pi)$	N y	N M.E.	N $\cos\theta_v$	N $\cos\theta_\mu$	$\sigma\sqrt{N}$
5	1	1	1	1	1.58
1	5	1	1	1	7.15
1	1	5	1	1	7.71
1	1	1	5	1	4.23
1	1	1	1	5	1.66
8	1	1	1	1	1.53
5	1	1	1	5	1.54
5	5	1	1	1	1.53
5	5	1	1	5	1.49
5	1	1	3	1	1.54
5	1	1	5	1	1.53
5	1	1	5	5	1.46
6	1	1	5	4	1.46

We can see immediately that, as expected, neither y or the matrix element provides any significant discrimination power as indicated by the large error predicted for the (1,5,1,1,1) and (1,1,5,1,1) cases. Similarly, we find $\cos\theta_v$ has a little more power and $M(\phi\pi)$ and $\cos\theta_\mu$ have good discrimination power. The (8,1,1,1,1) case compared to the (5,1,1,1,1) case indicates that we don't need to add any more bins to $M(\phi\pi)$. Comparing the (5,5,1,1,5) to (5,1,1,1,5) and (5,5,1,1,1) we see that $M(\phi\pi)$, y, and $cos\theta_\mu$ are mostly not independent because including all three does not improve the error over using any two.

Going from (5,1,1,3,1) to (5,1,1,5,1) does not significantly improve the error, indicating only three bins are necessary in $cos\theta_\mu$. We will proceed with the last set, (6,1,1,5,4), because it has the best predicted error. We go with 6 bins in

$M(\phi\pi)$ to get the maximum power from that variable and include both $\cos\theta_v$ and $\cos\theta_\mu$.

Finally, to separate $\phi\mu\nu$ from potential D^+ backgrounds, we use the proper time distribution as the last distribution to fit. We fit to the joint distribution of $M(\phi\pi)$, $\cos\theta_v$, and $\cos\theta_\mu$ and the projection of the proper time since we expect the proper time to be uncorrelated with the other variables.

The decay modes which we allow in ϕ fit are presented in Table 9.2. For the modes with measured branching ratios we also report the fraction of the ϕ signal expected from this mode. Note that $D^+ \to \phi\mu\nu$ is not expected to be seen because it is Cabibbo suppressed and the $d\bar{d}$ in the final state quark diagram must rescatter to form a ϕ. We also do not expect to see any significant $D_s^+ \to \phi\pi^0\mu\nu$ because the the formation of the additional π^0 from gluons is Okubo-Zweig-Iizuka suppressed. As reported in Chapter 7, the equivalent decay for the D^+, $\overline{K}^{*0}\pi^0\mu\nu$ is not seen and is limited to be very small relative to $D^+ \to \overline{K}^{*0}\mu\nu$.

Table 9.2. ϕ Fit Considered Decay Modes

Decay Mode	Matrix Element	Estimate (% of ϕ's)
$D_s^+ \to \phi\mu\nu$	s.l.	-
$D^+ \to \phi\mu\nu$	s.l.	< 12
$D_s^+ \to \phi\pi\pi^0$	p.s.	5.8 ± 3.5
$D_s^+ \to \phi 3\pi$	p.s.	$.39 \pm .18$
$D^+ \to \phi\pi\pi^0$	p.s.	5.1 ± 3.3
$D^+ \to \phi\overline{K}^0\mu\nu$	p.s.	-
$D_s^+ \to \phi\pi^0\mu\nu$	p.s.	-

The estimate of the background level is made from a combination of the relative efficiencies of the the background and signal, the branching ratios for the modes, our measurement of the muon misidentification probability, ($\kappa = .0088$), and, for the D^+ mode, the production ratio, $D_s^+/D^+ = .6 \pm .2$, which is estimated

from the the yields of D^+, $D_s^+ \to KK\pi$, and their known [19] branching ratios. For example, for the $D^+ \to \phi\pi\pi^0$ mode:

$$\%\text{contamination} = \frac{BR(D^+ \to \phi\pi\pi^0)}{BR(D_s^+ \to \phi\mu\nu)} \frac{\epsilon(D^+ \to \phi\pi\pi^0)}{\epsilon(D_s^+ \to \phi\mu\nu)} \frac{D^+}{D_s^+} \kappa = 5.1 \pm 3.3\%$$

The fit is binned maximum likelihood and the fit function is simply the Monte Carlo distributions of the three kinematic variables. To subtract the non-ϕ background, we add the distribution of the events in the ϕ high and low sidebands to the fit prediction. The errors are slightly underestimated because we are ignoring fluctuations in the non-ϕ background distribution about the parent population. The fit variables are the fractions of the ϕ signal in each decay mode. There is a constraint that the sum of the fractions is one.

The fit results are summarized in Table 9.3.

Table 9.3. ϕ Fit Results (%)

Decay Mode	fraction (%)
$D_s^+ \to \phi\mu\nu$	58 ± 19
$D^+ \to \phi\mu\nu$	4 ± 6
$D_s^+ \to \phi\pi\pi^0$	6 ± 3
$D_s^+ \to \phi 3\pi$	$.4 \pm .2$
$D^+ \to \phi\pi\pi^0$	6 ± 3
$D^+ \to \phi\overline{K}^0\mu\nu$	5 ± 7
$D_s^+ \to \phi\pi^0\mu\nu$	21 ± 20

Figure 9.7 shows the fit results displayed over the data distributions of the three kinematic variables. The large errors on the signal and $\phi\pi^0\mu\nu$ yield indicates that there is little power to discriminate between the two and the fit is consistent with a large of of combinations of these two modes. The yield of signal plus $\phi\pi^0\mu\nu$ is $79 \pm 9\%$. We will proceed assuming that this sum is actually all

signal. This is standard assumption used by other workers [27,28,29] and we are consistent with no $\phi\pi^0\mu\nu$. If we fit without the $\phi\pi^0\mu\nu$ background, we find the signal fraction is 76 ± 9, completely consistent.

If we assume there is no contribution from $D^+ \to \phi\mu\nu$, $D^+ \to \phi\overline{K}^0\mu\nu$, and $D_s^+ \to \phi\pi^0\mu\nu$ which are expected to be insignificant, and simply subtract the expected levels of the other contaminants, we find the ϕ peak is $89 \pm 6\%$ signal. Figure 9.8 shows data distributions overlayed with the prediction under these assumptions.

9.4 $\Gamma(D_s^+ \to \phi\mu^+\nu)/\Gamma(D_s^+ \to \phi\pi^+)$

We find the $D_s^+ \to \phi\pi$ signal in the same skim and with the vertexing and cuts except for the muon cuts and we require $\ell/\sigma > 5$. We look at three D_s^+ signal regions based on the D_s^+ mass error, 9.505MeV/c^2. We take $\pm 2\sigma$ as the signal region with weight= 1 and two sidebands $\pm 4\sigma$ to $\pm 6\sigma$ with weight= -1 and make a weighted histogram of the KK mass. The resulting signal is Figure 9.9.

The branching ratio is found separately in 1990 and 1991 data since we expect significantly different muon efficiencies. The semileptonic efficiencies include the small (15%) effect of the matrix element. The numbers in Table 9.4 shows the yields, uncorrected by the results of the fit for contamination.

Table 9.4. Branching Ratio Signals

Mode	Yield	efficiency (%)
$D_s^+ \to \phi\mu\nu$ ('90)	44 ± 9	2.595
$D_s^+ \to \phi\pi$ ('90)	98 ± 14	4.548
$D_s^+ \to \phi\mu\nu$ ('91)	81 ± 13	1.447
$D_s^+ \to \phi\pi$ ('91)	203 ± 20	3.395

The resulting branching ratio, uncorrected for contamination but with a 5% correction for the target absorption of the extra hadron in $\phi\pi$, is $.75 \pm .18$ in

the '90 data and $.89 \pm .17$ in the '91 data. These two are completely consistent so we proceed to combine them and find $.82 \pm .12$. Taking the results of the contamination fit which gives 79±9% signal, the branching ratio becomes .65±.12. Since the $c\bar{c}$ Monte Carlo predicts some contamination, about 10%, from $\phi\pi\pi^0$ with a muon from the $\bar{c}$ decay, and since the data response to the DCL cut shows a slight excess at DCL> .2 compared to DCL> .4, also about 10%, we will make a *post-hoc* correction by lowering the branching ratio by 10% to $.58 \pm .11$.

As the main source of systematic error we take the difference in this measurement and the result if we ignore the kinematic fit and simply subtract the expected backgrounds. This method gives a 13% systematic. The other sources we expect are 5% for the difference in absorption and scattering of the additional hadron in $\phi\pi$, and 3% for the possible variations in the HC triggering thresholds.

Table 9.5 compares this measurement to the other measurements available.

Table 9.5. Branching Ratio Measurements

Experiment	Signal	BR
E687 (μ)	97 ± 17	$.58 \pm .11 \pm .08$
E691[27] (e)	-	$< .45$
CLEO[28] ($\mu + e$)	$(17 \pm 6) + (37 \pm 9)$	$.49 \pm .10^{+.10}_{-.14}$
ARGUS[29] (e)	104 ± 26	$.57 \pm .15 \pm .15$

9.5 $\Gamma(D_s^+ \to \phi\pi^+)/\Gamma(D_s^+ \to \text{all})$

To calculate the absolute width for $D_s^+ \to \phi\pi$ we use the formula:

$$\frac{\Gamma(D_s^+ \to \phi\pi^+)}{\Gamma(D_s^+ \to \text{all})} = \frac{\Gamma(D_s^+ \to \phi\pi^+)}{\Gamma(D_s^+ \to \phi\mu^+\nu)} \frac{\tau(D_s^+)}{\tau(D^+)} \frac{\Gamma(D^+ \to \overline{K}^{*0}\mu^+\nu)}{\Gamma(D^+ \to \text{all})} \frac{\Gamma(D_s^+ \to \phi\mu^+\nu)}{\Gamma(D^+ \to \overline{K}^{*0}\mu^+\nu)} \tag{9.2}$$

where we have used the fact that $\Gamma(X \to \text{all}) = \hbar/\tau_X$.

The last factor relating the dominant semileptonic widths of of the D^+ and D_s^+ is expected[13] to range from .78 to 1.02, we will use $.9 \pm .12$. We use a lifetime ratio taken from our recent measurement[30] of the D_s^+ lifetime ($0.475 \pm 0.02 \pm .007$ ps) and the world average [19] lifetime for the D^+ ($1.066 \pm .023$ps). The $D^+ \rightarrow \overline{K}^{*0}\mu\nu$ width is obtained using the measurement of the $\overline{K}^{*0}\mu\nu$ branching ratio relative to $K^-\pi^+\pi^+$ presented in Chapter 7 ($.56 \pm .04 \pm .06$) and the present world average [19] absolute branching ratio for $D^+ \rightarrow K^-\pi^+\pi^+$ ($8 \,^{+.8}_{-.7}\%$). The result is $\Gamma(D_s^+ \rightarrow \phi\pi^+)/\Gamma(D_s^+ \rightarrow \text{all}\ ) =$ ($3.1 \ \pm .6$(stat) $\pm .5$ (sys) $\pm .4$ (theoretical))%. This compares well the current world average, $2.8 \pm .5\%$.

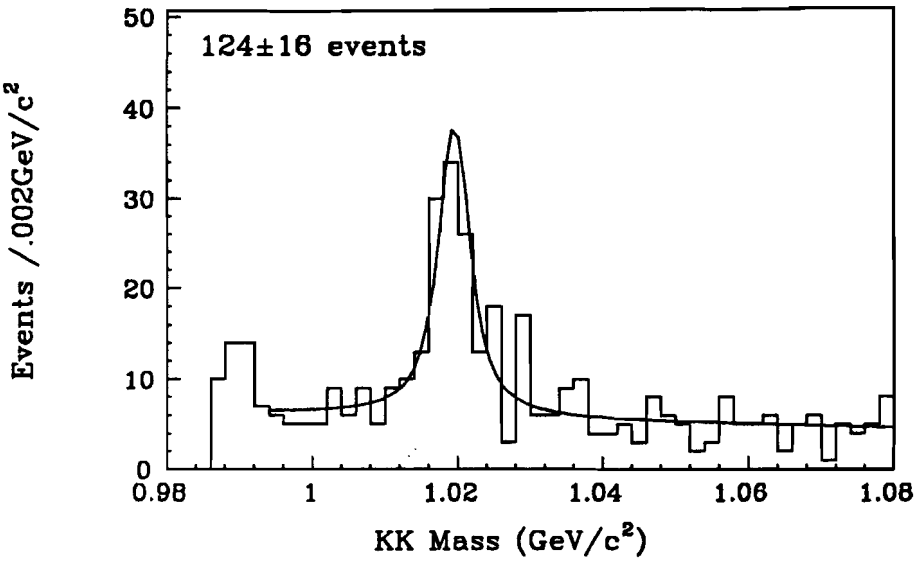

Figure 9.1. $D_s^+ \rightarrow \phi\mu^+\nu$ signal. The data is the histogram and the fit for the signal yield is the solid line. The fit is a Breit-Wigner with the known [19] ϕ width, convoluted with a Gaussian of width 1MeV/c^2 which is our measurement error, from Monte Carlo. The background is a linear function.

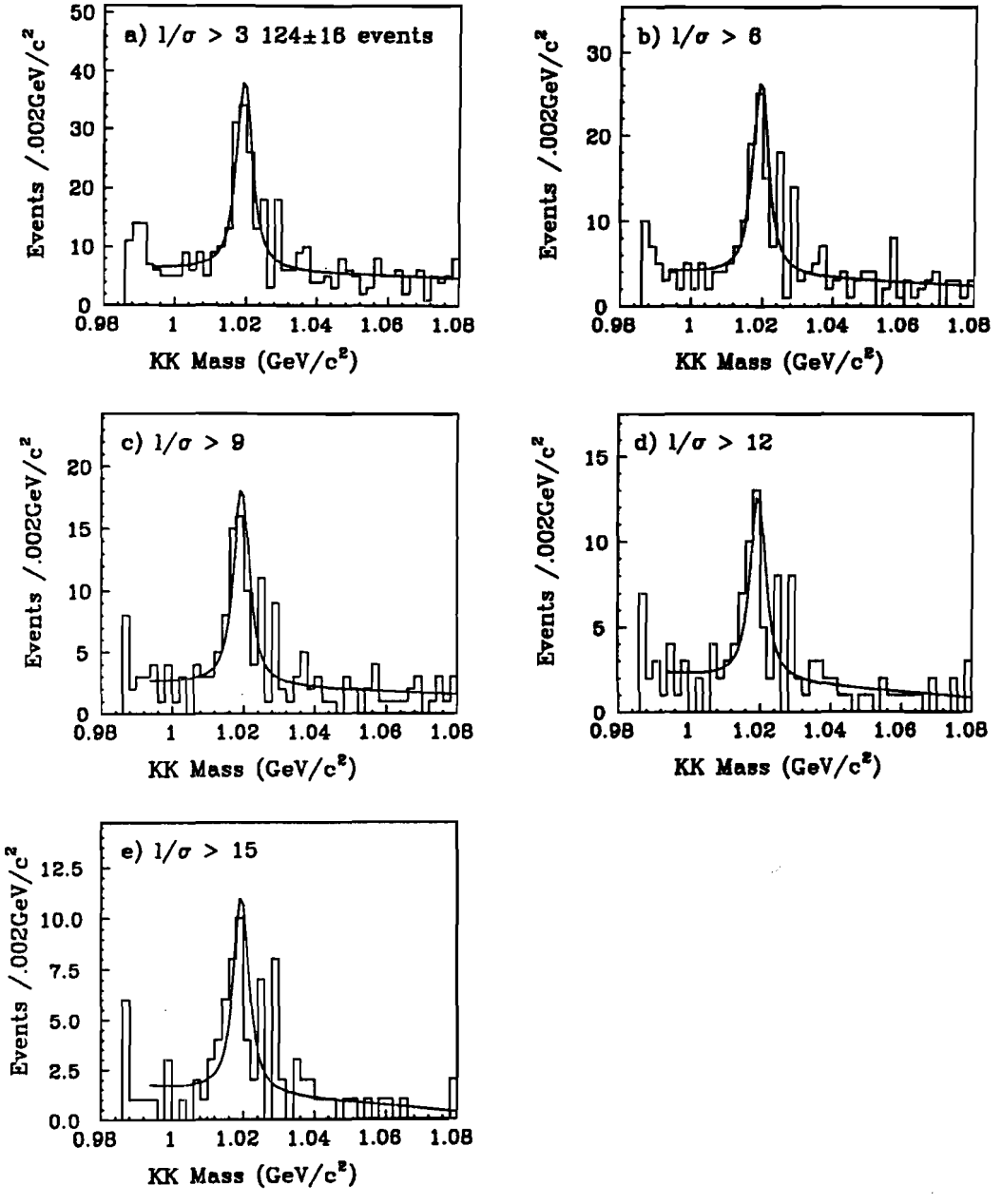

Figure 9.2. $D_s^+ \to \phi\mu^+\nu$ signal for the indicated ℓ/σ cut.

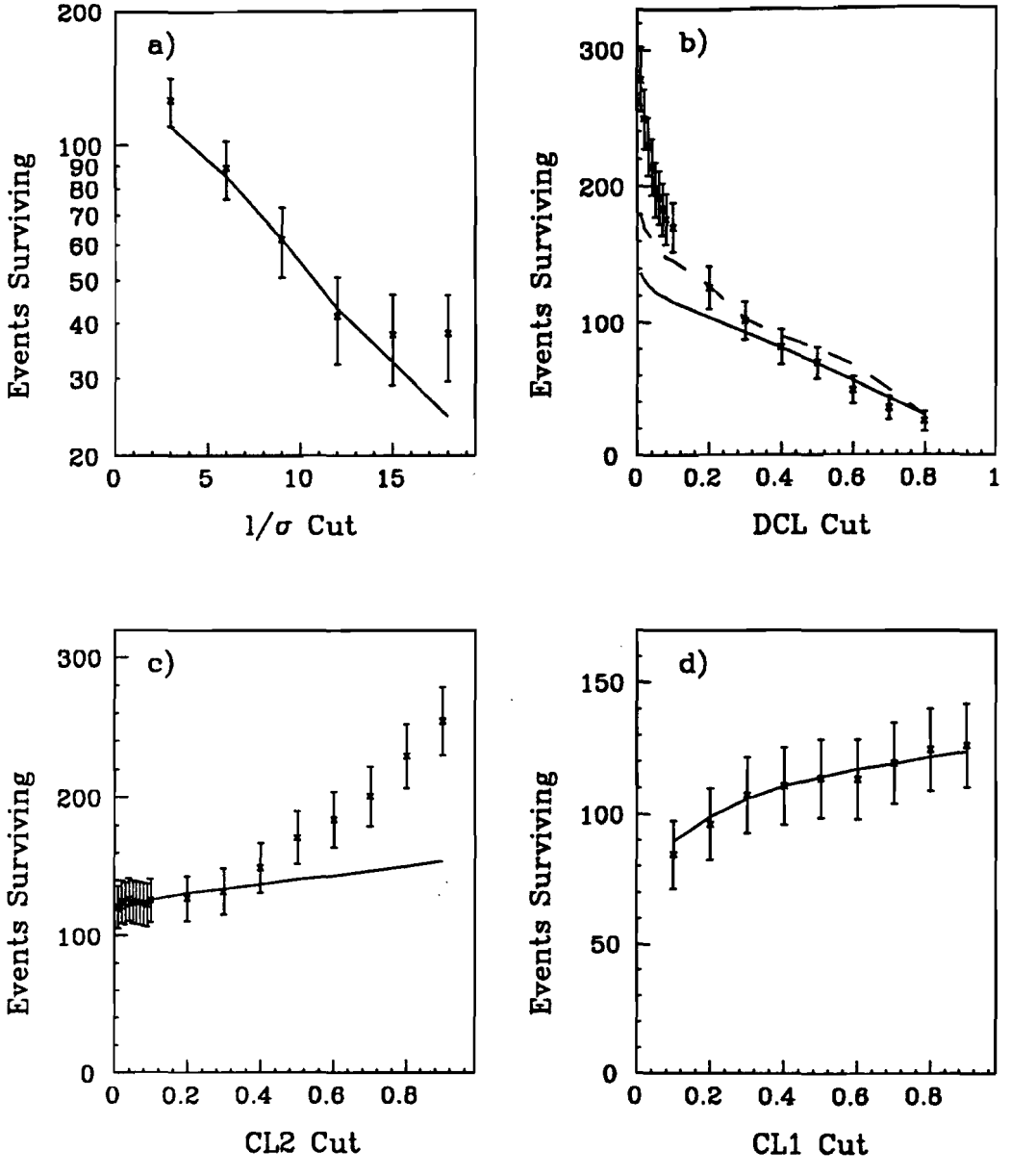

Figure 9.3. The $D_s^+ \to \phi\mu^+\nu$ signal survival plotted *vs* the cut for a) $\ell/\sigma >$ cut, b) DCL> cut, c) CL2< cut, and d) CL1< cut. The solid lines are the Monte Carlo prediction for signal. The dashed line in b) is the prediction of a $c\bar{c}$ Monte Carlo.

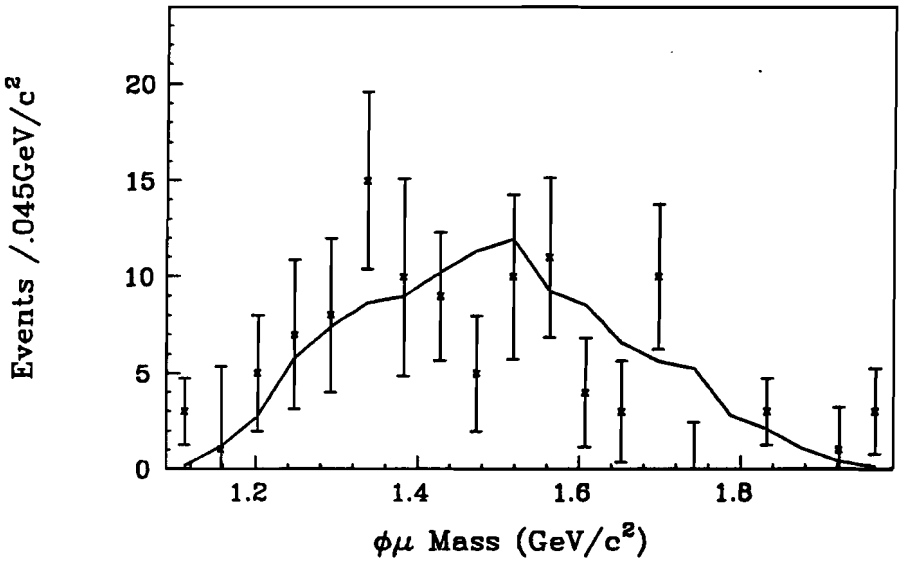

Figure 9.4. The distribution of the $\phi\mu$ mass for ϕ region candidates after subtracting the ϕ sidebands. The data are the points with the errors bars. The solid line is the Monte Carlo prediction.

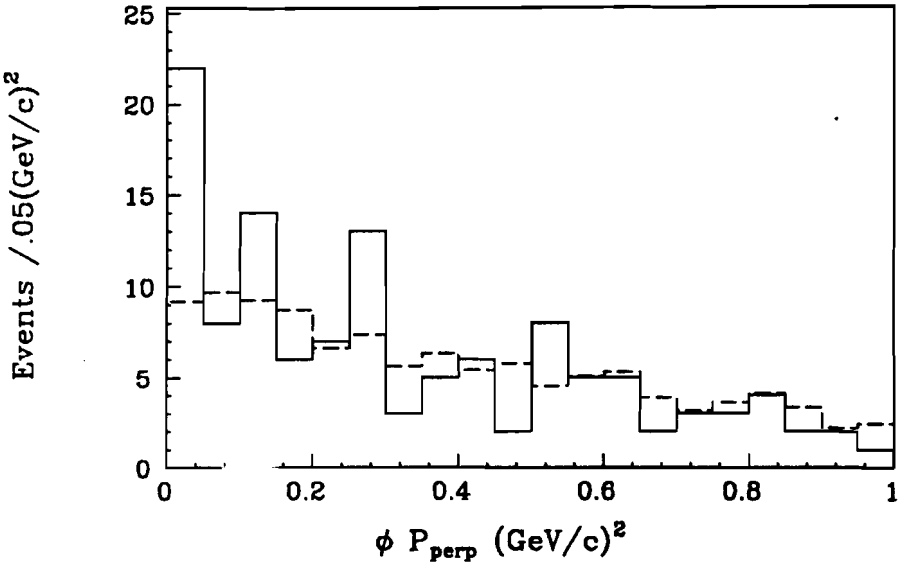

Figure 9.5. The distribution of the ϕ $p_\perp$ for ϕ region candidates. The data is the solid histogram, the Monte Carlo prediction is the Monte Carlo prediction.

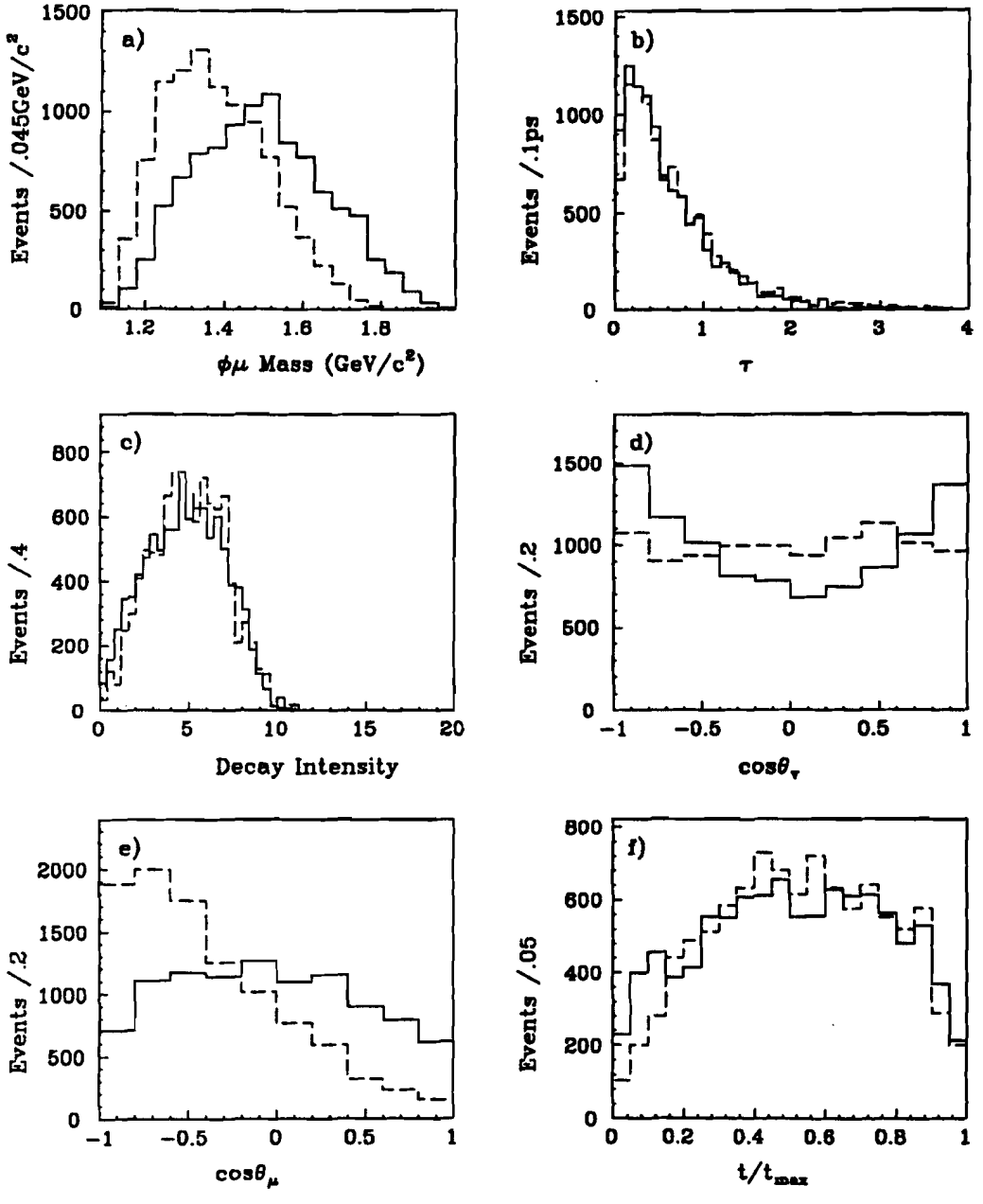

Figure 9.6. The Monte Carlo predictions for the distributions of kinematic variables for signal (solid) and $\phi\pi^0\mu\nu$ (dashed). The distributions are a) $M(\phi\mu)$, b) the proper time, c) the decay intensity, d) $\cos\theta_v$, e) $\cos\theta_\mu$, and f) t/t_{max}.

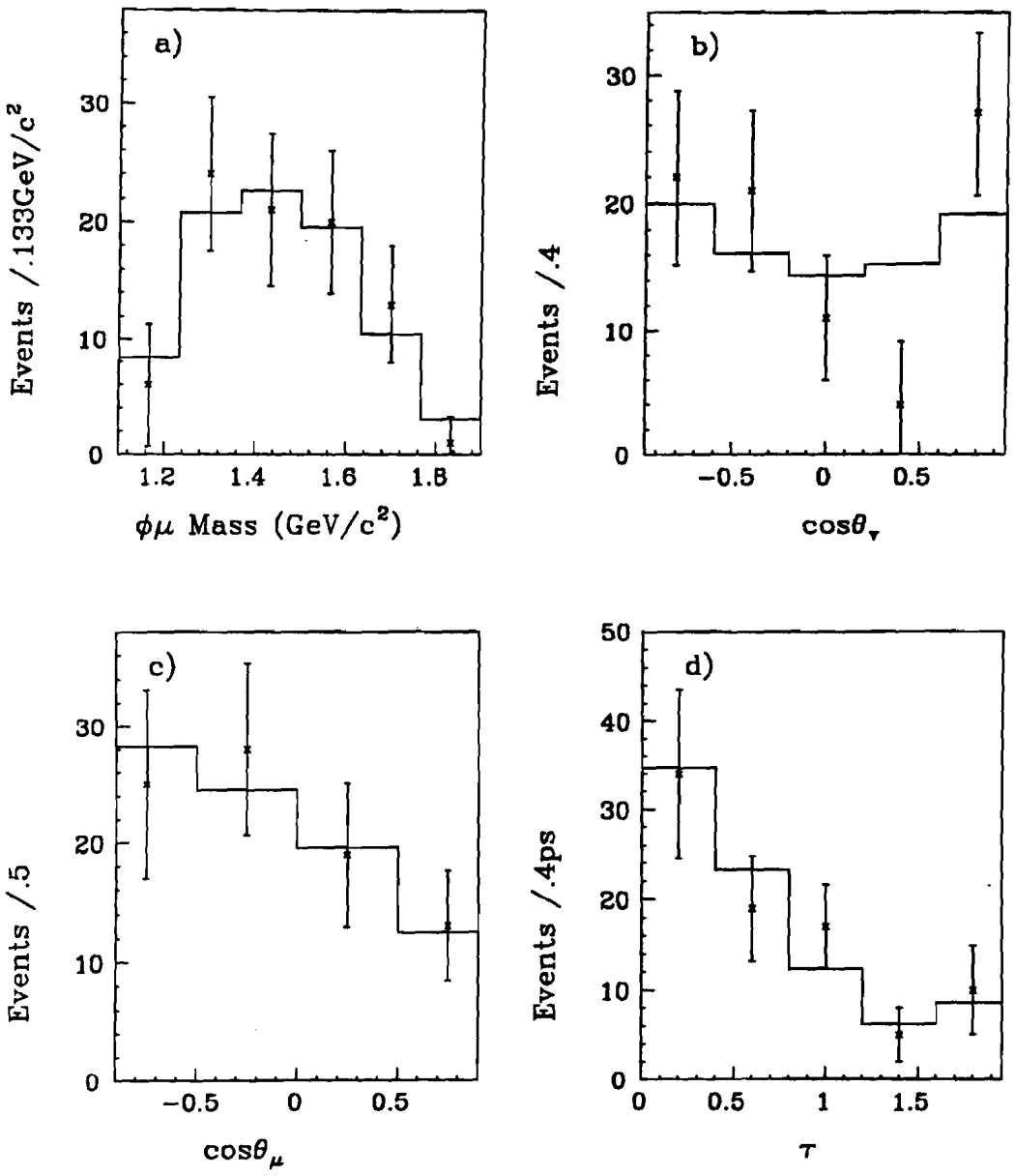

Figure 9.7. The projections of the fit results. The data are shown as the points with the errors bars. The fit result is displayed as a solid histogram. The three dimensions are a) $M(\phi\mu)$, b) $\cos\theta_\nu$, c) $\cos\theta_\mu$, and d) the proper time.

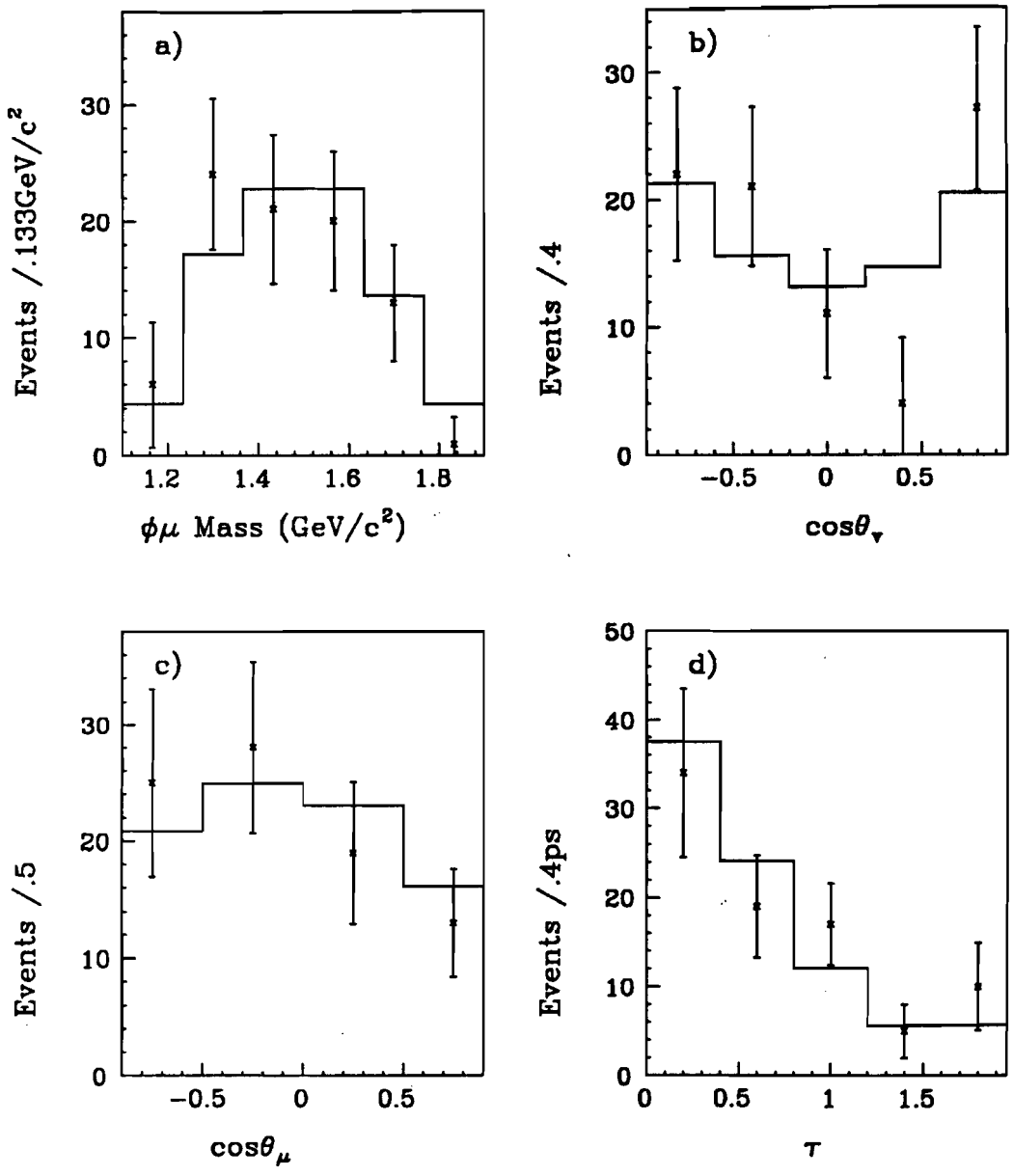

Figure 9.8. The projections predicted when we do not fit but simply subtract the expected backgrounds. The data are shown as the points with the errors bars. The prediction is displayed as a solid histogram. The three dimensions are a) $M(\phi\mu)$, b) $\cos\theta_v$, c) $\cos\theta_\mu$, and d) the proper time.

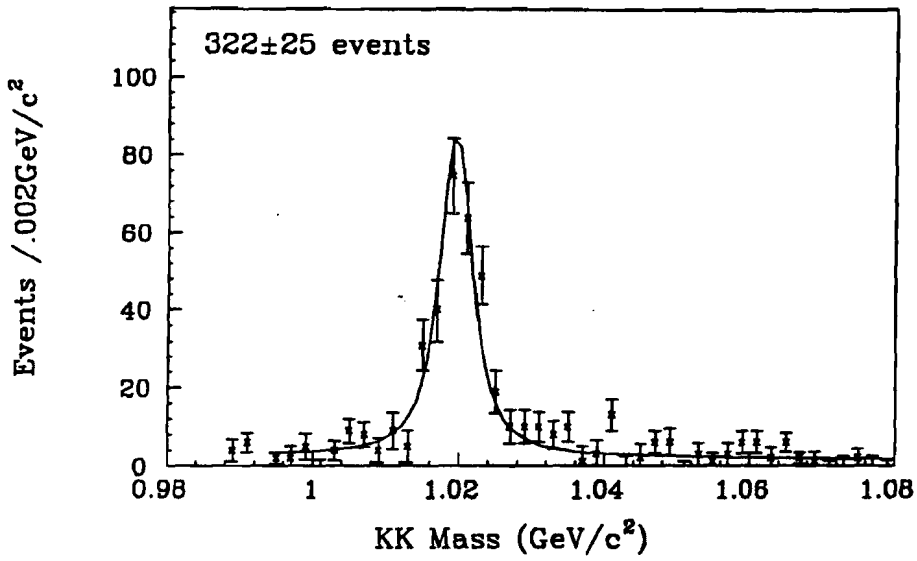

Figure 9.9. The ϕ mass for $D_s^+ \to \phi\pi^+$ candidates after subtracting the D_s^+ sidebands. The data are shown as the points with error bars and the fit is displayed as a solid line.

Chapter 10

Conclusion

We have presented an overview of the fixed target photoproduction experiment E687. We have presented a method of calculating the true errors on track parameters that were found by fits that ignore MCS and tests of these calculations. We have presented a candidate driven vertexing algorithm and demonstrated it effectiveness.

We have presented extensive tests demonstrating the experiments ability to reconstruct samples of four-body muonic semileptonic decays of D mesons, and have presented new measurements of the branching ratios:

$$\frac{\Gamma(D^+ \to K^-\pi^+\mu^+\nu(\text{nonresonant}))}{\Gamma(D^+ \to (K^-\pi^+)\mu^+\nu)} = .083 \pm .029$$

(or a limit of $< .12$ at the 90% confidence level),

$$\frac{\Gamma(D^+ \to (K^-\pi^+)\pi^0\mu^+\nu)}{\Gamma(D^+ \to (K^-\pi^+)\mu^+\nu)} < .042$$

and

$$\frac{\Gamma(D^+ \to \overline{K}^{*0}\mu^+\nu)}{\Gamma(D^+ \to K^-\pi^+\pi^+)} = .56 \pm .04 \pm .06$$

We have measured the form factors governing the decay $D^+ \to \overline{K}^{*0}\mu^+\nu$:

$R_v = 1.74 \pm .27 \pm .28$, $R_2 = .78 \pm .18 \pm .10$, which imply $\Gamma_l/\Gamma_t = 1.20 \pm .13 \pm .13$

We have presented the results of the isospin test:

$$\frac{\Gamma(D^0 \to K^{*-}\mu^+\nu)}{\Gamma(D^+ \to \overline{K}^{*0}\mu^+\nu)} = 1.37 \pm .34 \,{}^{+.15}_{-.35}$$

Finally, we have presented a measurement of the branching ratio:

$$\frac{\Gamma(D_s^+ \to \phi\mu^+\nu)}{\Gamma(D_s^+ \to \phi\pi^+)} = .58 \pm .11 \pm .08$$

which, with a theoretical input, implies

$$\frac{\Gamma(D_s^+ \to \phi\pi^+)}{\Gamma(D_s^+ \to \text{all})} = (3.1 \pm .6(\text{stat}) \pm .5\ (\text{sys}) \pm .4\ (\text{theoretical}))\%$$

References

[1] E687 Collab., P.L. Frabetti et al., Phys. Lett. B, to be published.

[2] L.M. Jones and H.W. Wyld, Phys. Rev. D 17 (1978) 759.

[3] E687 Collab., P.L. Frabetti et al., Nucl. Instr. and Methods A 320 (1992) 519.

[4] E691 Collab., J.R. Raab et al., Phys Rev D 37 (1988) 2391.

[5] E653 Collab., K. Kodama et al., Nucl. Instr. and Methods A 289 (1990) 146.

[6] CLEO Collab., D.G. Cassel et al., Nucl. Instr. and Methods A 252 (1986) 325.

[7] E691 Collab., J.C. Anjos et al., Phys. Rev. Lett. 65 (1990) 2630.

[8] E653 Collab., K. Kodama et al., Phys. Lett. B 274 (1992) 246.

[9] F.J. Gilman and R.L. Singleton, Phys. Rev. D 41 (1990) 142.

[10] J.G. Korner and G.A. Schuler, Z. Phys. C 46 (1990) 93.

[11] E687 Collab. P.L. Frabetti et al., Phys Lett. B, to be published.

[12] C.W. Bernard, A.X. El-Khadra, and A. Soni, Phys. Rev. D 45 (1992) 869. And V. Lubicz, G. Martinelli, M.S. McCarthy, and C.T. Sachrajda, Phys. Lett. B 274 (1992) 415.

[13] Particle Data Group, K. Hikasa et al., Phys. Rev. D 45 S1 (1993). See page VII.137 and references.

[14] E687 Collab., P.L. Frabetti et al., Nucl. Instr. and Methods A, to be published.

[15] E687 Collab., P.L. Frabetti et al., Phys. Lett. B 300 (1993) 190.

[15] E687 Collab., P.L. Frabetti et al., Phys. Rev. Lett. 70 (1993) 2058.

[16] E687 Collab., P.L. Frabetti et al., Phys. Rev. Lett. 70 (1993) 1381.

[17] E691 Collab., J.C. Anjos et al., Phys. Rev. D 45 (1992) R2177.

[18] E691 Collab. J.C. Anjos et al., Phys. Rev. Lett. 62 (1989) 722.

[19] Particle Data Group, K. Hikasa et al., Phys. Rev. D 45 S1 (1993).

[20] M. Bauer, B. Stech, and M. Wirbel, Z. Phys. C 29 (1985) 637. And M. Bauer and M. Wirbel, Z. Phys. C 42 (1989) 671.

[21] P. Ball, V.M. Braun, H.G. Dosch, and M. Neubert, Phys. Lett. B 259 (1991) 481. And P. Ball, V.M. Braun, and H.G. Dosch, Phys. Rev. D 44 (1991) 3567.

[22] V. Lubicz, G. Martinelli, M.S. McCarthy, and C.T. Sachrajda, Nucl. Phys. B 356 (1991) 301.

[23] C.W. Bernard, A.X. El-Khadra, and A. Soni, Phys. Rev. D 45 (1992) 869.

[24] G. Jaross, Ph.D. Thesis, University of Illinois at Urbana-Champaign, (1991).

[25] E687 Collab., P.L. Frabetti et al., Phys. Lett. B 263 (1991) 584.

[26] CLEO Collab., G. Crawford et al., Phys. Rev. D 44 (1991) 3394.

[27] E691 Collab., J.C. Anjos et al., Phys. Rev. Lett. 64 (1990) 2885.

[28] CLEO Collab., J. Alexander et al., Phys. Rev. Lett. 65 (1990) 1531.

[29] ARGUS Collab., H. Albrecht et al., Phys Lett. B 255 (1991) 634.

[30] E687 Collab., P.L. Frabetti et al., Phys. Rev. Lett., submitted.

Vita

Raymond Lloyd Culbertson [redacted]. He received his B.S. in physics from Towson State University in 1987 and was the class salutatorian. He completed an honors thesis on group decompositions in angular momentum. The same year he started graduate school at the University of Illinois at Urbana-Champaign with a summer fellowship. In the fall of 1987, he was a teaching assistant for general physics. For 1 1/2 years he worked on experiment E776, neutrino oscillations at Brookhaven. In January of 1990 he joined E687, photoproduction of heavy flavors at Fermilab and participated in the 1990-1991 fixed target run. He was the primary author on two papers, *A Measurement of the D^0 and D^+ Lifetimes*, E687 Collab., P.L. Frabetti et al., Phys. Lett. B 263 (1991) 584, and *Analysis of the Decay Mode $D^+ \to \overline{K}^{*0}\mu^+\nu$*, E687 Collab. P.L. Frabetti et al., Phys Lett. B, to be published. He also made a contribution to *Measurement of The Decays $D^0 \to \pi^+\pi^+\pi^-\pi^-$, $D^0 \to K^-K^+$, and $D_s^+ \to \phi\pi^+\pi^+\pi^-$*, E687 Collab. P.L. Frabetti et al., Phys Lett. B 281 (1992) 167, and *Description and Performance of the Fermilab E687 Spectrometer*, E687 Collab., P.L. Frabetti et al., Nucl. Instr. and Methods A 320 (1992) 519.